FIELD TRIALS FOR A RAPID DEPLOYMENT LIDAR-BASED HIGH TEMPORAL-FREQUENCY CHANGE DETECTION MONITORING SYSTEM

by

Arapi KANDIAH

THESIS PRESENTED TO ÉCOLE DE TECHNOLOGIE SUPÉRIEURE IN PARTIAL FULFILLMENT FOR A MASTER'S DEGREE WITH THESIS IN CONSTRUCTION ENGINEERING
M.A.Sc.

MONTREAL, APRIL 16, 2025

ÉCOLE DE TECHNOLOGIE SUPÉRIEURE
UNIVERSITÉ DU QUÉBEC

BOARD OF EXAMINERS

THIS THESIS HAS BEEN EVALUATED

BY THE FOLLOWING BOARD OF EXAMINERS

Mr. Jonathan D. Aubertin, Thesis Supervisor
Department of Construction Engineering, École de technologie supérieure

Dr. Diego Ramirez-Cardona, Professor
Department of Construction Engineering, École de technologie supérieure

Dr. Romain Rampa, Professor
Department of Systems Engineering, École de technologie supérieure

THIS THESIS WAS PRESENTED AND DEFENDED

IN THE PRESENCE OF A BOARD OF EXAMINERS AND THE PUBLIC

ON MARCH 28, 2025

AT ÉCOLE DE TECHNOLOGIE SUPÉRIEURE

ACKNOWLEDGMENTS

I would like to thank my project director, Dr. Jonathan D. Aubertin, for his invaluable guidance and support. In addition, I would like to thank Richard Prowt, Eole Valence, Niloufarsadat Sadeghi, and Bastien Charonnat for their assistance with my prototype, data analysis, and automation tools. Additionally, I would like to express my gratitude to the staff members of the ETS library for their assistance in helping me put the library's resources to use for study. Furthermore, I want to express my gratitude to Hatch and BBA, the companies I worked for and supported while conducting this research, for their assistance in managing my job and school.

Utilisation des technologies de télédétection pour la surveillance des glissements de terrain et des événements géologiques rapides

Arapi KANDIAH

RÉSUMÉ

Les technologies de télédétection sont aujourd'hui très répandues dans les applications de surveillance des risques géologiques. Les scanners laser (LiDAR), la photogrammétrie et les mesures topographiques par satellite peuvent être utilisés pour cartographier diverses géomorphologies, terrains naturels et infrastructures construites par l'homme. L'analyse de la détection des changements à l'aide d'ensembles de données topographiques capturées à une certaine fréquence permet de détecter les précurseurs de rupture et les glissements de terrain actifs, et d'analyser les événements a posteriori. La détection des changements dans le temps est souvent effectuée à haute résolution et à faible fréquence temporelle. Des ensembles de données denses réduisent considérablement l'incertitude inhérente à la rugosité superficielle et à la dispersion statistique entre deux séries de relevés. La surveillance à long terme et à haute résolution permet donc d'effectuer des mesures précises et de détecter des seuils de changement relativement bas. Une telle application n'est pas facilement applicable à la détection d'événements à évolution rapide. Lorsque des anomalies statistiques surviennent, comme des pluies intenses ou des tremblements de terre, des glissements de terrain peuvent être déclenchés et ne pas être détectés dans les délais requis pour agir et atténuer les effets. La présente étude examine les mesures de fréquence à faible résolution et à haute résolution temporelle en tant qu'option pour capturer les événements à évolution rapide.

Dans ce travail, un scanner laser fixe bon marché a été connecté à un petit Raspberry Pi pour collecter des images de nuages de points à intervalles d'une heure. Le montage consistait en une combinaison lidar-ordinateur montée sur un trépied ancré au sol. Tout le matériel électronique a été emballé dans une petite boîte pélican pour la protection de l'environnement. Cet article décrit le montage, le matériel nécessaire à l'assemblage et le protocole d'installation. Des considérations particulières ont été prises en compte pour un déploiement rapide avec une main-d'œuvre limitée. Deux expériences ont été réalisées pour tester le dispositif de surveillance. La première consistait à assembler un tas artificiel de matériaux humides moins que 4 mm dans une carrière locale. La pile a été partiellement excavée à la base pour obtenir une rupture progressive au fur et à mesure de l'assèchement du matériau. La surveillance de la pile a été effectuée pendant environ 3 semaines avec des relevés horaires. Un balayage à haute résolution a été effectué au début de l'essai à titre de référence. La deuxième expérience a consisté à analyser une plaine d'inondation à Grizzly Creek, au Yukon, pendant 10 mois au cours de la saison hivernale, avec 6 relevés par jour. La neige s'est formée au cours des mois et a fondu vers la fin de la période. Un balayage à haute résolution a été effectué au début des deux tests à titre de référence. Les résultats obtenus sont analysés et discutés dans l'article. Une discussion est fournie sur l'incertitude associée aux mesures topographiques collectées au cours de cette expérience.

Mots-clés : Télédétection, glissements, changements, mesures

Field Trials for a Rapid Deployment LiDAR-Based High Temporal-Frequency Change Detection Monitoring System

Arapi KANDIAH

ABSTRACT

Remote sensing technologies are now prevalent in geohazard monitoring applications. Laser scanners (LiDAR), photogrammetry, and satellite-based topographical measurements can be used to map various geomorphologies, natural terrains, and man-made infrastructures. Change detection analysis with topographical data sets captured at a certain frequency can denote failure precursors, and active landslide events, and analyze events a-posteriori. Change detection in time is often conducted at high resolution and low temporal frequency. Dense data sets considerably reduce the inherent uncertainty arising from superficial roughness and statistical spread between two series of surveys. Long-term, high-resolution monitoring thus allows for precise measurements and the detection of relatively low change detection thresholds. Such an application is not readily applicable to the detection of rapidly progressing events. When statistical outliers occur such as intense rains, or earthquakes, landslides may be triggered and not captured within the time frame required to act and mitigate. The present study investigates low-resolution, high-temporal frequency measurements as an option for capturing rapidly evolving events.

In this work, a low-cost fixed laser scanner was connected to a small Raspberry Pi to collect point cloud frames at hourly intervals. The montage consisted of the lidar-computer combination mounted on a tripod anchored to the ground. This paper describes the montage, material required to assemble, and installation protocol. Special considerations were given for rapid deployment with limited labor. To evaluate the monitoring setup, two experiments were done. One was that an artificial pile of humid less than 4 mm material was assembled in a local quarry. The pile was partially excavated at the toe to achieve a progressive failure as the material dried up. Monitoring of the pile was performed for approximately 3 weeks with hourly readings. A high-resolution scan was taken at the onset of the test for reference. The second experiment consisted of analyzing a floodplain in Grizzly Creek, Yukon for 10 months during the winter season, with six readings a day. Snow developed across the months and melted near the end of the period. A high-resolution scan was taken at the onset of both tests for reference. The results obtained are analyzed and discussed in the thesis. A discussion is provided on uncertainty associated with topographical measurements collected during this experiment.

Keywords: monitoring, detection, LiDAR, topographical, deployment

TABLE OF CONTENTS

Page

INTRODUCTION……………………………………………………………………...27

CHAPTER 1 SCOPE AND OBJECTIVES……………………………………………...29
1.1 Problem Statement 27
1.2 Goal and Objectives 30
1.3 Methodology 31
1.4 Chapter Overviews.....32

CHAPTER 2 LITERATURE REVIEW……………………………………………..…37
2.1 Remote sensing tools and methods 35
  2.1.1 Definitions..... 35
  2.1.2 Tools and applications 36
  2.1.3 Electromagnetic distance measurement (EDM) 36
  2.1.4 Photogrammetry..... 38
  2.1.5 Radars 39
  2.1.6 LiDAR..... 40
  2.1.7 Satellite based technologies 42
  2.1.8 Mobile and fixed remote sensing systems 42
  2.1.9 Digital Elevation Models (DEM)..... 43
2.2 Typical surveying framework 45
2.3 LiDAR-based remote sensing techniques 48
2.4 Quantifiable uncertainty and error margins with LiDAR surveys 55
2.5 Remote sensing assisted geohazard monitoring applications 58
2.6 High temporal-resolution monitoring solutions 72

CHAPTER 3 RAPID-DEPLOYMENT HIGH TEMPORAL RESOLUTION TLS MONITORING SYSTEM…………………………………………….....77
3.1 Desired specifications of the prototype and rationale 75
3.2 Components of the prototype 77
  3.2.1 Tripod..... 77
  3.2.2 Raspberry Pi..... 78
  3.2.3 Battery..... 80
  3.2.4 Hardware used for prototype 81
3.3 Montage and Assembly.....86
3.4 Blickfeld scanner interface and resolution specifications.....88

CHAPTER 4 COMPUTATIONAL METHODS…………………………….……………...95
4.1 Point Cloud Processing 93
4.2 Scan registration techniques 95
  4.2.1 The ICP algorithm..... 97
  4.2.2 Recursive ICP 99

4.3 Automation Method through Python code 100
4.4 Uncertainty and level of detection 101

CHAPTER 5 CONTROLLED PILE FAILURE HIGH TEMPORAL FREQUENCY MONITORING EXPERIMENT....................109
5.1 Scope and Objectives 107
5.2 Experimental Settings 108
5.3 Initial scan placement 113
5.4 Results and analysis 115
5.5 Error analysis and LOD computations 120
5.6 Discussions 122

CHAPTER 6 CHANGE DETECTION MONITORING IN YUKON WITH LOD ANALYSIS....................129
6.1 Scope of analysis 129
6.2 Experimental Settings 130
6.3 Initial scan placement 136
6.4 Change detection results 138
6.5 Level of detection analysis 148
6.6 Discussion and limitations 149

CHAPTER 7 DISCUSSION....................153
7.1 Comparison of Experiments 153
7.2 Additional Considerations 155
7.3 Limitations 157
7.4 Lowering uncertainty to improve LOD 161
    7.4.1 Sensor Calibration 162
    7.4.2 Filtration Methods 162
    7.4.3 Alternative Scanning Systems 162
    7.4.4 Environmental Factors 164
    7.4.5 Data collection and processing strategies 165

CONCLUSION....................167
Summary of work performed 167
Findings and research contributions 169
Recommendations and path forward 171

ANNEX A AUTOMATED PROCESSING SCRIPT 173

LIST OF REFERENCES....................176

LIST OF TABLES

Page

Table 5.1 Uncertainty components and LOD computations for controlled failure pile experiment 121

Table 6.1 Uncertainty components and LOD computations for Yukon monitoring case study 148

LIST OF FIGURES

Page

Figure 1.1 Vajont (Italy) Rockslide (a) overview of the mountainside (b) close-up view of the sliding surface with visible calcareous layers (c) sliding surface with failure profile 28

Figure 1.2 Inverse velocity representation concerning time for an accelerating rockslide event 29

Figure 2.1 Total station courtesy of Leica Geosystems 37

Figure 2.2 Digital Modular Camera DMC 2001 from Zeiss-Intergraph 38

Figure 2.3 Two-Dimensional SAR Geometry (a) data column of distributed scene for a fixed antenna (b) data of point targets for a moving antenna 40

Figure 2.4 Terrestrial static laser scanner courtesy of Riegl UK Ltd 41

Figure 2.5 DEM of the greater Montreal area with color scale for elevation 45

Figure 2.6 Conceptual representation of the phase difference method for distance measurements using a laser pulse 50

Figure 3.1 Tripod used for Prototype 78

Figure 3.2 Raspberry Pi Clock Model 4 80

Figure 3.3 12 V 18 A-hr Battery 81

Figure 3.4 30-inch Earth Anchor Set 82

Figure 3.5 Turnbuckle Jaw and Eye Galvanized 5/8 X 18 inches 83

Figure 3.6 Nail Common Bright Finish Smooth Shank Round 9 X 10 X 13 in Gauge Steel 83

Figure 3.7 Cable clamp Nylon 1/8 inch 84

Figure 3.8 Winch Cable 3/16 in 50 ft 840 lb 85

Figure 3.9 Welded Tube 1.25 in 6 ft 316 Stainless Steel 85

Figure 3.10 Prototype System 87

Figure 3.11 Blickfeld Cube 1 Outdoor LiDAR scanner..90

Figure 3.12 Blickfeld Cube 1 Outdoor Dimensions..91

Figure 4.1 Beam footprint error for the Blickfeld Cube 1..105

Figure 4.2 Beam footprint error for the Blickfeld Cube 1 for incidence angle of 40 and 60 degrees 106

Figure 5.1 Limestone Pile at Sintra Quarry of Fine and Wet Granular Material 109

Figure 5.2 Excavation Pile (on the left) and FEL (on the right) 109

Figure 5.3 Plan View of Sintra Quarry...110

Figure 5.4 Topographical Plan View with Color Elevation of Sintra Quarry...........111

Figure 5.5 High-Resolution Scan of Limestone Rock Pile 112

Figure 5.6 Cropped zone from the high resolution topographical data set of reference...114

Figure 5.7 Registration error graph for RICP number of iterations 115

Figure 5.8 Change detection analysis reported in terms of average and standard deviation...116

Figure 5.9 Maximum C2C measurement from the cloud distribution 117

Figure 5.10 Average C2C measurements captured during day and night intervals 118

Figure 5.11 Change detection analysis reported in terms of average and 95 % C2C confidence interval computed as $\mu + 2\sigma$..119

Figure 5.12 HTF scan on November 7th at 14:00 with color scale for C2C measurement and overlaid on top of the high resolution reference scan 120

Figure 6.1 Grizzly creek location where the experimental field work was carried as part of this chapter 130

Figure 6.2 Topographical model of the zone monitored at Grizzly creek 132

Figure 6.3 Picture of the monitored zone for high temporal frequency change detection monitoring 133

Figure 6.4 Topographical data set with color scale for vertical elevation 133

Figure 6.5 High resolution topographical data set with color-scale for point density 134

Figure 6.6 High temporal frequency monitoring system used at Grizzly Creek.......135

Figure 6.7 Registration error graph for RICP number of iterations 137

Figure 6.8 Change detection analysis results with respect to high and low resolution reference scans with monthly averaging 139

Figure 6.9 Change detection analysis results with respect to high and low resolution reference scans with weekly averaging for 2022 data 140

Figure 6.10 Change detection analysis results with respect to high and low resolution reference scans with weekly averaging for 2023 data 140

Figure 6.11 Maximum C2C values measured from the change detection analysis developed on a monthly average 141

Figure 6.12 High temporal frequency scans respective placement for low-resolution reference scan dated September 23 2022 (red) and scan taken on March 30 2023 (blue) 142

Figure 6.13 High temporal frequency scans respective placement for low-resolution reference scan dated September 23 2022 (red) and scan taken on March 30 2023 (blue) 142

Figure 6.14 C2C distances between scan taken on March 30th 2023 and low-resolution reference scan 144

Figure 6.15 C2C distances between scan taken on March 30th 2023 and low-resolution reference scan (The scan in red is for the low-resolution reference scan) 144

Figure 6.16 Change detection analysis results with respect to high and low resolution reference scans with daily averaging for 2023 data 145

Figure 6.17 March 30th 2023 scan with color scale for C2C with respect to the high resolution reference scan (a) pseudo-isometric view and (b) from an arbitrary angle to emphasize the gap between the two scans 147

LIST OF ABBREVIATIONS

°C	Degrees Celsius
3D	Three-dimensional
A-hr	Ampere-hour
AI	Artificial Intelligence
AMR	Advanced Microwave Radiometer
AMR-C	Advanced Microwave Radiometer - Climate Quality
BIM	Building information modeling
C2C	Cloud-to-cloud
CI	Confidence Interval
cm	centimeters
CNES	Centre National d'Études Spatiales
CPU	Central Processing Unit
CSV	Comma-separated values
CW	Continuous-wave
DC	Direct current
DEM	Digital Elevation Models
DERM	Digital Elevation Reference Model
DMC	Digital modular camera
DORIS	Doppler Orbitography and Radio positioning Integrated via Satellite
DSHA	Deterministic Seismic Hazard Analysis
DSM	Digital Surface Model
EC	European Commission

EDM	Electromagnetic distance measurement
ESA	European Space Agency
ESRI	Environmetal Systems Research Institute
EUMETSAT	European Organization for the Exploitation of Meteorological Satellites
EWS	Extra-Wide Swath
FEL	Front-End Loader
FoV	Field of View
GCP	Ground Control Point
GeoTIFF	Geographic Tag Image File Format
GHz	Gigahertz
GIS	Geographic information systems
GNSS	Global Navigation Satellite Systems
GPIO	General Purpose Input/Output
GPS	Global Location System
HH	Horizontal-vertical
HTF	High temporal frequency
HV	Horizontal-vertical
i.e.	For example
I2C	Inter-Integrated Circuit
ICP	Iterative Closest Point
IEC	International Electrotechnical Commission
InSAR	Interferometric Synthetic Aperture Radar
IP	Internet Protocol

kd	K-dimensional
km	Kilometers
LAS	LiDAR Aerial Survey
LAZ	LiDAR Aerial Survey zip format
LiDAR	Light Detection and Ranging
LoD	Level of Detection
LOD	Level of Detection
m	meters
MEMS	Micro Electronic Mechanical Systems
mm	millimeters
MSL	Mean sea level
NASA	National Aeronautics and Space Administration
NIR	Near-Infrared
nm	nanometers
NOAA	National Oceanic and Atmospheric Administration
PLY	Polygon File Format
PPE	Personal protective equipment
PSHA	Probabilistic Seismic Hazard Analysis
PTS	Point Cloud Text
RAM	Random-Access Memory
Reg	Registration error
R-ICP	Recursive ICP
ROR	Radius Outlier Removal

RTC	Real-Time Clock
SAR	Synthetic aperture radar
SLAM	Simultaneous Localisation and Mapping
SM	Stripmap
SOR	Statistical Outlier Removal
TCP	Transmission Control Protocol
TIN	Triangulated Irregular Network
TLS	Terrestrial laser scanner
ToF	Time of Flight
UAV	Unmanned aerial vehicles
UNC	Unified National Coarse
V	Volts
VH	Vertical-horizontal
VV	Vertical-vertical

LIST OF SYMBOLS

a_{el}	Largest axis of the ellipse
E_{CI}	Error associated with given measurement along a reference frame for specific CI
I_B	Measurement distance
$RMSD_{C2C}$	Root Mean Square Deviation for C2C distribution
β	Beta
θ_I	Incidence angle
μ_{C2C}	Average distance for C2C distribution between two registered scans
σ_{BF}	Beam footprint error
σ_{tool}	Tool calibration
σ_{xy}	Standard deviation for the xy plane
σ_z	Standard deviation for the z plane

INTRODUCTION

Effective geohazard monitoring is critical in the field of engineering, especially in the context of geotechnical research, as evidenced by the rapidly growing construction projects and increased mining operations. Because these projects are complex, careful supervision is required to reduce hazards and protect both people and infrastructure. This research explores the complexities of geohazard surveillance, addressing a basic issue that is present in modern methods.

The limits of traditional geohazard surveillance techniques are the central problem statement of this study. Seasonal or monthly survey frequencies, common in geohazard programs, fall short of capturing the quick, fleeting events caused by things like heavy rain or seismic activity. This shortcoming exposes projects to unanticipated risks, highlighting the urgent requirement for a monitoring system that can provide high-frequency data collecting without requiring prohibitive financial or temporal commitments.

The primary issue this project aims to answer is: how can geohazard monitoring be improved to better account for the dynamic character of triggered events? By putting forth a novel strategy focused on the creation of a low-cost, high-temporal-resolution laser scanning prototype, this work seeks to answer this question. This prototype intends to transform geohazard monitoring procedures by utilizing innovative technology and processes. It will provide stakeholders with real-time insights into changing hazard conditions and enable them to take initiative-taking decision-making.

The research conducted aims to close the gap between traditional monitoring methods and the changing needs of contemporary engineering projects. In addition to shedding light on the urgent problems facing geotechnical practitioners, this study aims to spark revolutionary developments in geohazard monitoring techniques by describing the conception, execution, and field testing of the suggested prototype. The ultimate objective of this research is to provide the engineering community with an affordable and scalable system that emphasizes the collection of high-temporal-resolution data, therefore supporting the sustainability and resilience of mining and construction projects worldwide.

CHAPTER 1

SCOPE AND OBJECTIVES

1.1 Problem Statement

The expansion of construction activities and increasing mining operations have led the way to a remarkable growth in geotechnical work worldwide. Both construction and mining operations heavily rely on geotechnical engineering, which includes soil and rock mechanics to evaluate subsurface conditions and their impact on infrastructure. As excavation and surface remodeling operations significantly alter the natural environment, they can lead to a wide variety of geohazards. Such geophysical processes, such as rockslides, landslides, rockfalls, and excessive subsidence, can have drastic economic impacts and lead to major safety concerns. Geotechnical engineers are therefore tasked with providing robust and resilient designs for safe and reliable operations over exceptionally extended periods. The design process is inherently intertwined with monitoring activities which are necessary to corroborate preliminary assumptions and validate the analytical framework integrated in the construction. The present research addresses modern techniques for geotechnical monitoring, with an emphasis on remote sensing-based non-destructive methods.

The environment as a whole may suffer from these types of landslides in several ways, like forest and habitat destruction, deterioration of soil, and deposition of streams. Elimination of the vegetation cover worsens soil erosion and reduces biodiversity. Landslide-related sediment flow has the potential to harm aquatic habitats and lower water quality. Roads, trains, and airports are among the transportation networks that might be affected by landslides, which can result in delays, detours, and closures. Infrastructure damage can make it more difficult to provide emergency services, access to healthcare, and necessary supplies and services to affected populations.

To exemplify the impact and scale of geohazards induced in part by man-made large construction, the famous historical rockslide of 1963 Vajont, Italy, is often cited as a milestone case study that impacted fundamentally geotechnical engineering (Hoek, 2007). Many communities were destroyed, and thousands of people lost their lives as a result of the catastrophic landslide-generated tsunami that was caused by the collapse of a large piece of Mount Toc into the Vajont reservoir. The Vajont region has mountain slopes made of limestone and marl formations, among other sedimentary rocks. As a result of their geological structure and the existence of bedding planes and cracks, as shown in Figure 1.1 below, these rocks are vulnerable to instability. Therefore, these weak geological formations that were prone to failure and significant rain were the main causes of the Vajont landslip, which displaced rock and debris of around 270 million cubic meters. The rock pile became wet from the intense rain, which decreased its stability and raised the possibility of the slope collapse. This severely damaged and destroyed houses, companies, roads, bridges, and other buildings. There was serious environmental harm caused by the millions of cubic meters of rock and debris that were moved into the Vajont reservoir. The environment and terrain of the impacted area also changed due to the flooding, having a long-lasting impact on the water quality, vegetation, and wildlife.

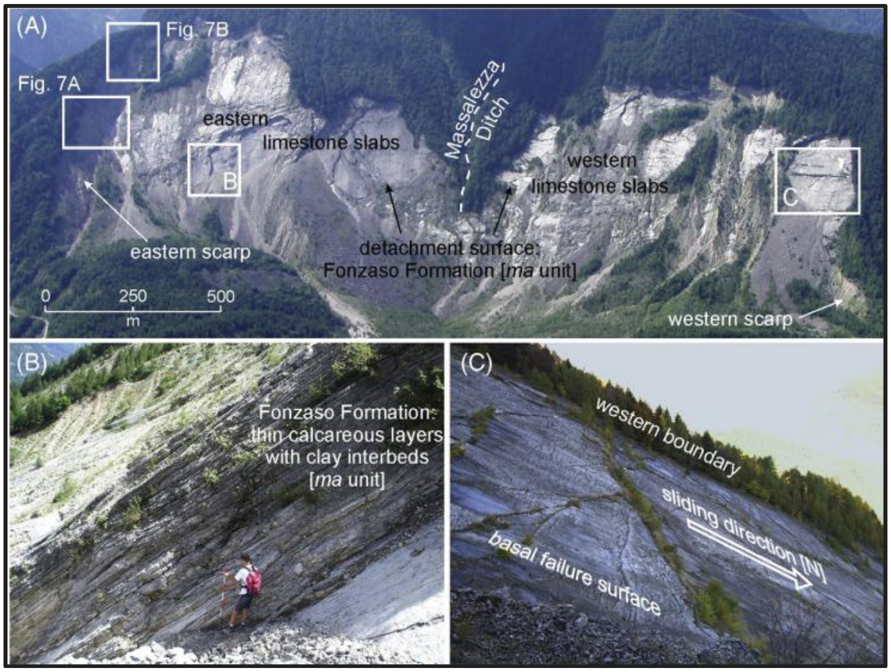

Figure 1.1 Vajont (Italy) Rockslide (a) overview of the mountainside (b) close-up view of the sliding surface with visible calcareous layers (c) sliding surface with failure profile
Taken from Paronuzzi and Bolla (2012, p. 45)

The Vajont incident underscores the scale and potential impact of geohazards near the urban environment. It also triggered an intense reactionary movement in geotechnical engineering circles to address rock engineering as a distinct topic of interest and emphasized the need to monitor somehow the evolutive nature of potential geohazards. Later work on evolving geohazards highlighted the progressive acceleration typically observed with large-scale landslides and rockslides. Rose and Hungr (2007) presented a detailed quantifiable perspective on the deformation rate of large rockslides. Figure 1.2 (a) illustrate conceptually the concept of inverse velocity used by Rose and Hungr to represent an evolving landslide movement. They inferred that such a representation may potentially yield information on the critical time of failure. Figure 1.2 (b) exemplifies this concept with a series of normalized case studies. These plots further emphasize the value and importance of systematic monitoring around geohazards for various risk management considerations.

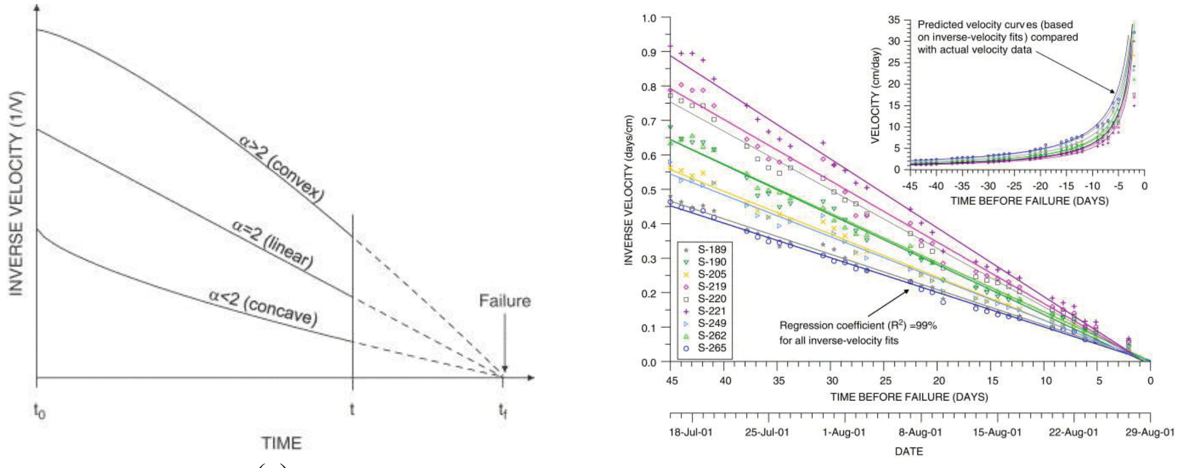

(a)

(b)

Figure 1.2 Inverse velocity representation concerning time for an accelerating rockslide event Taken from Rose and Hungr (2007, p. 308)

Geotechnical monitoring can be categorized broadly as intrusive and non-intrusive. The more traditional intrusive methods typically rely on excavated trenches or drilled exploration holes where water pressure and settlement can be measured. Extensive information on conventional investigation and monitoring methods can be found in Holts et al. (1981).

In the last two decades, remote sensing technologies have become prevalent in large-scale monitoring schemes. These non-intrusive methods rely on image analysis (i.e. photogrammetry) or the emission and reflection of electromagnetic pulses (i.e. laser scanners) to generate detailed physical models that can be further processed and analyzed. Unmanned aerial vehicles (UAV) such as battery-powered drones have further enhanced the accessibility and applicability of these tools with cost-effective solutions.

Modern monitoring schemes for geohazards near urban environments or mining operations integrate recurring remote sensing data collection to track evolving conditions and capture changes if any. Such schemes may involve seasonal to monthly data collection, and even weekly captures in some instances. Such programs yield massive data sets which can be time-consuming to analyze and limit the applicability for dependable and systematic geohazard monitoring. Furthermore, it is apparent when considering the physical nature of geohazards that triggering events may occur which would preclude the possible capture of the resulting hazard with monthly and even weekly surveys. There therefore is an ability from conventional remote sensing tools to detect and inform upon rapid changes related to geohazards. The present research addresses high-temporal frequency remote sensing-based monitoring as a potential complement to traditional non-intrusive periodic surveys to capture rapid changes (Carlà et al, 2024).

1.2 Goal and Objectives

The present research investigates the applicability of high-temporal resolution remote sensing data collection for geohazard monitoring applications. The research is geared towards developing a pragmatic, cost-effective solution that could readily be deployed and integrated in construction and mining settings for geohazard monitoring applications. The research further addresses uncertainty associated with remote sensing data collection and concerning the achieved resolution. It is emphasized that high-temporal frequency data collection must in some ways limit the resolution of collected data to avoid the overwhelming large data sets that would be collected.

The goal of this research is to **develop a framework for a high-temporal resolution LiDAR-based monitoring system with quantified uncertainty**. To achieve the stated goal, the following objectives were identified:

1. Develop a low-cost testing prototype and associated application methodology.
2. Test the prototype in different physical and environmental conditions.
3. Quantify uncertainty associated method concerning resolution and surface measured.
4. Define automation method for systematic computation and analysis.

1.3 Methodology

The present work was divided into three distinct research activities: (i) development and implementation of a remote sensing prototype, (ii) field trials and results analysis, and (iii) automation and uncertainty analysis. These activities are briefly described below and further addressed throughout the thesis.

The remote sensing prototype is a small, adaptable monitoring system intended for gathering high-resolution data in regions vulnerable to geohazards. It offers quick deployment and accurate spatial data collecting by using parts including cable clamps, stainless steel welded tubing, and a LiDAR scanner. The prototype's sturdy design and adaptable mounting options allow for precise environmental change monitoring, which improves risk assessment and mitigation activities.

To assess the monitoring system's efficacy and performance, real-world geohazard scenarios are used for deployment during the field trials. The trials evaluate the system's capacity to identify and track dynamic changes with high temporal resolution using controlled experiments and data gathering in settings vulnerable to dangers like landslides or rockfalls. The system's dependability and its potential to improve geohazard monitoring and management techniques are validated by analysis of the data gathered.

Creating a Python script as part of the automation process can expedite data processing and analysis and guarantee the effective extraction of pertinent information from point cloud data that the LiDAR scanner has acquired. Simultaneously, uncertainty analysis measures the precision and consistency of monitoring outcomes by analyzing standard deviations, error margins, and the maximum, minimum, and average change detection values. The research guarantees accurate and dependable geohazard monitoring results by automated computational techniques and thorough uncertainty assessment, which are essential for well-informed decision-making and risk management plans.

1.4 Chapter Overviews

The following information will give an overview of each chapter. **Chapter 2** reviews the relevant literature on remote sensing and LIDAR technology, along with a background on their fundamental theories, technology, and uses. The use of LIDAR and remote sensing in environmental monitoring and Earth observations, among other domains, shall be emphasized. The data collection, processing, and analysis procedures used by remote sensing and LIDAR systems to produce information about the different surfaces on Earth will be described.

Chapter 3 refers to the rapid deployment high temporal resolution LIDAR monitoring system, which is a light detection and ranging system that may be easily constructed and used to regularly sample the temporal domain while gathering high-resolution topography data. A LiDAR sensor that can record high-resolution points clouds of different rocks and soils would be part of the system. Depending on the needs of the deployment, the sensor can be installed on a vehicle, drone, tripod, or aircraft that is stationed on the ground. Users would be able to quickly gather topographic data over wide areas or target areas of interest with the system's simple setup and field deployment design.

Chapter 4's content is about computation methods including the point cloud registration and processing, automation methods through Python, and the level of direction in LiDAR systems. Data preprocessing can be done through CloudCompare by cleaning and filtering the raw point cloud data to get rid of noise and outliers. Point cloud registration is the process of aligning several scans or datasets obtained from various angles or points in time to produce a single coordinate system. Python scripting is used to automate point cloud processing tags of large datasets, facilitating the efficient execution of recurring processes like data preparation, registration, and analysis across numerous scans or datasets. The level of detection is to recognize and measure temporal variations across several point cloud datasets that were collected at various times.

Chapter 5 describes a controlled pile failure monitoring experiment done at a limestone quarry in Saint-Alphonse-de-Granby, Quebec. A big pile of rocks of 10-14 mm was excavated using a front-end loader, to induce a failure. The low-cost, high temporal resolution LiDAR monitoring system was placed to monitor the behavior of the limestone excavated pile, analyze the structural characteristics, and change detection across a period of 7 days.

Chapter 6 includes a similar analysis as Chapter 5 except for a floodplain in Grizzly Creek, Yukon for a complete winter, in a period of 10 months from August 2022 to June 2023. The uncertainties were quantified with the comparison of the initial high-resolution photogrammetry scan and the low-resolution scans obtained from the LiDAR system.

Chapter 7 is the comparison and contrasts of the limestone quarry-induced failure experiment and the ice floodplain. The 2 LiDAR experiments' configurations, sensors used, data collection procedures, and scanning parameters (such as resolution, range, and frequency) will be examined. There are variations in the experimental techniques utilized, including the test site selection, instrumentation, and data processing methods. To ensure consistency and comparability between the two datasets, the effectiveness of the raw data filtering and registration will be evaluated. The point cloud density, accuracy, precision, and coverage of each experiment's LiDAR data collection will be analyzed to determine its quality and reliability.

Chapter 8 concludes the experimental analysis and literature studies. It will summarize the key conclusions and observations drawn from the two LiDAR studies' comparison, emphasizing the similarities, differences, and noteworthy trends found. An overview of the main quantitative and qualitative findings from the LiDAR data analysis will be provided.

CHAPTER 2

LITERATURE REVIEW

2.1 Remote sensing tools and methods

2.1.1 Definitions

An essential tool for engineering surveys is remote sensing, which allows for the acquisition of important information on the surface and subsurface properties of the Earth without the need for direct physical contact. The process of gathering data about a target, region, or event by analyzing data from sensors installed on platforms such as satellites, airplanes, or drones that are far away from the target is also known as remote sensing. These sensors record electromagnetic radiation that the Earth's surface emits or reflects. This data is processed to produce useful geographic information. Remote sensing is concisely defined by Campbell and Wynne (2011) as:

> […] the practice of deriving information about the Earth’s land and water surfaces using images acquired from an overhead perspective, using electromagnetic radiation in one or more regions of the electromagnetic spectrum, reflected or emitted from the Earth’s surface.

The wide range of energy that materials and things emit as waves or particles is known as electromagnetic radiation. Remote sensing devices pick up electromagnetic radiation in various wavelengths, from visible light to radio, microwave, and infrared. Important details regarding the characteristics, makeup, and environmental circumstances of the Earth's surface are revealed by the interaction of electromagnetic radiation with the surface.

Satellites, airplanes, and drones are examples of mobile remote sensing platforms that are used to carry sensors or instruments for data collection. These platforms have sensors that can identify and capture electromagnetic radiation that the Earth's surface emits or reflects. Aircraft and drones offer greater spatial resolution and flexibility for focused data collecting, while satellites offer worldwide coverage and long-term monitoring capabilities.

Specialized devices called remote sensing sensors are positioned atop platforms to detect electromagnetic radiation that the Earth's surface emits or reflects. Surface characteristics, terrain, vegetation, and environmental conditions can all be characterized thanks to these sensors' ability to detect radiation within particular wavelength bands. Thermal infrared, radar, lidar, and optical sensors (such as cameras and multispectral imagers) are examples of common remote sensing sensors.

The process of identifying and characterizing surface features, terrain shape, land use, and climatic variables using remote sensing imagery is known as image interpretation. Extracting useful information from unprocessed image data requires computer-based analysis tools, digital image processing, and visual interpretation.

2.1.2 Tools and applications

A wide range of devices and tools are used in remote sensing to record and examine electromagnetic radiation that the Earth's surface emits or reflects. These instruments are used in many different fields for a variety of purposes. The following outlines several popular categories of remote sensing instruments and the uses for which they are appropriate. The tools emphasized in this section, and in this thesis, are for generating digital elevation models (DEM), i.e., topographical data sets. Geophysical processes, density variation, magnetic resonance, and other applications are mentioned briefly when relevant, but are not central to the present research.

2.1.3 Electromagnetic distance measurement (EDM)

Optical sensors that detect electromagnetic radiation in the visible and near-infrared range include cameras and multispectral imagers. Numerous fields, including agriculture, urban planning, vegetation monitoring, and land cover classification, make extensive use of these sensors. Resource management and environmental assessment are aided by the ability to distinguish surface features based on their spectral fingerprints, which is made possible by multispectral photography. Algorithms for dividing the slope distance into horizontal and vertical components are present in contemporary total stations, as shown in Figure 2.1. Total stations with automated data logging are becoming commonplace on-site equipment for engineering surveys. (Schofield & Breach, 2007)

Figure 2.1 Total station courtesy of
Leica Geosystems
Taken from Schofield & Breach
(2007, p. 128)

2.1.4 Photogrammetry

Digital photogrammetry is a remote sensing method that measures and analyses surface properties on Earth by using digital photographs. It is built on the concepts of stereoscopy, which reconstructs the three-dimensional form and location of things by using overlapping photos captured from various perspectives. This method is frequently used in engineering, urban planning, and environmental monitoring for mapping, topographic modelling, and producing detailed surface models. Software tools are used in digital photogrammetry to automatically find corresponding points in overlapping photos, determine their positions, and produce a three-dimensional point cloud. The precision of the photogrammetric techniques employed, the degree of overlap, and the image quality all affect how accurate this process is. Digital photogrammetry uses advances in image processing, computing power, and digital storage to deliver more precise and efficient data gathering and analysis than traditional photogrammetry, which depends on analogue images and manual measurements. An example of digital photogrammetry equipment is the DMC 2001 from Zeiss-Integraph, which is now part of Leica Geosystems under Hexagon, shown in Figure 2.2 below (Egels and Kasser, 2001).

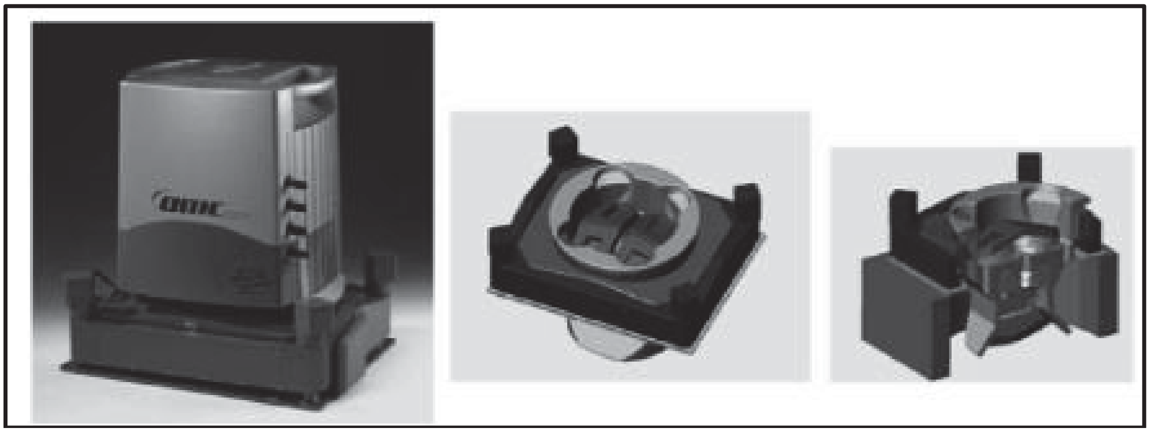

Figure 2.2 Digital Modular Camera DMC 2001 from Zeiss-Intergraph
Taken from Egels and Kasser (2001, p. 52)

The mid-infrared spectrum, which reflects the thermal energy released by surfaces and objects, is where thermal infrared sensors pick up radiation emissions. Applications including heat mapping, energy efficiency analysis, and environmental monitoring make use of these sensors. Temperature fluctuations can be detected using thermal infrared photography, which makes it easier to identify thermal anomalies and heat signatures in natural settings, industrial locations, and urban regions.

A thorough spectrum examination of surface materials and features is made possible by hyperspectral sensors, which collect electromagnetic radiation over hundreds of small spectral bands. Applications for these sensors include pollution detection, precision farming, environmental monitoring, and mineral prospecting. Hyperspectral photography allows the identification of certain minerals, vegetation species, and contaminants by providing fine-scale information about material composition (Schofield & Breach, 2007).

2.1.5 Radars

To create images of the Earth's surface, radar sensors emit microwave radiation and monitor the timing and strength of the reflected signals. Radar sensors known as Synthetic Aperture Radar (SAR) devices are widely employed in oceanography, disaster monitoring, and terrain mapping. The geometry of two-dimensional SAR is shown in Figure 2.3 below. Even in bad weather or at night, SAR photography offers important insights into surface topography, plant structure, and geological features (Berens, 2006).

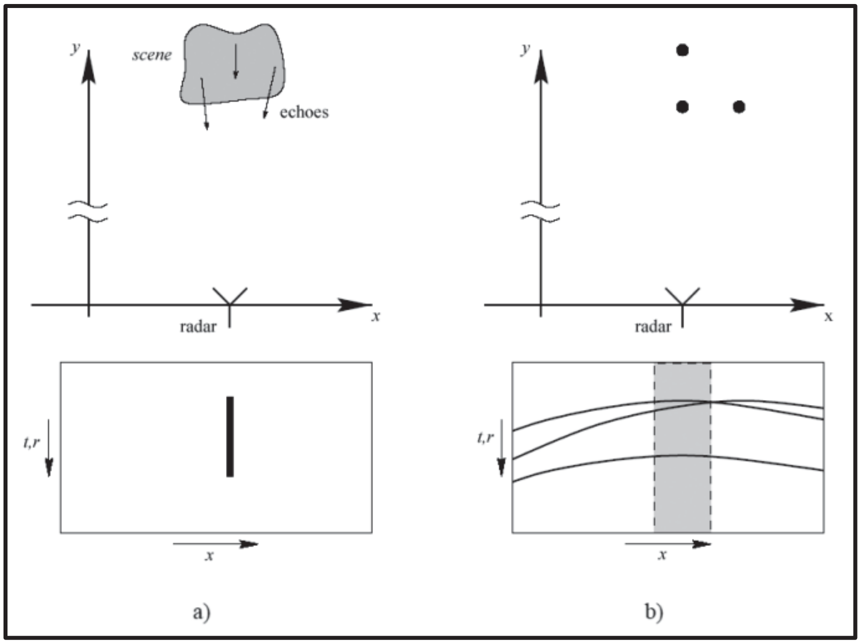

Figure 2.3 Two-Dimensional SAR Geometry (a) data column of distributed scene for a fixed antenna (b) data of point targets for a moving antenna
Taken from Berens (2006, p. 3-5)

2.1.6 LiDAR

Laser pulses are emitted by lidar (light detection and ranging) sensors, which track how long it takes for the pulses to return after coming into contact with surfaces or objects. Urban planning, forest inventory, topography mapping, and infrastructure monitoring are just a few of the uses for these sensors. Accurate terrain analysis, high-resolution elevation models, and three-dimensional (3D) visualization of natural and constructed environments are made possible by LiDAR data.

One kind of LiDAR (Light Detection and Ranging) technology used to collect comprehensive three-dimensional (3D) data about the Earth's surface and its objects is the Terrestrial Laser Scanner (TLS). TLS systems are made to scan the surroundings from a fixed point and are usually mounted on a tripod or fixed mount. They can create exact 3D point clouds by emitting laser pulses and measuring the time it takes for the pulses to return after reflecting off surfaces. An example is shown below (Schofield & Breach, 2007).

Figure 2.4 Terrestrial static laser scanner courtesy of Riegl UK Ltd
Taken from Schofield & Breach (2007, p. 583)

Key features include high precision where TLS systems provide accuracy from millimeters to centimeters, which makes them perfect for in-depth surveys. Point clouds are dense collections of 3D coordinates that reflect the scanned environment. Point clouds are created by processing the data that TLS systems have collected. Range is another feature of TLS systems, which, depending on their specifications, can collect data over a few meters to several hundred meters. Among the applications are those in architecture and construction for structural analysis and building information modeling (BIM), archaeology for 3D documentation of historical places and artifacts, forestry for measuring tree heights and density in forests, and mining for keeping an eye on mine walls and structures. Benefits include their effectiveness for both small- and large-scale surveys, their incredibly accurate and detailed data collecting, and their ability to capture intricate details and complex geometries. The fact that this scanner needs to be in the line of sight of the target, which can be blocked by trees, structures, or other objects, as well as the fact that it is rather expensive and needs skilled workers to operate and handle the data are its drawbacks (Schofield & Breach, 2007).

2.1.7 Satellite based technologies

To georeference remote sensing data and ground truthing, Global Navigation Satellite Systems (GNSS) receivers, such as GPS (Global Location System) and GNSS augmentation systems, offer precise location and timing data. In remote sensing applications, these systems are crucial for georeferencing, geolocation, and the integration of geographic data.

Overall, a wide range of applications in environmental assessment, resource management, disaster monitoring, and infrastructure development are made possible by the diverse array of remote sensing tools and instruments, which provide useful capabilities for monitoring and analyzing the Earth's surface and subsurface features (Schofield & Breach, 2007).

2.1.8 Mobile and fixed remote sensing systems

Fixed remote sensing systems use fixed sensors that watch over a certain area continuously or sporadically. Usually, these systems are set up permanently in a structure, tower, or special monitoring station. One of the fixed systems' main advantages is that it can collect data continuously over an extended period of time from a constant point of view. This is important for tracking changes in a particular region over time. The applications include structural health monitoring, which keeps an eye on the state of buildings, bridges, and other infrastructure, security surveillance, which continuously monitors high-security areas, and environmental monitoring, which tracks changes in vegetation, soil moisture, or atmospheric conditions. Fixed remote sensing has the advantages of continuous data collecting over extended periods of time, as well as high precision and consistency because of its fixed placement. There are drawbacks as well, such as the sensors' spatial restrictions and the inability of these systems to collect data from numerous or moving targets without the deployment of extra sensors (Schofield & Breach, 2007).

Sensors installed on moving platforms, such as automobiles, drones, airplanes, or satellites, are used in mobile remote sensing solutions. These systems are frequently used for surveying, mapping, and monitoring in dynamic situations because they allow collecting data over large or challenging-to-access areas. Applications include disaster response (evaluating conditions and damage following catastrophes like earthquakes or floods), agricultural monitoring (evaluating crop health over wide fields), and land surveying and mapping (capturing topographic data over big areas). Benefits include the capacity to reach far-off places and cover big regions and versatility in data collecting across a range of environments. Cons are that they are usually more expensive and complex to deploy and run, and they may have lesser precision than stationary systems due to movement and environmental conditions (Schofield & Breach, 2007).

2.1.9 Digital Elevation Models (DEM)

A digital depiction of the topography of the Earth is called a digital elevation model (DEM). It is a three-dimensional depiction of the elevation of the ground and is commonly used for surface feature analysis and visualization. DEMs are essential for many applications, including engineering, land use planning, environmental modeling, and geographic information systems (GIS).

The terrain elevation data is represented by a DEM as a grid of uniformly spaced points, or pixels, with elevation values assigned to each pixel. The height above a given reference point, often mean sea level (MSL), is shown by these elevations. Depending on the needs of the program and application, DEMs can be exchanged and saved in a variety of digital forms. Raster Format is among the frequently used formats. This is made up of one of the most used formats, GeoTIFF. Elevation data is contained in the georeferenced raster format known as GeoTIFF. Every pixel in the raster grid corresponds to a distinct region on the earth and has a corresponding elevation value. A common format in GIS applications for spatial analysis is ESRI Grid, which is unique to ESRI's ArcGIS program. Elevation data is stored in the straightforward text-based ASCII Grid format as a grid of numbers with extra metadata for georeferencing. The Triangulated Irregular Network (TIN) is a vector-based elevation data representation that models the surface using a network of non-overlapping triangles. In regions with complicated topography, where uniform grids could miss subtle variances, TINs are helpful. LiDAR point clouds, from which data is recorded in formats like LAS (LiDAR Data Exchange Format) or LAZ (compressed LAS), can also be used to create DEMs. Each point's 3D coordinates are stored in these formats, together with characteristics like classification and intensity.

A greyscale or colorized image, with each pixel's brightness or color intensity corresponding to an elevation value, is how a digital elevation model is visually displayed. Heights are shown using greyscale digital elevation models (DEMs), where darker regions correspond to lower heights and lighter regions to higher elevations. When color is not required in analytical applications, this straightforward depiction is frequently utilized. Color-relief digital Elevation Models (DERMs) facilitate visual differentiation between different elevations by representing distinct elevation ranges with a gradient of colors. Lower altitudes could be represented by the color green, mid-elevations by the color yellow, and higher elevations by the color brown or white. To give a perspective view of the terrain, DEMs can also be shown in three dimensions. Applications such as virtual reality, flight simulation, and landscape analysis benefit greatly from this visualization technique.

Because DEMs can properly depict the Earth's surface, they are widely employed in many fields. Among the most important uses is hydrological modeling, which models floodplains, stream networks, and watershed borders using DEMs. Hydrologists can forecast water flow patterns, flood threats, and drainage areas by examining elevation data. To calculate the slope, aspect, and curvature of the terrain—all important variables in land use planning, agriculture, and forestry—DEMs are necessary for terrain analysis. In urban planning, DEMs are used by planners to evaluate possible construction sites, examine how new constructions would affect the environment, and create infrastructure such as drainage and roadways. Thanks to their comprehensive data on slope steepness and terrain stability, digital elevation models (DEMs) assist in estimating the risk of natural hazards including earthquakes, landslides, and volcanic eruptions. By simulating soil erosion, sediment movement, and the suitability of habitat for distinct species, DEMs aid environmental studies.

Figure 2.5 shows as an example a DEM for the greater Montreal area. The data was obtained from Canada's online geospatial database. The topographical data was obtained from satellite-based measurements. The point spacing for this model is approximately 20 m.

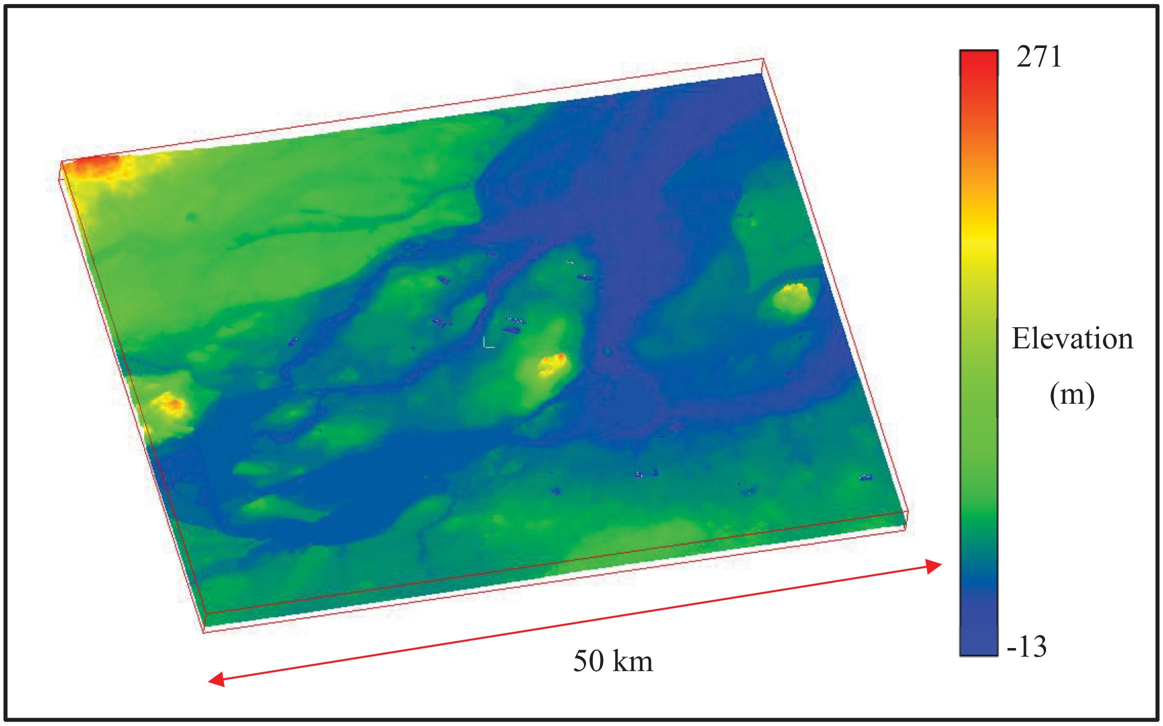

Figure 2.5 DEM of the greater Montreal area with color scale for elevation

Digital elevation models are useful resources for studying and assessing the surface of the Earth. For a variety of uses in GIS, engineering, environmental research, and urban planning, they offer a comprehensive, precise depiction of terrain heights. DEMs can be visualized in a variety of ways to fit the needs of the user and are available in a variety of forms, each appropriate for a particular function.

2.2 Typical surveying framework

An organized method of data collection, processing, analysis, and interpretation is typical of a remote sensing surveying framework, which aims to extract valuable information about the

Earth's surface and subsurface properties (Campbell & Wynne, 2011). The main elements of a typical remote sensing surveying framework are described as follows.

The mission planning phase of the surveying framework is when the remote sensing campaign's goals are established. The study region must be determined, suitable remote sensing instruments and sensors must be chosen, data acquisition parameters (such as temporal coverage, spatial and spectral resolution, flight, or orbit trajectories), logistical limitations, and environmental factors must be considered (Campbell & Wynne, 2011).

Data is acquired utilizing remote sensing platforms with sensors, such as satellites, airplanes, drones, or ground-based devices after the mission plan has been developed. Taking pictures, spectra, or other measurements of electromagnetic radiation that the Earth's surface emits or reflects within particular wavelength ranges might be considered data capture. The data collected must fully encompass the research region and fulfill the demands of the mission goals (Campbell & Wynne, 2011).

Preprocessing is performed on the obtained raw data to account for atmospheric effects, geometric distortions, radiometric discrepancies, and sensor artifacts. To guarantee the accuracy and consistency of the data for later analysis, preprocessing procedures may include calibration, orthorectification, atmospheric correction, and geometric correction (Schofield & Breach, 2007).

After processing, the data are exposed to image processing techniques to improve visualization, extract interesting features, and get ready for analysis. Picture processing methods to raise the quality and interpretability of the remote sensing imagery could include picture fusion, augmentation, filtering, and classification (Schofield & Breach, 2007).

To extract information about surface features, topographical characteristics, land cover, vegetation health, and other aspects of interest, the processed and augmented data are analyzed. To find patterns, trends, and anomalies in the dataset, data analysis techniques may be used, such as spectrum analysis, texture analysis, feature extraction, change detection, and classification (Schofield & Breach, 2007).

To obtain significant insights and share findings with stakeholders, the analyzed data are interpreted and produced visually. Based on the analysis results, interpretation entails identifying and characterizing surface features, land cover types, and environmental conditions. To portray the data in an intelligible and straightforward way, visualization techniques like interactive visualization, 3D rendering, and thematic mapping are used (Schofield & Breach, 2007).

Ultimately, ground truthing, accuracy evaluation, and comparison with reference data or field observations are used to evaluate and verify the information that has been obtained. This increases trust in the interpretation and decision-making process and guarantees the quality and dependability of the remote-sensing data.

In general, a typical remote sensing surveying framework consists of:

1. Data collection: Gathering information through remote sensing with a range of platforms and sensors.
2. Preprocessing: Error correction, sensor calibration, and georeferencing are steps in getting the raw data ready for analysis.
3. Data analysis is the process of using models and algorithms to extract pertinent information from preprocessed data.
4. Interpretation: Analyzing the data to find trends, correlations, and patterns.
5. Validation is the process of checking the interpreted data's accuracy and dependability against reference or ground truth data.
6. Knowledge production is the process of concluding and insights from verified data that can be used to investigate dynamic processes and the Earth's surface (Schofield & Breach, 2007).

2.3 LiDAR-based remote sensing techniques

LiDAR (Light, Detection, and Ranging) is an advanced form of remote sensing that uses laser light to measure distances and produce accurate, three-dimensional data regarding the features of the Earth's surface and those of other objects. Because of its accuracy and versatility, LiDAR is frequently employed in many different fields. The following is a thorough description of LiDAR-based remote sensing methods, including both their uses and underlying principles (Schofield & Breach, 2007).

Laser pulses are directed towards a target using the LiDAR remote sensing technique, and the duration of time it takes for the pulses to return to the sensor after reflecting off the target is measured. A laser source, a scanner, a receiver, and an optional GPS/GNSS system for precise positioning are usually the main parts of a LiDAR system. Measuring the interval of time between the production of a laser pulse and the detection of the reflected signal forms the basis of LiDAR technology. The distance to the target may be calculated thanks to this time delay and the speed of light. High-resolution, three-dimensional data on the Earth's surface, vegetation, buildings, and other objects can be produced by LiDAR systems (Schofield & Breach, 2007).

One of the most used LiDAR techniques is time of flight (ToF) analysis. It entails timing the separation of a laser pulse's emission from the signal's detection via reflection. The following formula is used to determine how far away the objective is:

$$Distance = \frac{Time \times Speed\ of\ Light}{2} \tag{2.1}$$

The laser pulse's round-trip travel is explained by dividing it into two. Flight time Because LiDAR devices are easy to use and efficient at gathering precise distance measurements over huge areas, they are widely employed. Applications needing precise topographic mapping and landscape modeling usually employ these technologies (Schofield & Breach, 2007).

The phase shift of the returned laser signal concerning the emitted signal is assessed using a technique called phase difference analysis, also called continuous-wave (CW) modulation. The distance that the laser pulse travels is precisely proportional to the phase shift. High accuracy distance determination is possible using the phase difference, particularly at shorter ranges. Compared to ToF analysis, this method can reach higher resolution and accuracy, although it involves extensive signal processing. Phase disparity LiDAR systems are frequently employed in high-resolution 3D mapping, engineering surveys, industrial metrology, and other fields where exact measurements are crucial (Schofield & Breach, 2007).

Figure 2.6 illustrates the concept of phase shift for laser pulse-based distance measurement. The process allows us to measure with high confidence the difference in terms of wavelength distance. Multiple pulses are emitted from the source with known frequency to generate different scales of phase difference. A pulse with a large wavelength (small frequency) provides the means to measure large distances. A high-frequency pulse on the other hand determines the precision of the tool and the number of reportable digits (Schofield & Breach, 2007).

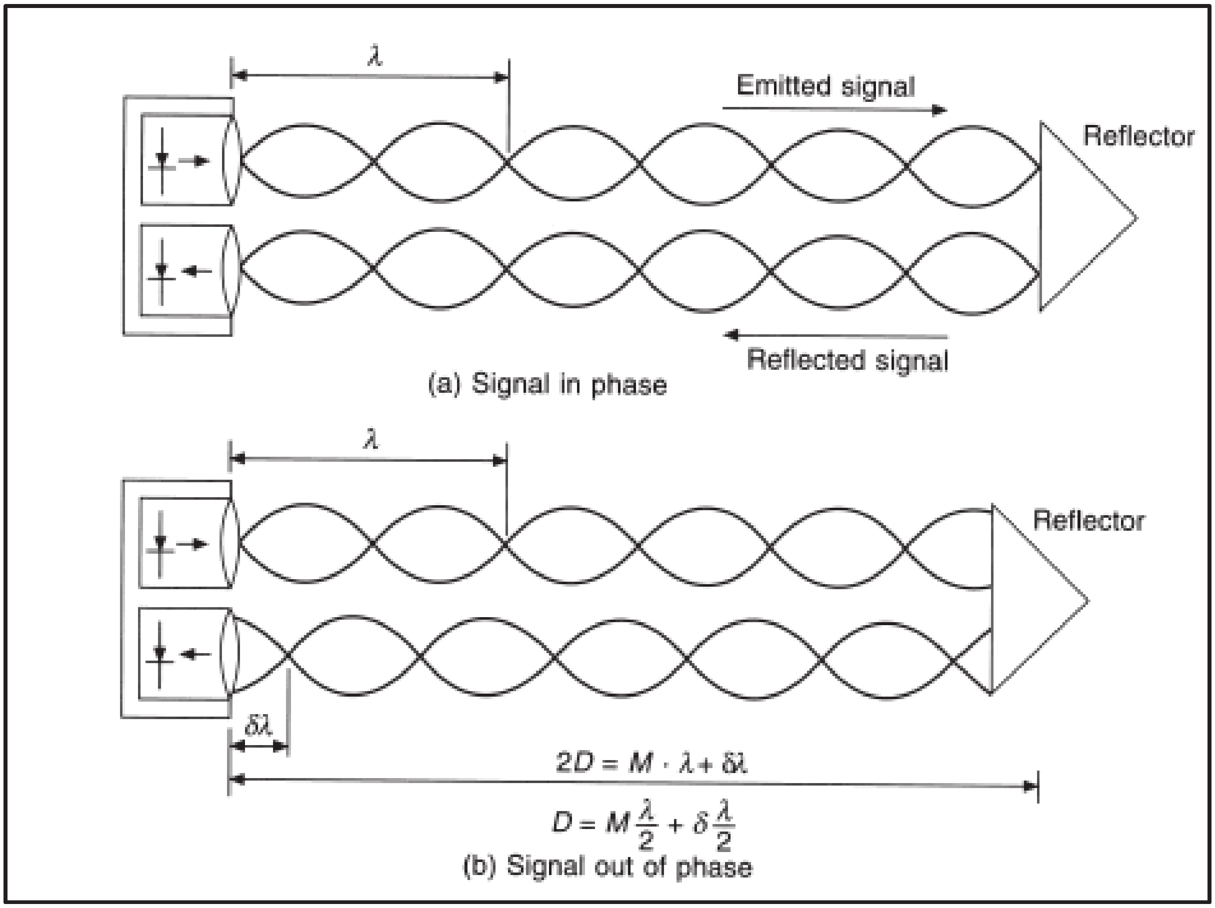

Figure 2.6 Conceptual representation of the phase difference method for distance measurements using a laser pulse
Taken from Schofield and Breach (2007, p. 132)

Based on how they function, LiDAR systems can be divided into two primary categories: pulse-based and CW LiDARs. Pulse-based LiDAR is a technology that measures the time it takes for a single, short-duration, high-power laser pulse to return. Because pulse-based LiDAR can collect data over long distances and through vegetation, it is frequently used for large-scale topographic mapping, forestry, and environmental monitoring. LiDAR with CW measures the phase difference of the returned signal after emitting a continuous laser beam. Usually, these systems are employed for shorter-range, high-precision tasks like small-scale 3D modeling and industrial inspections (Schofield & Breach, 2007).

Because of its versatility, LiDAR technology finds usage in many different fields, such as forestry, urban planning, agriculture, environmental monitoring, topographic mapping, and disaster management. Forestry is when the biomass, tree density, and canopy height of forests are measured using LiDAR. It supports the management, inventory, and observation of ecological changes in forests. Urban planning is when remarkable 3D models of urban landscapes, including structures, highways, and infrastructure, are produced using LiDAR data. These models support infrastructure upkeep, zoning, and urban growth. Agriculture involves LiDAR technology helping precision agriculture by giving comprehensive data on crop structure, properties of the soil surface, and topography of the land. The best procedures for crop management, fertilization, and irrigation are aided by this data. LiDAR technology facilitates the monitoring of environmental changes, including riverine systems, glacier dynamics, and coastal erosion. It offers useful information for evaluating and reducing natural dangers. Topographic Mapping involves LiDAR producing comprehensive digital surface models (DSMs) and elevation models (DEMs), which are necessary for comprehending topography and terrain features. Land-use management, building, and urban planning all employ these concepts. Disaster Management uses LiDAR mapping to determine the extent of damage caused by earthquakes, landslides, and floods. It supports risk assessment, recovery planning, and disaster response (Schofield & Breach, 2007).

The performance, accuracy, and applicability of LiDAR systems are determined by several crucial factors. To choose the best LiDAR system for a given work and to analyze the data it generates, it is imperative to comprehend these criteria. Range, accuracy, resolution, field of view (FoV), laser class, operating temperature, mobility and weight, scan rate, beam divergence, and power consumption are crucial factors to consider.

The FARO X130 will be used as an example to explain the parameters of LiDAR systems (Faro, 2021). The portable, high-precision 3D laser scanner, the FARO Focus3D X130 is made to measure details in three dimensions of intricate objects and settings. It is a member of the Focus3D line of laser scanners from FARO Technologies, which is renowned for its precision, use, and adaptability in a range of fields, including surveying, engineering, construction, and architecture. Rechargeable batteries allow the scanner to run continuously for up to 4.5 hours, making it convenient for fieldwork when a steady power source is not available.

Accurate 3D models are produced by the scanner and utilized for design, renovation, and construction scheduling. It offers accurate measurements for site surveys, facilitating the verification of as-built conditions and the tracking of development progress. Detailed 3D scans of historical sites and artifacts are captured using the FARO Focus3D X 130, which facilitates preservation and restoration activities. It is used to capture criminal scenes in three dimensions, offering precise and in-depth depictions for forensic examination and legal proceedings. To ensure quality control and that the components fulfill design criteria, the scanner aids in component inspection and measurement. Digital models of current parts are made via reverse engineering and can be utilized for improvement or reproduction.

The maximum distance that a LiDAR system can reliably measure is referred to as its range. It is an essential component in figuring out whether a LiDAR system is appropriate for a given application. LiDARs come in three different range types: short, medium, and long ranges. Typically, indoor applications or small-scale projects like robots or industrial metrology use short-range LiDAR. Applications such as environmental monitoring, infrastructure inspection, and urban planning are well-suited for mid-range LiDAR. Large-scale topography mapping, forestry, and aerial surveys are applications for long-range LiDAR. For instance, the FARO Focus3D X130 is appropriate for mid-range scanning applications because of its maximum range of 130 m.

The degree to which measurements resemble actual values is known as accuracy. It is a crucial parameter for applications where exact measurements are needed. Absolute accuracy is defined as the measurement's precision relative to the true value. The consistency of measurements made after repeatedly scanning the same place is known as relative accuracy. As an example, the FARO X130 ensures excellent precision in measurements with an accuracy of ±2 mm.

The density of the points in the point cloud produced by the LiDAR system is referred to as resolution. More points per unit area at a higher resolution yields data that is more accurate and detailed. The distance in a point cloud between neighboring points is known as spatial resolution. The smallest angle between two adjacent laser beams is known as the angular resolution. As an illustration, the FARO X130 can provide precise geographic data by reaching a point cloud density of up to 1.5 mm spacing per 10 m distance increments.

The viewable region that the LiDAR system captures is measured in terms of angle, or field of view. It establishes the LiDAR scan's coverage region. The angle in the horizontal plane is called the horizontal field of view. The angle in the vertical plane is called the vertical FoV. For instance, the 360-degree horizontal and 300-degree vertical field of vision of the FARO X130 enables thorough coverage of the surroundings.

The LiDAR system's laser's safety level is indicated by its Laser Class. International standards like the IEC 60825-1 specify it (Schulmeiser, 2015). An international standard that addresses the security of laser products is IEC 60825-1. The International Electrotechnical Commission (IEC), a global organization that develops and disseminates international standards for technology connected to electrical and electronic fields, publishes it. To safeguard users and the public from the risks associated with laser radiation, this standard specifies standards and guidance for the safe use of laser goods. The standard specifies the safety precautions that each class of laser requires. Some of these methods include personal protective equipment (PPE) use, administrative controls, and engineering controls. Engineering controls are components of the laser product that keep users safe from dangerous laser radiation exposure levels. Beam shutters, key switches, and interlocks are a few examples. Policies and processes known as administrative controls are implemented to guarantee the safe use of laser products. This covers user education, safety procedures, and limited access to high-power lasers. To prevent laser exposure, wear the proper laser safety eyewear and clothes as part of your PPE. According to the standard, laser items must have labels that include class, power output, and wavelength details. The laser product needs to have warning labels attached to it to alert users to any potential risks. The laser class, hazard symbols, and cautionary advice are all included on warning labels. The user manual provides comprehensive instructions on how to safely operate the laser product as well as maintenance schedules and safety precautions. The maximum emission levels that lasers in each class are permitted to have to guarantee their safety for the intended usage are specified in IEC 60825-1. These restrictions are determined by the exposure time and wavelength. Manufacturers are required to evaluate their laser products to make sure they meet the standard's emission limitations and safety criteria. Measurements of the laser's power output, beam properties, and safety features are required for this. A key component in guaranteeing the security of laser products is the IEC 60825-1 standard. It assists producers in creating laser devices that are safe to use in a range of settings, including consumer electronics, industry, and medicine. Manufacturers can reduce the dangers of laser exposure and shield users from potential skin and eye damage by conforming to this standard. It gives users peace of mind that the laser goods they use have been put through testing and found to be safe as long as they are used according to the manufacturer's instructions. Additionally, it offers guidance to safety authorities and employers on how to put into place efficient safety protocols and training courses for staff members using laser products. Three classes comprise the laser class. Class 1 is safe in all typical use scenarios. Class 2 is with natural aversion reactions and is safe for inadvertent sight. Extra safety measures are needed for Class 3 and up. Class 1 laser used by the FARO X130 is safe for the eyes to use in all operating circumstances.

The operating temperature range describes the set of environmental parameters that the LiDAR system can operate optimally. Low-temperature ranges are capable of functioning in chilly conditions. Heat can be tolerated in high-temperature ranges. The operating temperature range of the FARO X130 is -20°C to +50°C, making it suited for a variety of environmental settings. The LiDAR system's weight and portability play a crucial role in deciding how simple it is to move and set up in the field. Lighter systems are typically quicker to set up and more portable. For instance, the FARO X130 is lightweight and simple to set up in the field at only 5.2 kilograms.

The rate at which the LiDAR system can collect data is known as the scan rate. Points per second are typically used to measure it. Increased Scan Rates permit more comprehensive point clouds and speedier data collecting. The FARO X130 can scan at a maximum rate of 976,000 points per second.

The spread of the laser beam as it moves away from the LiDAR system is referred to as beam divergence. Greater spatial resolution and a finer point are produced by lower beam divergence. Low beam divergence works well for mapping that is precise and in-depth. Elevated beam divergence has less detail but covers wider areas. The beam divergence of the FARO Focus3D X130 LiDAR scanner is 0.19 milliradians (mrad). The scanner is appropriate for a range of mid-range scanning applications because of its relatively low beam divergence, which enables it to maintain excellent spatial resolution and generate detailed point clouds.

Particularly in field deployments, power consumption plays a significant role in defining the LiDAR system's operational duration and power requirements. The battery life of the machine dictates how long it may run between charges. Continuous operation requires a power supply. During operation, the FARO Focus3D X130 LiDAR scanner uses about 25 watts of power. The scanner's portability and ease of usage in a variety of field circumstances are facilitated by its comparatively low power consumption. The gadget can be used for extended field deployments without the need for a continual external power supply because it can run on a rechargeable battery that lasts for many hours.

2.4 Quantifiable uncertainty and error margins with LiDAR surveys

LiDAR technology is a very efficient way to create finely detailed 3D models of objects and environments. However, LiDAR is susceptible to a variety of error and uncertainty sources, just like any other measurement technology. Comprehending these sources is essential to measuring the precision and dependability of LiDAR data.

The main causes of mistakes in LiDAR surveys include instrumental errors, environmental factors, survey setup, and operational issues. Beam divergence, timing errors, and calibration mistakes are examples of instrumental errors. Imperfections in the calibration of the LiDAR system led to calibration mistakes. A calibration error specification that shows the possible departure from the true value is supplied by the manufacturers. This value typically represents the reproducibility of a given measurement at a given distance. The precision of the distance measurement might be impacted by beam divergence, which is the spread of the laser beam along its journey. Point cloud data is less accurate with a larger beam. Timing errors need to be considered because the precision of the timing mechanisms inside the LiDAR unit can have an impact on the accuracy of the time-of-flight measurement, which is essential for calculating distance.

Surface reflectivity, obstacles, and atmospheric conditions are examples of environmental factors. Changes in temperature, humidity, and air pressure are considered by atmospheric conditions, which can also have an impact on the speed of light and, by extension, distance measurements. The strength of the return signal is influenced by the reflectivity of the surface being scanned. Surfaces that are extremely dark or reflective can lead to measuring errors. Errors in the recorded data can occur when the laser beam is obstructed by dust or other airborne particles.

Among the survey setup and operating factors are the scan angle and range, scanner stability, and registration mistakes. The range and scan angle are errors that may be introduced by the LiDAR scanner's angle of contact with the surface, particularly at oblique angles. The scan's range also influences accuracy; measurements taken at greater distances are usually less accurate. The scanner's stability is considered when collecting data because any movement or vibration can result in serious inaccuracies. Additionally, there may be registration issues when combining numerous scans to produce a comprehensive model since these scans may not be accurately aligned and registered.

In the context of remote sensing and geotechnical monitoring, the smallest change or displacement that can be accurately detected and quantified by a monitoring system is referred to as the Level of Detection (LOD). It is essential for figuring out the system's sensitivity and precision, especially when it comes to seeing small movements or deformations that could be signs of bigger, more important events. Numerous error sources and environmental and monitoring system-related characteristics have an impact on LOD. Measurement repetition, calibration errors, beam divergence, surface roughness, registration errors, and positional precision are important factors that affect the LOD computation (Kromer et al., 2015). A measurement device's intrinsic error known as calibration error is frequently supplied by the manufacturer. It stands for the maximum precision at which the tool is capable of measuring distances or identifying changes. The number of times a measurement is repeated to lower random errors is referred to as measurement repetition. The accuracy of the measurement can be increased by doing more repeats. The laser measurement standard deviation can be computed by dividing the number of repeats by the calibration error (Brodu & Lague, 2012). The measurement precision is affected by the laser's lighted area and its beam divergence or spread, which is represented by the β angle (degrees). A larger beam spread may result in more uncertainty. The term "surface roughness" refers to the inherent imperfections of the surface under measurement. Parameters from point cloud data analysis, such as those from CloudCompare software, can be used to quantify it. Errors in aligning or integrating disparate point clouds can be attributed to registration errors, especially when a high-resolution reference scan is used. The merged dataset's overall accuracy is impacted by this inaccuracy. The degree of precision with which the scanning device's position is known as positional accuracy. It considers things like positioning system errors, total station errors, and GPS accuracy. Combining the separate error components yields LOD, provided that the errors are independent and have a normal distribution (Lague et al., 2013). Then, to guarantee a specific degree of confidence, the LOD is established as a multiple of the combined standard deviation. Taking into consideration several sources of error and uncertainty, the LOD offers a quantitative estimate of the lowest observable change by a remote sensing system. The reliable interpretation of monitoring data depends on the accurate calculation and understanding of the LOD, which guarantees that changes noticed are real and not just the result of measurement errors. A detailed computational method is presented in Chapter 4. Additional formulations have been proposed by Brody et Lague (2012) and Kromer et al. (2015).

2.5 Remote sensing assisted geohazard monitoring applications

The utilization of remote sensing technologies for geohazard monitoring has been increasingly popular owing to its capacity to provide extensive geographical and temporal data, which is imperative for comprehending and alleviating geohazard hazards. This section explores the several uses of remote sensing for geohazard monitoring, based on works by prominent scholars in the field.

LiDAR and InSAR (Interferometric Synthetic Aperture Radar) in particular are widely employed in remote sensing applications for landslip monitoring and detection (Hilley et al., 2004). InSAR is a remote sensing method that compares radar images acquired over time from slightly different sites to measure topography and ground deformation changes. Because it can precisely detect even the smallest disturbances in the ground, this approach is very helpful for monitoring geohazards including landslides, earthquakes, and volcanic activity. These methods make it possible to analyze slope stability, measure ground deformation precisely, and implement early warning systems. Different remote sensing methods, including LiDAR, InSAR, and optical images, have varying degrees of ability to record and analyze the dynamics of landslides (Miao & Zhang, 2012).

LiDAR is a type of remote sensing that produces high-resolution topographic maps by measuring distances with laser light. LiDAR sensors can be used to collect precise surface data by mounting them on ground-based devices, drones, or airplanes. LiDAR systems use laser pulses to collect data, and they time how long it takes for the pulses to return after striking the ground. Accurate 3D representations of the topography can be made thanks to this time-of-flight data. For topographic mapping, LiDAR generates high-resolution DEMs, which are crucial for locating and assessing landslide-prone locations. Researchers can identify minute changes in the terrain, such as vegetation displacement, slope movement, and ground deformation, which could be signs of landslip activity, by comparing LiDAR data taken at various dates. In addition to estimating the volume of material displaced by a landslip, LiDAR also sheds light on the size and effects of the landslip (Kromer et al., 2015).

By comparing phase differences between radar images collected from slightly different sites at different times, InSAR uses radar signals to determine ground displacement. Radar waves are emitted by InSAR sensors installed on satellites or aircraft to collect data, and the reflected signals are recorded. Through the analysis of phase variations between consecutive radar images, InSAR can pinpoint ground movements to the millimeter level of accuracy. When it comes to tracking slowly moving landslides and subsidence, InSAR is quite useful. It offers long-term, continuous data on ground movement. Because InSAR data can identify locations undergoing considerable ground movement before a large disaster, it can be used to construct early warning systems for landslides (Brodu & Lague, 2012).

Optical imagery is taking pictures of the surface of the Earth with aerial or satellite cameras. Although optical imagery is not as accurate as LiDAR and InSAR, it still offers useful contextual information. During data collection, optical sensors record both visible and near-infrared light, creating images that may be examined for variations in the terrain. Landslides, plant changes, and changes in land usage can all be visually identified with the aid of high-resolution optical pictures. Researchers can recognize landslip episodes, evaluate damage, and track recovery by comparing optical pictures captured at various dates (Brodu & Lague, 2012). For example, Hutchinson et al. (2021) provides a thorough method for using LiDAR to track landslides in hilly areas. The goal of this project is to create predictive models for the occurrence of landslides by analyzing slope movements using time-series LiDAR data. The writers hope to strengthen early warning systems and increase our understanding of landslip dynamics by utilizing the high-resolution capabilities of LiDAR technology. The investigation was conducted in a hilly area where landslides happen frequently. This region was chosen because of its geological features, past landslip incidents, and ease of access for the use of LiDAR technology. A series of LiDAR surveys were conducted during a designated time frame to record topographical changes. Terrestrial LiDAR scanners were used for these surveys, yielding high-resolution 3D point cloud data of the terrain. The writers periodically conducted LiDAR surveys to track variations in the slope. They were able to capture the dynamic aspect of the terrain and spot minute shifts that might point to possible landslip activity thanks to this method. To produce intricate 3D representations of the landscape, the gathered LiDAR data were processed. This required producing high-resolution point clouds, aligning several scans, and filtering out noise.

The authors identified variations in the slope over time by comparing the time-series LiDAR data (Hutchinson et al., 2021). To do this, it was necessary to examine how the points in the point clouds moved and pinpoint any notable movements. Algorithms were employed in the study to quantify the degree of slope deformation. Understanding the rate and direction of slope movements, which are crucial for comprehending the mechanisms causing landslides, was made possible by these data. Along with additional geographic and environmental data, such as rainfall patterns, soil composition, and geological structures, the deformation data from the LiDAR scans were combined. The development of predictive models was based on this extensive dataset. The authors created models that may anticipate the occurrence of landslides using statistical and machine-learning techniques. The time-series LiDAR data was used to validate these models, which were trained on historical data (Hutchinson et al., 2021). To facilitate early warning and risk mitigation, the predictive models sought to determine the circumstances in which landslides are likely to transpire. The results of the study demonstrated how well time-series LiDAR data work for landslip monitoring. The accuracy of the model, the dynamics of the land, and the identification of high-risk zones were among the main outcomes. Significant deformation was detected in some places of the slope by the change detection study, suggesting a higher likelihood of landslides happening. These areas were given top priority for additional research and oversight. Measurements of deformation yielded important information about the mechanisms underlying slope movements. The authors noted that some locations showed regular patterns of migration, which they speculated could be related to particular environmental cues like prolonged rain. The study's predictive models showed a high degree of accuracy in predicting landslip occurrences (Hutchinson et al., 2021). The models were able to reflect the intricate relationships between different elements driving landslides by adding LiDAR data. Hutchinson et al.'s research from 2021 has a big impact on risk management and geohazard monitoring. The study's prediction models can be incorporated into improved early warning systems to deliver timely notifications about possible landslides. This can facilitate preventive actions like evacuations and infrastructure augmentation, which can lessen the effects of landslides. The in-depth study of slope movement conducted with LiDAR data improves our knowledge of the dynamics of landslides. In hilly areas, this data can help with risk assessments and guide the development and planning of land use. To further improve the predictive models, the authors stress the importance of ongoing study and the incorporation of new data sources. To supplement the results of this study, future work may incorporate real-time LiDAR data and investigate the usage of other remote sensing technologies.

Tracking volcanic activity is yet another important use for remote sensing. Understanding and anticipating eruptions, reducing hazards, and safeguarding communities all depend on monitoring volcanic activity. For the analysis of volcanic processes, remote sensing technologies including LiDAR, InSAR, thermal infrared, and optical images are essential sources of data (Ramsey et al., 2013). With the use of these methods, volcanoes can be continuously and non-intrusively monitored, providing information on changes in topography, ground deformation, gas emissions, and temperature anomalies.

LiDAR creates high-resolution 3D representations of volcanic terrain by measuring distances using laser pulses. Mounted on drones or airplanes, LiDAR sensors shoot laser pulses and time how long it takes for them to return to the surface. This measurement of the time-of-flight aids in the creation of accurate DEMs. LiDAR helps locate features like craters, lava flows, and volcanic domes by providing precise topographic maps of volcanic structures. LiDAR compares pre- and post-eruption DEMs to determine the volume of material that has erupted. Frequent LiDAR surveys identify surface variations in the volcano that point to possible eruption areas and magma migration.

Radar waves are emitted by InSAR sensors on satellites or aircraft, which then record the reflected signals. Subsequent radar pictures' phase differences can be used to precisely pinpoint ground deformation to the millimeter. Volcanic inflation, deflation, and magma intrusion all generate ground deformation that is detectable by InSAR. Because InSAR data can reveal areas of considerable ground movement before eruptions, it is essential for the development of early warning systems. Continuous, long-term monitoring of volcanic activity is made possible by InSAR, which helps with risk reduction and hazard assessment.

By detecting heat emitted from the Earth's surface, thermal infrared photography makes it possible to identify thermal anomalies connected to volcanic activity. Temperature maps are produced by capturing infrared radiation using thermal sensors on satellites, airplanes, or ground-based platforms. Hot places on volcanoes, such as fumaroles, active lava flows, and volcanic vents, can be identified using thermal photography. Changes in thermal patterns can be used to identify current volcanic activity changes or new eruptions. To help with hazard assessment and evacuation planning, thermal photography records the velocity and breadth of lava flows (Patrick et al., 2019).

Optical photography offers useful contextual data for tracking volcanic activity. Visible and near-infrared light are captured by optical sensors, creating images that may be examined for variations in the topography. High-resolution optical pictures are useful for tracking vegetation changes, monitoring land usage, and identifying volcanic features. New lava flows or ash deposits are examples of how variations in volcanic activity can be seen by comparing optical photographs captured at various dates.

Kromer et al. (2020) aimed to improve the monitoring of volcanic hazards by combining data from remote sensing with observations made on the ground. The main goal is to show how well thermal imaging and LiDAR data can be used to track active volcanoes in real time. The goal of this integration is to deliver fast and comprehensive data that is essential for comprehending volcanic activity and reducing related hazards. Temperature changes on the volcanic surface were recorded using thermal cameras. Finding hotspots and changes in thermal activity that can lead to an imminent eruption depends on these fluctuations. To produce high-resolution 3D representations of the volcanic terrain, LiDAR technology was used. This information is useful for tracking variations in the volcano's shape over time, as well as surface deformation and other physical changes. To gather further information on the volcano, such as ground movements, gas emissions, and seismic activity, sensors and instruments situated strategically around the volcano were used. Together with the data from remote sensing, these observations were combined to create a comprehensive picture of the volcanic activity. To monitor active volcanoes, the combination of thermal imaging and LiDAR data proved to be quite successful. While the LiDAR data offered accurate measurements of surface changes and deformations, the thermal data assisted in locating heat sources and variations in thermal patterns. Real-time analysis and monitoring of volcanic activity were made possible by the combined data. For early warning systems and disaster preparedness to function properly and for authorities to respond promptly in the event of increasing volcanic activity, real-time capacity is essential. Through the integration of LiDAR and thermal data with on-the-ground observations, the researchers created predictive models capable of predicting volcanic eruptions. To more accurately forecast possible eruptions, these models incorporate several variables, including variations in temperature, surface deformations, and seismic activity. A thorough understanding of volcanic behavior is made possible by the integration of many data sources. To effectively analyze the risks and potential repercussions of volcanic eruptions, a holistic approach is needed. Safety precautions and evacuation strategies are much improved by enhanced monitoring and real-time analysis. Prompt identification of possible eruptions enables prompt alerts and the establishment of safety measures to safeguard populations residing close to active volcanoes. The study emphasizes the necessity of ongoing investigation and advancement in the field of monitoring volcanic hazards. The accuracy and dependability of monitoring systems can be further increased by integrating innovative technologies and approaches.

Monitoring and controlling floods also heavily rely on remote sensing. Flood control and monitoring are essential for reducing the effects of floods, safeguarding people, and property, and improving readiness for emergencies. LiDAR, InSAR, radar, optical images, satellite altimetry, and other remote sensing technologies provide useful information for the assessment, management, and real-time monitoring of flood events (Twele et al., 2016). These methods provide efficient reaction and planning strategies by enabling the detection of flood extent, water levels, and changes in the landscape. LiDAR offers precise topographic maps that are useful for locating river basins, drainage patterns, and places that are vulnerable to flooding. Floodplain delineation, flood risk assessment, and flood scenario modeling are all done with LiDAR data. LiDAR facilitates the evaluation of an infrastructure's susceptibility to flooding, including roads, levees, and bridges. Ground subsidence or uplift is detected by InSAR sensors, which can reveal variations in water levels and possible flood hazards. The extent of floodwater can be mapped with the aid of InSAR photos, particularly in regions with continuous cloud cover where optical photography is less useful. Because InSAR data can detect locations at risk of floods owing to ground deformation, it is helpful in the development of early warning systems.

Using radar sensors to take pictures of the Earth's surface allows radar imagery to offer data in any weather situation and even through clouds. Satellite radar sensors, like Sentinel-1, use microwave emissions and recorded reflected signals to create images.

The European Space Agency (ESA) designed Sentinel-1 as a satellite mission as part of the Copernicus Programme, to provide rapid, accurate, and easily accessible Earth observation data. Sentinel-1A and Sentinel-1B, two satellites in the mission's constellation, are equipped with sophisticated SAR equipment (European Space Agency, n.d.). These satellites are extremely beneficial for a variety of applications since they continuously provide day and night, all-weather radar imaging. Sentinel-1 provides fine-grained radar images of the Earth's surface while operating in the C-band frequency, or at 5.405GHz. Continuous data collecting is ensured by SAR’s ability to operate in all weather conditions and penetrate clouds. The radar's capacity to record information in single and dual polarization modes (VV, VH, HH, and HV) improves its capacity to differentiate between various surface elements and materials. The standard mode with a swath width of 250 km and a spatial resolution of 5x20 m for the majority of land and coastal applications. With a 400 km swath width and 25x100 m spatial resolution, Extra-Wide Swath (EWS) is mostly utilized for marine surveillance. Higher spatial resolution imagery (5x5 m) over a smaller area (80 km) is provided by Stripmap (SM). Wave is used to monitor ocean waves by taking 5x5 m quality pictures of small areas measuring 20x20 km. With a repetition cycle of 12 days for every satellite, Sentinel-1 offers worldwide coverage, giving the constellation a total revisit duration of 6 days. The capacity to revisit an area frequently is essential for tracking dynamic environmental processes. Monitoring of land deformation, mapping of forests, land use changes, and agricultural practices are all included in this satellite program. It is used for ship detection, oil spill monitoring, sea ice mapping, and ocean wave analysis. It also provides vital data for mapping floods, landslides, assessing earthquake damage, and tracking volcanic activity. Additionally, by keeping an eye on ice sheet dynamics, sea level rise, and changes in polar regions, they aid in the study of the effects of climate change. InSAR applications use Sentinel-1's SAR pictures to determine ground movement with millimeter accuracy. Monitoring tectonic activity, landslides, and subsidence requires this. Through the Copernicus Open Access Hub, Sentinel-1 data is publicly accessible to users globally, supporting commercial applications, scientific research, and environmental monitoring (European Space Agency, n.d.).

Even in overcast or nighttime conditions, the extent of flooding can be seen and mapped using radar imagery. Radar sensors provide real-time data for flood management by measuring variations in the water levels in rivers, lakes, and reservoirs. The assessment of soil moisture content, which is essential for understanding hydrological processes and forecasting flood hazards, is made possible using radar data.

Optical imaging provides important visual data for flood monitoring by taking pictures of the Earth's surface with satellite or aerial cameras. High-resolution optical images are useful for mapping the extent of flooding, locating impacted areas, and evaluating vegetation and infrastructure damage. Optical imagery is used to track changes in land use and cover, which can affect floodplain management and flood risk. Optical pictures offer vital information for recovery planning, resource allocation, and emergency action.

Using radar or laser altimeters on satellites, satellite altimetry measures the height of the Earth's surface and provides information on surface elevations and water levels. To determine surface elevations and water levels, altimeters aboard satellites like Sentinel-6 and Jason-3 monitor the amount of time it takes for radar or laser pulses to travel from the satellite to the Earth's surface and back. Altimetry data is essential for forecasting and managing floods because it helps keep track of the water levels in rivers, lakes, and reservoirs. The study of sea level rise and its effects on storm surges and coastal flooding is aided by altimetry observations. To simulate and forecast flood events, altimetry data is included in hydrological models, enhancing flood risk assessments and management plans.

The ESA’s Copernicus program includes the satellite mission Sentinel-6, which is dedicated to high-precision ocean altimetry (European Space Agency, n.d.). With previously unheard-of accuracy, this mission seeks to measure wind speed, wave height, and sea surface height over the oceans. Sentinel-6, also called Jason Continuity of Service, or Jason-CS, is a mission of NASA that maintains the high-precision ocean altimetry data collection that was started by Jason-1, 2, and 3 and Topex/Poseidon (Torres et al., 2012). One of the main characteristics is the high-precision ocean altimetry. The height of the ocean surface about the geoid is measured by the sea surface height, which provides vital information for tracking climate change, especially in terms of comprehending sea-level rise. Significant wave height and ocean surface wind speed are tracked by the Wave Height and Wind Speed, which helps with marine weather forecasting and maritime safety. A Poseidon-4 radar altimeter, which compensates for ionospheric delay and operates on two frequencies (Ku-band and C-band), is installed on the satellite (Torres et al., 2012). The onboard AMR-C (Advanced Microwave Radiometer - Climate Quality) instrument detects atmospheric water vapor, which is crucial for improving the accuracy of sea surface height measurements by compensating for signal delays brought on by atmospheric circumstances. To determine an object's accurate orbit, Sentinel-6 combines GPS, DORIS (Doppler Orbitography and Radio positioning Integrated via Satellite), and a laser retroreflector. Ensuring the accuracy of altimetric readings is contingent upon this. Sentinel-6A, which was launched in November 2020, and Sentinel-6B, which is scheduled to launch five years later, are two identical satellites that will be part of the mission, guaranteeing a continuous data record for at least ten years (European Space Agency, n.d.). Sentinel-6 offers vital data for researching ocean currents, eddies, and tides; improving climate models and forecasts; and tracking global sea-level rise and its causes (such as glacier loss and thermal expansion). The ESA, European Commission (EC), European Organization for the

Exploitation of Meteorological Satellites (EUMETSAT), NASA, National Oceanic and Atmospheric Administration (NOAA), and Centre National d'Études Spatiales (CNES) are among the many international partners involved in the Sentinel-6 mission. Sentinel-6 data is essential for many applications, including oceanography, meteorology, climate research, and environmental monitoring. Sentinel-6 facilitates decision-making in the areas of catastrophe risk reduction, maritime resource management, and climate change adaptation by providing high-precision, timely data (European Space Agency, n.d.).

A satellite mission called Jason-3 is a component of a multinational effort to track sea surface height. It is the next in line of high-precision ocean altimetry missions, which were started by Jason-1 and Jason-2 and then continued by TOPEX/Poseidon (National Oceanic and Atmospheric Administration, n.d.). The long-term sea surface height data record is essential for comprehending variations in sea level, ocean circulation, and climate change. The Jason-3 mission is intended to maintain this record. Jason-3 has very good precision when measuring the height of the ocean's surface. Understanding ocean currents, monitoring the rise in sea level globally, and enhancing climate models all depend on these measurements. The Poseidon-3B radar altimeter, which uses both Ku-band and C-band frequencies, is installed on the satellite. By doing this, the satellite can improve the accuracy of observations of sea surface height by compensating for ionospheric delays. The onboard AMR (Advanced Microwave Radiometer) detects atmospheric water vapor, which is essential for adjusting for atmospheric conditions-related signal delays and enhancing measurement accuracy. To determine an exact orbit, Jason-3 combines GPS, DORIS, and a laser retroreflector array. For accurate altimetric measurements, a precise understanding of the satellite's position is necessary. Launched in January 2016, Jason-3 is intended to run for a minimum of five years, continuing the high-precision ocean altimetry data record that its predecessors started. The information supplied by Jason-3 is used to improve weather, climate, and ocean models and predictions, monitor global sea-level rise and its causes, such as ice melt and thermal expansion, and research ocean currents, eddies, and tides. EUMETSAT, NOAA, NASA, and CNES collaborated internationally to create Jason-3 (European Organisation for the Exploitation of Meteorological Satellites, n.d.). For a variety of uses, including climate research to advance our knowledge of the Earth's climate system and improve projections of climate change, the Jason-3 mission delivers essential data. Oceanography is the study of ocean circulation patterns and how they affect weather and climate. The goal of meteorology is to enhance weather models and forecasts. The purpose of environmental monitoring is to assist with disaster risk reduction and marine resource management (National Aeronautics and Space Administration, n.d.).

Lague, Brodu, and Kromer's (2019) work provides evidence of the use of high-resolution remote sensing data in flood risk assessment. The researchers sought to identify flood-prone areas and examine the consequences of floods in both urban and rural settings using satellite images and radar data. The comprehensive methodology used in this study demonstrates how several remote sensing approaches can be integrated to improve the precision and effectiveness of flood risk management. High-resolution satellite photos were gathered to give a comprehensive visual record of research regions. The changes in surface features and land cover before and after flood episodes were identified with the use of these photographs. During flood episodes, surface deformation and water extent were recorded using SAR data. Because SAR can see through clouds and provide data in all weather, it is especially helpful for monitoring floods. To assure precise spatial alignment and improve the quality of picture preprocessing, satellite images underwent geometric and radiometric modifications. Reliable change mapping and detection depend on this step. Ground displacement and water levels were measured using InSAR techniques to perform SAR Interferometry. By comparing several SAR images obtained at various times, the researchers were able to identify minute variations in water distribution and surface height. The scientists used satellite photos taken before and after the flood to conduct a change detection investigation. This analysis highlighted notable changes in land cover to identify locations impacted by flooding. To determine the extent of the flooding, SAR data was employed. Precise mapping of flooded areas was made possible by the radar signal's capacity to distinguish between surfaces covered in water and those that are dry. The study evaluated how floods affected both rural and urban areas. The analysis in urban areas concentrated on damage to utilities, buildings, and roadways. The researchers assessed the effects on natural vegetation, agricultural land, and water resources in rural locations. By merging land use and population density data with flood maps, the researchers were able to pinpoint high-risk areas. Planning for disaster response and flood mitigation was given priority in these areas. Flood maps have been much more accurate since high-resolution satellite images and SAR data were combined. The accurate determination of flood boundaries and the identification of impacted areas were made possible by the comprehensive spatial resolution. The study brought attention to how susceptible urban infrastructure is to flood. Low-lying structures, roads, and bridges were especially vulnerable to flood damage. Urban planners need this information to create robust infrastructure designs. The study found significant effects on natural ecosystems and agricultural lands in rural areas. Farmers lost money as a result of crop production disruptions caused by floodwater. Additionally, local wildlife was impacted by the flooding of natural ecosystems. For disaster management organizations, the thorough flood risk maps produced by this study are invaluable resources. These maps make initiative-taking planning easier, allowing authorities to more effectively allocate resources and put flood mitigation plans into action. The usefulness of high-resolution remote sensing data in flood risk assessment is demonstrated by this case study. The researchers were able to map and analyze the effects of flooding precisely for both rural and urban areas by using satellite imagery and SAR data. The knowledge gathered from this research is crucial for improving flood preparedness, directing the construction of infrastructure, and promoting sustainable land use planning.

Assessing seismic hazards entails determining how likely it is that an earthquake will induce ground shaking and related impacts in a particular location. Planning emergency responses, building earthquake-resistant structures, and lowering seismic risks all depend on this assessment. To comprehend and measure seismic dangers, a variety of methods are used, such as probabilistic analysis, geological surveys, and remote sensing. It is essential to locate and map active faults. Locating fault lines and comprehending their geometry requires field surveys, aerial photography, and remote sensing (such as LiDAR). Understanding the magnitudes and recurrence periods of previous earthquakes is made easier by analyzing historical earthquake data. Forecasting future earthquake activity requires this information. The decay of seismic waves as they move away from the source is predicted by attenuation relationships. They consider variables including distance from the fault, earthquake depth, and geological conditions, and are based on past earthquake records. Rock and soil conditions in a given area can greatly intensify seismic vibrations. Analyzing site reactions entails determining how various ground conditions impact surface seismic shaking. The Probabilistic Seismic Hazard Analysis (PSHA) determines the probability that a site may experience more ground shaking than expected at a particular time interval. This entails combining data on ground motion prediction, seismic source information, and site response. The likelihood of surpassing different intensities of ground shaking is shown by hazard curves. They provide information on design standards and building codes. Using historical seismicity and known faults as a basis, deterministic seismic hazard analysis (DSHA) models certain earthquake scenarios. Worst-case estimations of ground shaking for a certain area are provided using this method. The largest earthquake that is reasonably expected to occur on a given fault or within a certain seismic source zone is known as the maximum credible earthquake.

Surface ruptures and fault lines can be located and mapped with the use of high-resolution LiDAR data (Nissen et al., 2012). This is especially helpful in urban or heavily forested areas where faults could be hidden. DEMs created with LiDAR data offer comprehensive topographic data that is essential for comprehending the geometry of faults and evaluating the risk of landslides caused by seismic activity. LiDAR-derived DEMs offer comprehensive topographic data that are essential for comprehending fault geometry and evaluating the risk of landslides caused by seismic activity.

The ground displacement brought on by seismic activity is measured by InSAR. It is especially helpful in identifying and measuring minute ground motions that could occur either before or after an earthquake. The distribution of slip along a fault during an earthquake can be estimated using InSAR data, which sheds light on the mechanics of fault rupture. Seismic waves are also used in seismic tomography to provide three-dimensional images of the Earth's interior. This method aids in understanding the geological context of seismic sources and aids in the identification of underlying fault structures. The extent of earthquake damage is evaluated using high-resolution satellite photography. Planning for emergency response and recovery depends on this information. Surface fractures and other ground disturbances connected to earthquakes can be identified with the aid of satellite pictures.

A thorough investigation of the use of remote sensing technologies for seismic hazard assessment was conducted by Fey et al. (2018). Their research was primarily concerned with measuring ground displacement and identifying fault lines using LiDAR technology. This data is useful for risk mitigation and hazard assessment, making it essential for earthquake preparedness and response. LiDAR data with high resolution was gathered across multiple earthquake zones. Detailed topographic maps, made possible by LiDAR technology, are crucial for locating minute surface details connected to fault lines. The study used satellite pictures and aerial photos in addition to LiDAR to supplement the LiDAR data. The results from the LiDAR surveys were cross-referenced and validated with the aid of these data sources. High-resolution DEMs were produced through the processing of LiDAR data. These models illustrated topographical changes while offering a detailed depiction of the Earth's surface. The researchers used DEMs to analyze variations in surface elevation and geomorphological features, which allowed them to identify fault lines. Because of LiDAR's accuracy, even small fault lines that are difficult to see with conventional surveying techniques can be found. To calculate the displacement of the ground, LiDAR data from several periods were compared. By using a method called LiDAR differencing, the researchers were able to measure the amount of displacement along fault lines. A thorough fault line database was created by mapping the detected fault lines. Each fault line's location, length, and activity were all included in this database. The degree of fault line activity was evaluated using the ground displacement data. The researchers were able to ascertain each fault line's possible seismic hazard and migration pace by tracking the displacement over time. The study assessed how identified fault lines might affect important infrastructure and metropolitan areas. High-risk seismic event zones were determined to be those close to active fault lines. The researchers developed seismic hazard maps by combining information on land use and population density with fault line and displacement data. These maps identified high-risk regions that need focused attention on earthquake mitigation and preparedness. The mapping and identification of fault lines were greatly enhanced by the use of high-resolution LiDAR data. The capacity to locate tiny fault lines that were previously unknown allowed for a more thorough understanding of seismic threats. Ground displacement along fault lines could be precisely measured thanks to LiDAR differencing techniques. This data is essential for estimating the likelihood of future seismic events and determining the degree of fault activity. Seismic hazard maps were made using the precise fault line and ground displacement data. When creating plans for earthquake preparedness and response, engineers, urban planners, and emergency management organizations can all benefit greatly from these maps. Urban areas and vital infrastructure close to active fault lines were designated as high-risk zones by the study. To prioritize risk mitigation measures and guarantee the security of inhabitants and infrastructure, this knowledge is crucial. This case study emphasizes how important remote sensing technologies are for assessing seismic hazards, especially LiDAR. LiDAR is a valuable tool for improving earthquake preparedness and response since it can map fault lines in great detail and monitor ground displacement. The knowledge gathered from this research is crucial for enhancing the evaluation of seismic hazards and developing risk-reduction plans.

2.6 High temporal-resolution monitoring solutions

As elaborated above, remote sensing tools provide intuitive and non-intrusive solutions for high spatial resolution monitoring. These solutions have limited applicability for high temporal resolution applications due to the shear amount of data that would be generated (Clark et al., 2022). In such instances, conventional instrumentation is often preferred to offer rapid response during instability events. For example, growing developments have been observed around fiber optic installations to monitor deformation profiles along dikes, dams, and earth fill systems (i.e. Inaudi et al. 2023). These multi-kilometer cable networks provide high spatial resolution with deformations and can function as trip-wire alarm systems triggered by excessive deformation rates.

Remote sensing-based high temporal resolution systems, or near real-time systems, are available in some limited capacity. Doppler radars have been used at multiple locations to monitor at high temporal frequency the movement rate of structures and slopes. Carla et al.

(2023) present radar-based monitoring results of the extensively studied Ruinon rockslide in Italy. The radar systems require georeferenced reflective surfaces to accurately target monitored surfaces. The spatial resolution of this technology is therefore limited to a large extent, and often necessitate (although not systematically) the installation of a reflective surface. It is noted also that such radar systems present prohibitive costs in the multi hundred of thousands of dollars per apparatus (Luzi, 2010). The current state of application and availability of these tools in part led to the research formulation presented in this study.

CHAPTER 3

RAPID-DEPLOYMENT HIGH TEMPORAL RESOLUTION TLS MONITORING SYSTEM

3.1 Desired specifications of the prototype and rationale

The essential characteristics and functions needed for the successful deployment and operation of the rapid-deployment high temporal resolution LiDAR monitoring system prototype are listed to properly explain the desired specifications of the system and its justification.

- **Low cost**: The prototype ought to use easily accessible and reasonably priced parts to reduce implementation costs. This covers readily available LiDAR sensors, microcontrollers, and additional hardware parts. For the monitoring system to be widely adopted and scalable, cost reduction is crucial.
- **High temporal resolution**: For the system to effectively monitor quick changes in geohazard conditions, it must be able to capture data at high temporal resolutions. To take regular photos of the monitored region, quick scanning technology and effective data-collecting processes are needed.
- **Adequate spatial resolution**: Point spacing generated by the tool must be sufficiently small to allow for systematic scan placement without complex or costly geo-referencing.
- **Portability and ease of transportation**: For quick deployment in isolated or remote areas vulnerable to geohazards, portability is essential. The system ought to be lightweight and small enough to fit into a regular car or even a bag. To reduce downtime during deployment, quick assembly and disassembly processes are necessary.
- **Rapid assembly**: The prototype must have a modular design that makes rapid assembly possible without the need for specialist equipment or knowledge. Connectivity between components that plug, and play simplifies setup processes, allowing users to promptly set up the system for short-term and long-term monitoring programs or emergency scenarios.

- **Robustness and durability**: The monitoring system needs to be able to survive the severe weather that is common in geohazard-prone areas, including high humidity, low temperatures, and mechanical shocks. In demanding field situations, dependable operation and longevity are guaranteed by robust construction and strong components.
- **Flexible mounting options**: The device can be adjusted to distinct types of terrain and monitoring situations thanks to adjustable mounting choices. Tripod mounts for fixed observation, car mounts for mobility surveys, and drone integration for aerial surveillance are a few examples of this. Varying the mounting configurations allows the system to be more adaptable and useful in a variety of settings.

The justification for these intended requirements arises from the intrinsic difficulties linked to the traditional methods of geohazard surveillance. Conventional monitoring systems are limited in their accessibility and scalability, especially in environments with limited resources, because they sometimes necessitate large investments in specialized labor, infrastructure, and equipment. The suggested prototype solves these shortcomings and provides a workable substitute for prompt and effective geohazard monitoring by placing a strong priority on cost-effectiveness, mobility, and high-temporal precision.

The low cost makes it possible for monitoring systems to be adopted and deployed more widely in various geographic locations, including developing nations and isolated communities with little financial resources. A high temporal resolution minimizes the possibility of disastrous outcomes like landslides, rockfalls, or slope failures by ensuring prompt identification and reaction to dynamic geohazard events. Users may quickly deploy the monitoring system in emergency scenarios or for short-term monitoring campaigns due to its portability and easy assembly, which improves overall responsiveness and efficiency in hazard mitigation activities.

Additionally, the system’s sturdy design and versatile mounting options improve its durability and flexibility in response to changing climatic conditions and monitoring needs. A scalable and easily accessible solution for initiative-taking geohazard monitoring and risk management to researchers, mining companies, and community organizations can be provided by integrating these elements into the prototype.

3.2 Components of the prototype

The prototype monitoring system is made up of the following parts, which together allow for high-resolution, quick deployment geohazard monitoring in a range of environmental settings. Every part is essential to maintaining the system's reliability, stability, and functionality while it is in use.

The Blickfeld Cube LiDAR scanner, the main sensing device in the monitoring system that records precise spatial data of the monitored regions, is the most crucial component of the entire system. It will measure the distances and generate three-dimensional point clouds using laser beams, making precise geohazard condition detection and analysis possible. More details on this laser scanner will be provided in Section 3.4.

3.2.1 Tripod

The tripod is a three-legged structure that is used to raise and stabilize machinery or instruments. As shown in Figure 3.1 below, with its adjustable height and orientation, this stand provides a secure mounting platform for the LiDAR scanner, enabling accurate positioning. Even under difficult circumstances and uneven terrains, it guarantees continuous and reliable data capture. The tripod selected for this work was acquired at Home Hardware. The model is not as important as the underlying features. It requires proper coupling mounts for the centered steel rod, and some pinpoints along the legs. A conventional survey tripod would have also been an option considered.

Figure 3.1 Tripod used for Prototype

3.2.2 Raspberry Pi

Small, inexpensive, and multipurpose, the Raspberry Pi is a single-board computer that is extensively utilized in a variety of computing and electronics projects. It is a fundamental part of the prototype and is essential to the automation and management of the remote sensing apparatus. An ARM-based central processing unit (CPU), which is commonly included with Raspberry Pis, offers enough processing power for activities including data processing, peripheral device control, and sensor connection. Depending on the model, it has different quantities of RAM that allow for multitasking and the running of intricate algorithms. A variety of sensors, motors, and other electronic parts can be interfaced with the Raspberry Pi thanks to its GPIO (General Purpose Input/Output) pins. It is perfect for remote monitoring applications because it has Ethernet, Wi-Fi, and Bluetooth integrated right in for connection. Data and the operating system are kept on a microSD card, which is readily upgraded or changed. The Raspberry Pi functions as the CPU in the remote sensing prototype, directing LiDAR's operations and overseeing the gathering and archiving of data. Additionally, it can evaluate data locally before sending it to a central server or cloud for additional analysis, automate the scanning process, and start activities based on sensor inputs. The Raspberry Pi is a great option for incorporating into field-based monitoring systems when space and power resources are restricted because of its small size, low power consumption, and flexibility. As a vital component of the experimental setup, it also permits the creation of custom Python scripts and other software required for data gathering and processing.

A real-time clock (RTC) module, commonly referred to as the Raspberry Pi Clock Model 4, is used for this prototype to give the monitoring system precise timekeeping capabilities. It guarantees synchronized timestamps for information gathered from other sensors and the LiDAR scanner, allowing for temporal alignment and correlation with outside triggers and events. The small and dependable RTC module made especially for use with Raspberry Pi single-board computers is the Raspberry Pi Clock Model 4, as shown in Figure 3.2 below. It has a battery-operated clock chip (DS3231 or DS1307, for example) that keeps the time and date correct regardless of the Raspberry Pi operating system. The GPIO pins on the Raspberry Pi single-board computer allow the Raspberry Pi Clock Model 4 to be easily connected to it and integrated into the electronics configuration of the monitoring system. It uses the Inter-integrated Circuit (I2C) protocol to connect with the Raspberry Pi and provides precise timekeeping. Advanced scheduling and recording features of the Raspberry Pi Clock Model 4 enable users to automate data acquisition operations or schedule recurring monitoring sessions based on predetermined criteria or time intervals. By guaranteeing precise temporal synchronization of monitoring data, it improves the monitoring system's overall performance. To connect monitoring data with outside phenomena like rainfall, seismic activity, or temperature swings, accurate timekeeping is essential. Precise temporal alignment of data is made possible by the Raspberry Pi Clock Model 4, which improves the system's ability to identify and assess geohazard conditions over time. Also, compared to previous models, the Raspberry Pi Clock Model 4 has better precision, guaranteeing reliable timekeeping performance even in harsh environmental circumstances. Because of its small size and low power consumption, it is perfect for embedded applications where energy efficiency and space are critical, like geohazard monitoring systems.

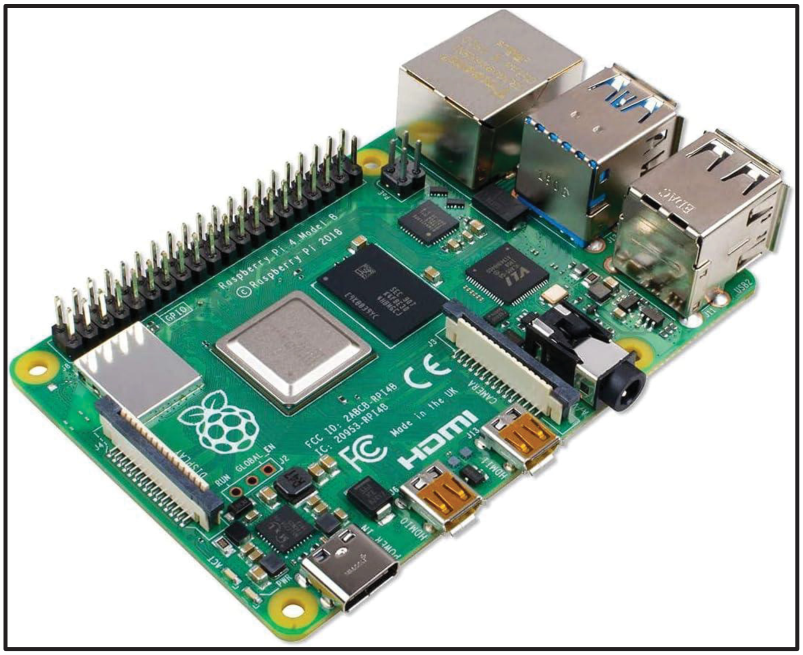

Figure 3.2 Raspberry Pi Clock Model 4

3.2.3 Battery

The LiDAR scanner and related electronics are powered primarily by the 12 Volt, 18 Amp-hour battery, shown in Figure 3.3 below. It is a rechargeable power source, which is frequently used to power portable gadgets, and supplies enough energy to support prolonged monitoring activities, guaranteeing ongoing data collection and system operation.

Figure 3.3 12 V 18 A-hr Battery

3.2.4 Hardware used for prototype

Heavy-duty fasteners called anchor bolts are used in the prototype monitoring system to fasten the tripod to the ground, improving stability and resistance to wind and other external forces. As shown in Figure 3.4, they guarantee that, when is in use, the monitoring system stays securely fixed in place.

Figure 3.4 30-inch Earth Anchor Set

The LiDAR scanner and other components are secured with cables that will have their tension adjusted using the turnbuckle. It entails two threaded eye bolts spaced apart by a central body that may be moved to change the bolt-to-bolt spacing. The specific turnbuckle used is a jaw and eye, galvanized, and has a threaded diameter of 5/8 inches, and a close length of 18 inches, as shown in Figure 3.5 below. It guarantees the monitoring system's stability and alignment, enabling accurate positioning and trustworthy data collection.

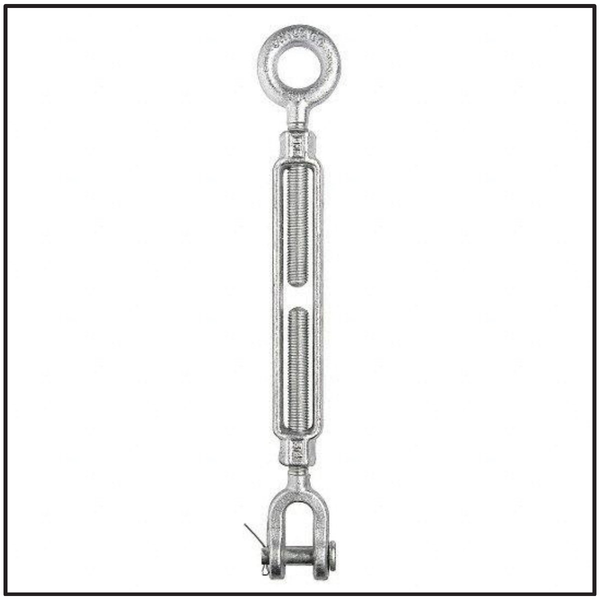

Figure 3.5 Turnbuckle Jaw and Eye
Galvanized 5/8 X 18 inches

Nails are used in the monitoring system to fasten wires, brackets, and other fixtures to mounting surfaces. They facilitate the installation and assembly of the monitoring system components by offering a straightforward and efficient method of attachment. The nail used for this prototype is made of steel with a bright finish. It has a length of 9 inches, a head diameter of 10 inches, and a 13 inches gauge. This nail also has a smooth round shank as shown in Figure 3.6 below.

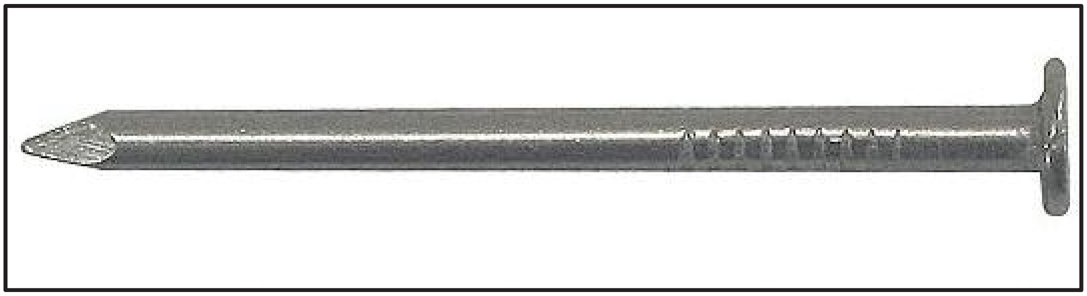

Figure 3.6 Nail Common Bright Finish Smooth Shank Round 9 X 10 X 13 in
Gauge Steel

The monitoring system uses cable clamps to secure the cables to the mounting frames. They usually consist of a screw or bolt that tightens the clamp, which holds the cable firmly, and a metal or plastic clamp that wraps around the cable. They guarantee a neat and orderly cable arrangement and improve the system's overall reliability by preventing the movement or vibration of the cables that could occur during harsh weather conditions when they are in use. The cable clamps used for this experiment are 1/8 inches in size, and have a nylon material, as shown in Figure 3.7 below.

Figure 3.7 Cable clamp Nylon 1/8 inch

The winch cable is used in the prototype to raise or lower the LiDAR scanner or other components so that they can be adjusted in height during deployment or setup. It makes it possible to precisely place the scanning instrument at varied altitudes, which makes it easier to capture the best possible data from various angles. The winch cable comes with a zinc-plated hook, safety clasp, swaged loop, and heavy-duty thimble eye, and is suitable for both manual and electric winches, as shown in Figure 3.8 below. Its size is 3/16 inches, and has a length of 50 feet, and a working load limit of 840 pounds.

Figure 3.8 Winch Cable 3/16 in 50 ft 840 lb

The cylindrical stainless steel welded tube acts as a structural support for the LiDAR scanner, battery, and Raspberry Pi clock, ensuring that they are mounted safely. It offers the monitoring system a strong and long-lasting framework that guarantees stability and resilience to outside influences. For this prototype, the tube had an outside diameter of 1.25 inches, and an overall length of 6 feet as shown in Figure 3.9 below.

Figure 3.9 Welded Tube 1.25 in 6 ft 316 Stainless Steel

The prototype's cables and wires are shielded from damage by red silicone tubing, which is exceptionally durable and temperature resistant. By protecting the cables from outside factors like moisture, dust, and abrasion, it increases their longevity and lowers the possibility that they will be damaged during use. To prevent interfering with other work that needs to be done there, it is also utilized to demonstrate through its vivid color that a monitoring system is there at that particular site. This will be demonstrated in detail using the entire assembly in Section 3.3.

3.3 Montage and Assembly

To construct a working monitoring system, all of the parts listed in Section 3.2 were assembled and integrated throughout the prototype's montage. This is a thorough breakdown of the montage procedure:

First, the tripod for the monitoring system was chosen as a suitable mounting structure as part of the mounting structure preparation. It was made sure the framework was sturdy and could withstand the weight of the parts. The tripod is then fastened to the stainless steel welded tube using anchor bolts and nails. The tubing is set up vertically to function as the LiDAR scanner's primary support structure. At the top of the 6-foot stainless steel tubing, a cable clamp was attached. The monitoring system's cables will be fastened with this cable clamp to keep them from tangling or coming free in operation. The stainless steel tubing is where the LiDAR scanner is mounted. A lab assistant created a mounting bracket that was mounted on the tube to hold the LiDAR scanner firmly in place, guaranteeing that it was positioned precisely for maximum efficiency and preventing any movement. After that, the monitoring system's winch cables were routed along the stainless steel tubing and fastened in place with cable clamps. There are no sharp edges or obstacles that could cut the cables, and they are arranged neatly at an angle. In addition to protecting the wires from environmental elements including dust and wind, the red silicone tubing was wrapped around the cables to visibly display the full prototype assembly. The high-visibility orange tape was also placed along the winch cable for visibility.

The Raspberry Pi clock and battery are positioned carefully during the installation of the prototype monitoring system to provide maximum accessibility and performance. The tripod's base is where the 12 V/18 A-hr battery is located. It is kept safe from damage and movement while in use by being enclosed in a yellow Pelican case. Placing the battery at the base of the monitoring system lowers its center of gravity and improves stability, particularly on windy or uneven terrain. To facilitate maintenance and replacement when needed, the battery was also positioned close to the bottom of the assembly. The Raspberry Pi clock module is part of the electronic configuration of the surveillance system. A little circuit board that has the Raspberry Pi clock module installed on it is also kept inside the yellow Pelican cover. To ensure effective communication and synchronization of timekeeping data, which is necessary for precise timestamping of monitoring data gathered by the system, the Raspberry Pi clock module is placed close to the batteries.

These procedures can be used to successfully build the prototype monitoring system, producing a sturdy and dependable system for geohazard monitoring applications. Every part is essential to maintaining the system's durability, functionality, and stability while it is in use. The result of the assembly complete with all components is shown in Figure 3.10 below.

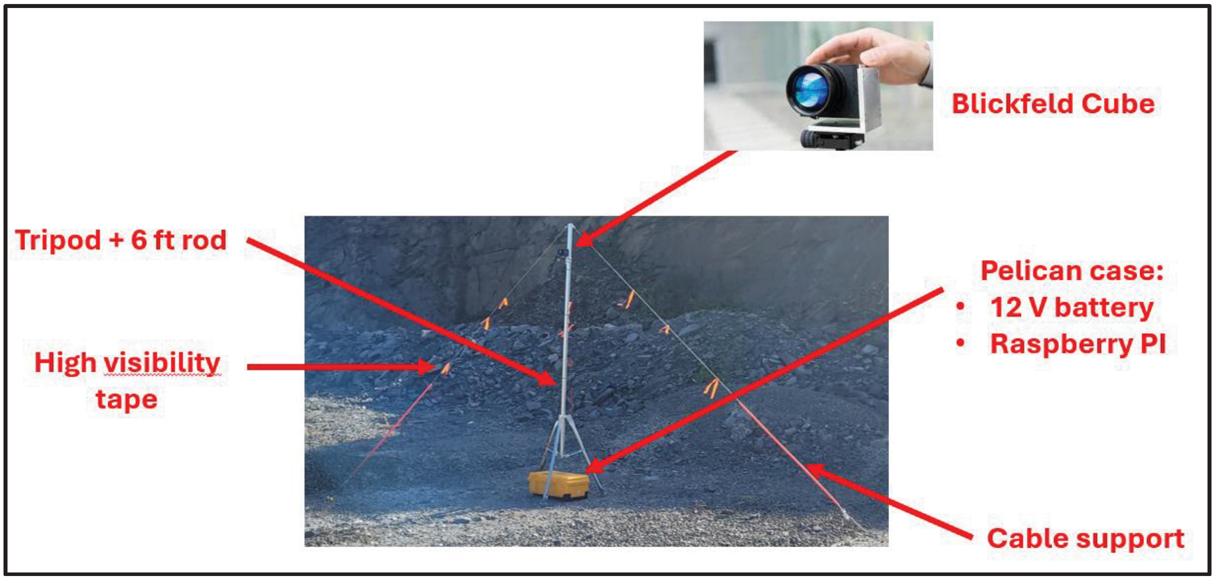

Figure 3.10 Prototype System

3.4 Blickfeld scanner interface and resolution specifications

The imaging device used in this study is the Blickfeld Cube 1 Outdoor LiDAR scanner. With its modern features and specifications for high-resolution 3D scanning, it is made for outdoor use.

Generally, the Blickfeld Cube 1 Outdoor LiDAR scanner uses an Ethernet connection to communicate with other devices. This makes it possible for the scanner and a host computer or control system to communicate and transfer data quickly. Since the scanner is powered by a conventional DC power supply interface, it can be easily integrated into power distribution systems that are already in place. The manufacturer specifies the power requirements, which normally fall between 12 and 24 V DC. Either standard communication protocols like TCP/IP (Transmission Control Protocol/Internet Protocol) or Blickfeld's proprietary software can be used to control and configure the scanner. This enables remote data downloads, performance monitoring, and scanning parameter adjustments.

High spatial resolution is possible with the Blickfeld Cube 1 Outdoor LiDAR scanner, which can often achieve point cloud densities of up to millions of points per square meter. In outdoor contexts, this resolution makes detailed 3D mapping and object identification possible. Both the horizontal and vertical scanning planes' angular resolution requirements are provided by the scanner. These standards allow for accurate mapping of object surfaces and features by indicating the lowest angular increment between individual measurement locations. The ability of the scanner to discern between objects at various distances from the sensor is referred to as range resolution. At long ranges, the Blickfeld Cube 1 Outdoor LiDAR scanner often achieves sub-centimeter accuracy because of its precise range resolution. The high temporal resolution provided by the scanner enables quick data collection and in-the-moment scene monitoring. Applications including high temporal precision environmental sensing, traffic monitoring, and moving object detection are made possible by this. The scanner's dynamic range shows how well it can pick up signals with a variety of intensities. This makes it possible to measure objects with different reflectivity accurately, ranging from highly reflective materials to dark surfaces. The scanner's accuracy and precision standards also show that it can measure angles and distances precisely and consistently. Applications needing accurate dimensions analysis and spatial measurements must adhere to these criteria.

The Blickfeld Cube 1 Outdoor provides a broad FoV with an average field of view of up to 90 degrees horizontally and 30 degrees vertically. This wide perspective allows for thorough coverage of the surroundings, which makes precise 3D mapping and object detection possible. Long-range data collection is possible with the LiDAR scanner; normally, it can capture data at least 250 m away. With this increased range, objects at different distances from the sensor can be accurately detected and measured.

The laser sources used by the Blickfeld Cube 1 Outdoor LiDAR scanner are solid-state, MEMS-based. These lasers function consistently in outdoor settings because of their excellent durability and dependability. The near-infrared (NIR) light emitted by the lasers has a beam divergence of 0.4 degrees and a wavelength of approximately 905 nanometers (nm). Because it performs best outdoors and has good penetration through air conditions, this wavelength is particularly suited for LiDAR applications.

The ruggedized enclosure housing of the scanner, as shown in Figure 3.11 below, is made to survive severe weather conditions. It is resilient to dust, water, and other impurities thanks to its IP67-rated ingress protection. The scanner has flanges or mounting brackets that enable flexible placement on a range of surfaces, including walls, poles, and automobiles. Its adaptability makes it simple to integrate into a variety of applications. A low-voltage DC power supply, usually between 12 and 24 V, powers the scanner. Compatibility with common standard power sources prevalent in outdoor settings is made possible by this.

Figure 3.11 Blickfeld Cube 1 Outdoor LiDAR scanner
Taken from Blickfeld (2022)

With scan rates that often range from hundreds of thousands to millions of points per second, the Blickfeld Cube 1 Outdoor provides high scan rates. For outdoor applications, this quick data gathering allows for dynamic scene analysis and real-time monitoring. Because of its exterior design, the scanner can function well in a variety of weather situations, such as rain, snow, fog, and extremely high or low temperatures. Its sealed enclosure and sturdy design guarantee dependable operation even under harsh outside conditions.

A high-density point cloud with up to 250,000 points per second is produced by the Blickfeld Cube 1 LiDAR. With only one scan frame, this high data rate is able to acquire comprehensive environmental information. The configured scan rate and the area covered determine the precise number of points for every scan frame, although a high number of points guarantees thorough coverage of the surroundings. The distance from the sensor determines the interval between each individual point in the scan. The Blickfeld Cube 1 has a point spacing of roughly 15 mm between successive spots at a distance of 10 m. This results in great spatial resolution at short and medium distances, or 1.5 cm per 10 m increment. The Cube 1's narrow spacing makes it appropriate for medium-range applications even at extended ranges; its point spacing rises significantly beyond 10 m. The Blickfeld Cube 1's high point density and precise spacing allow it to capture comprehensive information about the surfaces of objects and the terrain, which is essential for applications like infrastructure inspection, geohazard detection, and ice shelf monitoring. The Blickfeld Cube 1's outdoor qualities, notably its resilience to changing weather patterns and high resolution, make it appropriate for long-term installation in difficult settings like Grizzly Creek.

Interface cables for attaching the scanner to external devices, including computers or control systems, could be included in the package. Simple integration and communication with the LiDAR scanner are made possible by these wires. To make installation on different surfaces easier, the scanner has a ¼ inch-UNC threaded hole, as shown in Figure 3.12 below, for mounting the Blickfeld Cube to common camera mounts, such as brackets, flanges, or screws. These add-ons guarantee the scanner is mounted steadily and securely in outdoor settings.

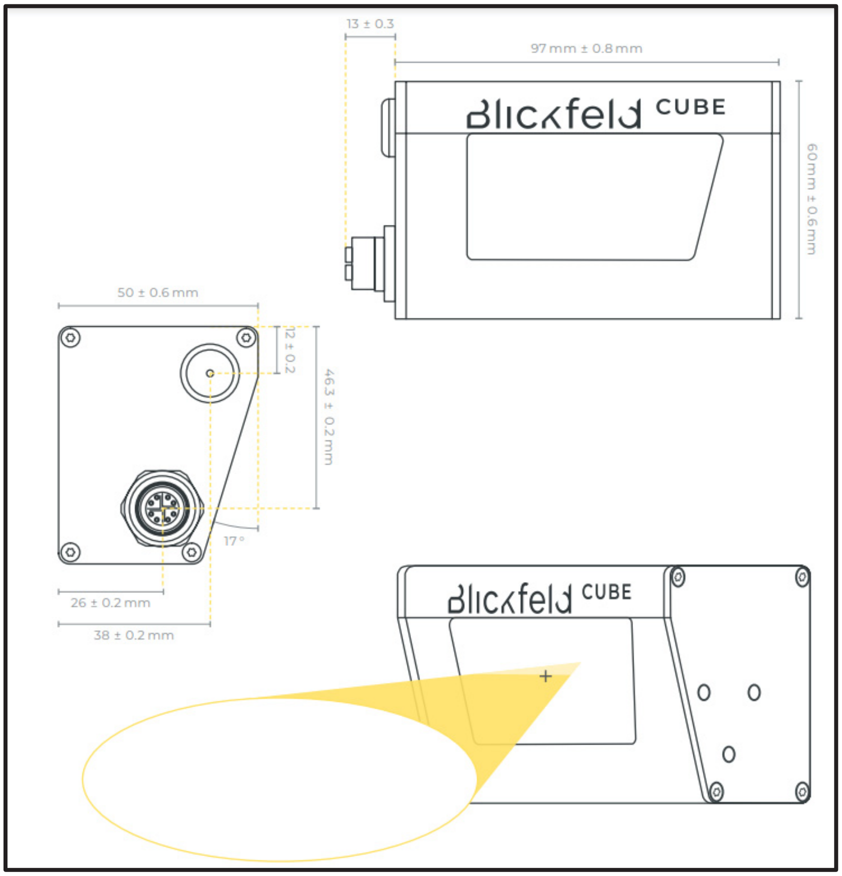

Figure 3.12 Blickfeld Cube 1 Outdoor Dimensions
Taken from Blickfeld (2022)

In entirety, the Blickfeld Cube 1 Outdoor LiDAR scanner provides strong optical, mechanical, and electrical performance appropriate for a variety of outdoor surveillance applications, comprehensive interface and resolution details, and sensing uses. The Blickfeld Cube 1's outdoor qualities, notably its resilience to changing weather patterns and high resolution, make it appropriate for long-term installation in difficult settings like Grizzly Creek. It gives users useful details regarding its features and performance parameters. Its superior build quality, innovative laser technology, and flexible mounting choices make it the perfect alternative for harsh outdoor settings.

CHAPTER 4

COMPUTATIONAL METHODS

4.1 Point Cloud Processing

CloudCompare V2.12.4 (Girardeau-Montaut, 2022) was used as the primary software for point cloud processing. CloudCompare is a free, open-source software developed primarily for geoscientific applications. The tool has since expanded to multiple fields of applications and features a number of computational algorithms for feature recognition, cloud registration, measurements and more.

Using CloudCompare for point cloud registration and processing entails many phases, including quantification of registration accuracy and quality rating of scan placement. CloudCompare has extensive visualization features for 3D point cloud data rendering. Large point cloud datasets may be dynamically navigated, rotated, zoomed in, and panned over, allowing for in-depth examination and analysis. The program lets users select the best representation for their data and analytic needs by supporting several rendering modes, such as surface, mesh, and point rendering. Users can improve the visual clarity and interpretability of their point cloud visualizations by modifying the point size, color mapping, transparency, and shading options available in CloudCompare's display settings. Point cloud data can be imported and exported using a variety of file formats supported by CloudCompare, such as LAS, LAZ, XYZ, PTS, PLY, and others. The smooth integration of data-gathering systems and other software tools is guaranteed by this compatibility. For thorough research and visualization, users can import several point cloud datasets at once and combine them into a single, cohesive dataset. In the same manner, exported datasets are readily shared with partners or combined with other software systems for additional processing.

Using a LiDAR scanner, several point cloud datasets are collected at various periods or from various angles. The resolution, quality, and spatial coverage of these datasets would differ. To begin pre-processing, the raw point cloud datasets are imported into CloudCompare. The data sets are then cleaned and adjusted to obtain a consistent framework towards data analysis. This includes the following steps briefly described below:

- Filtering:

  This procedure entails eliminating information or points that are not pertinent to the topic at hand. By concentrating the analysis on the required region, filtering increases the accuracy and efficiency of processing. Range-based filters, which eliminate points outside of a given distance, and boundary filters, which eliminate points outside of a defined area, are examples of common filtering approaches.

- Smoothing:

  Through the application of smoothing, which involves averaging or interpolating nearby points, noise in the point cloud data is reduced. Excessive smoothing would distort geometry and eliminate small details. Noise reduction may not be achieved by under-smoothing. It facilitates the creation of a more realistic and continuous surface, especially when working with erratic or noisy data. Additionally, by increasing the coherence of the point distribution, smoothing improves the accuracy of later processing stages like meshing, surface reconstruction, and feature extraction.

- Down sampling:

  Down sampling makes the data more manageable without significantly compromising detail by reducing the number of points in the dataset by retaining only a fraction of the original points. Usually, random sampling techniques, which average points inside a three-dimensional grid, are used for this. It helps to expedite processing while preserving the general organization.

- Noise reduction and outlier removal:

  The goal of these stages is to remove outliers, or random, undesirable points that don't match the surface or surroundings being assessed. Statistical outlier removal (SOR) and radius outlier removal (ROR) are two techniques used to exclude data points that don't fit the surrounding data's general distribution. A more accurate depiction of the scanned object or environment is ensured by this phase.

4.2 Scan registration techniques

CloudCompare provides a range of registration techniques, such as feature-based registration algorithms and Iterative Closest Point (ICP). These algorithms minimize the difference between corresponding points to align point cloud datasets.

The degree to which individual point cloud scans are consistently and precisely positioned with one another within a wider spatial context is referred to as the quality of scan placement. Ensuring the exact registration and alignment of many scans is crucial in producing an accurate and comprehensive picture of the scanned environment. A high-resolution scan obtained at time 0 is registered with a low-resolution scan obtained at the same time to evaluate the quality of scan placement. To align the two scans, the registration transformation parameters are calculated. Enough depth of coverage guarantees that the entire region of interest is sufficiently examined from several angles. Imprecise depictions of the environment may result from gaps or areas with insufficient coverage.

The overall quality of the scan placement is influenced by the point density inside each scan. Increased point density improves the accuracy of registration and alignment across scans by offering more precise and detailed representations of surface characteristics and geometry. To visually assess the alignment quality, the registered high-resolution scan is superimposed over the low-resolution scan. The registered point cloud dataset's disparities and inconsistencies are reduced when scan placement is consistent across several scans. Accurate and dependable registration methods are improved by uniform scan location, orientation, and scale; this results in more accurate alignment between scans. As recognized reference locations for registration and alignment, ground control points (GCPs) or reference markers positioned inside the scanned area can be used. The precision and dependability of scan placement are increased by integrating control points into the scanning process, especially in georeferenced applications.

Accurate scan placement depends on the LiDAR scanner and related sensors being calibrated properly. By minimizing mistakes and distortions in the registered point cloud collection, calibration guarantees that measurements are accurate and consistent across scans. Tools such as overlay and transparency, color mapping and intensity visualization, cross-section and profile views, interactive slicing and clipping, distance measurement, and change detection are offered by CloudCompare for comparing and visualizing numerous point cloud datasets in three dimensions.

CloudCompare calculates the cloud-to-cloud distance between corresponding points in the registered datasets to measure the precision of registration. This distance measures registration inaccuracy by indicating the positional difference between aligned locations. One may evaluate the average registration accuracy and its variability across the dataset by computing the mean and standard deviation of the cloud-to-cloud distance. A cloud-to-cloud distance that is almost 0 indicates that the registered point clouds are perfectly aligned. Any departure from zero suggests inconsistencies in the datasets or problems with registration. Quantitative measures for assessing the quality of registration are provided by the cloud-to-cloud distance's estimated mean and standard deviation. Accurate and reliable registration is indicated by a small mean distance and a low standard deviation. Large variances in the cloud-to-cloud distance or any outliers could be signs of inadequate registration or dataset inconsistencies. These areas can be looked into more thoroughly and fixed if needed. Through visual examination of the registered point cloud collection, users can also determine and assess any gaps, misalignments, or artifacts that may arise from improper placement of the scans. Together with quantitative evaluations, visual inspection contributes to ensuring the overall integrity and quality of the registered dataset.

With the use of integrated measuring tools, statistical analysis, and visualization approaches, CloudCompare enables complex evaluation and quantification of point cloud data. From the point cloud data, users can immediately measure lengths, angles, areas, volumes, and other geometric features. To examine data distributions, trends, and patterns, users can produce statistical summaries, scatter plots, and histograms. Users can also examine registration errors, see registered point clouds, and create insightful reports and visualizations. This makes it easier to communicate registration findings and offers information for additional study or action.

These procedures enable precise alignment of different datasets and assessment of registration quality using point cloud registration and processing using CloudCompare. Its flexibility, robust processing techniques, and user-friendly interface are crucial for a variety of applications, including 3D mapping, surveying, and monitoring.

4.2.1 The ICP algorithm

A popular technique for aligning two sets of point clouds by minimising their difference is the Iterative Closest Point (ICP) algorithm. It is especially useful in fields like geoengineering, robotics, and 3D modelling where precise scan registration is required. The alignment of the source point cloud with the target point cloud is accomplished by the iterative refinement of the transformation (rotation and translation) required by the ICP algorithm (Aubertin, 2024).

The procedure starts with a preliminary approximation of the relative positions of the source and target point clouds. Although this estimate may be imprecise, it provides a foundation for the alignment. Every iteration finds the nearest point in the target point cloud for each point in the source point cloud. We treat these pairs as points that correspond. The algorithm determines a transformation (rotation and translation) that minimises the distance between the respective points based on the matched point pairs. The source cloud becomes closer to the target thanks to this transformation. Iteratively, the process is repeated. The correspondences are reassessed, and a fresh transformation is calculated following each transformation. This keeps going until either the maximum number of iterations is reached or the difference between iterations is less than a predetermined threshold. When the transformation changes between iterations are insignificant, the method converges, meaning that the source point cloud and the target point cloud are adequately aligned.

The sensitivity to the first guess presents a challenge in ICP. The procedure may converge to a local minimum and produce inaccurate alignment if the initial alignment is too off. Additionally, noise or outliers in the point clouds might cause distortions in the correspondence matching, making ICP less effective.

The ICP algorithm is essential for geoengineering because it aligns 3D images from LiDAR or photogrammetry to track the movement of structures such as piles, tunnels, and bridges over time. Precise tracking of structural alterations, including deformations or fissures, is made possible by accurate registration.

The seminal work that introduced the ICP algorithm was a 1992 study by Besl and McKay. The technique presented in the research involves iteratively minimising the distance between corresponding points in the two datasets in order to align two 3D forms, often known as point clouds. In computer vision, 3D modelling, and robotics, this registration method became a fundamental algorithm for applications like object identification, form matching, and SLAM (Simultaneous Localisation and Mapping). In order to align the two datasets, the ICP algorithm in this work matches each point in one point cloud to the point that is closest to it in the other point cloud. It then estimates the necessary transformation (rotation and translation), iteratively improves this transformation until convergence. The sum of squared disparities between the respective points is minimised by the algorithm. The foundation of the original ICP approach is this fundamental concept of point-to-point minimisation. ICP may be used for both rigid and non-rigid objects, and it can be applied to a variety of tasks such as autonomous navigation (localising a robot in a 3D environment) and medical imaging (aligning 3D scans of the human body). This work is significant because it established the foundation for further developments in 3D form registration and created a new area of study devoted to enhancing the algorithm's robustness, accuracy, and speed.

The shortcomings of the original ICP algorithm put forth by Besl and McKay are discussed in the study by Rusinkiewicz and Levoy (2001), notably with regard to computing efficiency and resilience. In order to make ICP faster and more useful for real-time 3D form registration, the authors Rusinkiewicz and Levoy suggest a number of enhancements and optimisations. Finding the closest point between two point clouds, which can take some time, is one of the main bottlenecks in the original ICP. The authors present techniques to speed up the nearest-neighbor search and drastically cut down on the time needed for each iteration, such as employing bounding volume hierarchies or kd-trees. This work addresses methods to minimise point-to-plane distances, which is computationally more efficient, especially for objects with smooth surfaces, as opposed to minimising point-to-point distances (as in the original ICP). They investigate techniques for speedier convergence as well as methods for improving the algorithm's initialisation, which lowers the risk of the algorithm entering a local minimum. In this study, several ICP variations optimised for various conditions and applications—such as noisy data or situations where only partial surfaces are available—are shown. A lot of 3D applications that require quick and precise registration have embraced the work of Rusinkiewicz and Levoy. Their improvements enabled ICP to be used for real-time applications like as 3D object reconstruction, augmented reality, and robotic navigation.

4.2.2 Recursive ICP

Recursive ICP (R-ICP) provides a consistent registration framework to reduce placement errors and rapidly quantify the resulting uncertainty. The R-ICP method was presented in Aubertin (2024). The procedure is briefly summarized below:

1. Scan import and initial rough placement. Two scans are imported and roughly placed together through manual translations and rotations to generate the original baseline.
2. ICP placement is applied to one of the scans with respect to the reference scan.
3. Cloud-to-cloud (C2C) distance computations are carried. High C2C distances will reflect overlap occlusion or mutually exclusive sub-zones of the scans.
4. Computation of Registration error Reg. For 95% confidence interval, Reg is computed as the average $C2C$ + 2 times the standard deviation. Strong asymmetry of the C2C distribution relates to important occlusions and mutually exclusive sub-zones of the two scans. These zones are filtered using the computed Reg as the filter threshold. Alternatively, if the distribution skew is very severe, the filter threshold can be measured explicitly as the maximum C2C distance below 95% cumulative frequency.
5. Scan filtering. The scans are filtered using C2C$< 95\%$ cumulative distribution.
6. Repeat steps 2-5. The computed Reg will progressively decrease until an asymptote value is reached. Further filtering iterations will then reduce the overall scan density and increase registration error Reg.

4.3 Automation Method through Python code

Using techniques and processes to effectively align various point cloud datasets and calculate registration quality indicators like maximum, minimum, and average cloud-to-cloud distances, and standard deviations are all part of automating point cloud registration and processing through the Python code.

With the library open3d, the Python code first imports point cloud data from the files and data sources obtained from the LiDAR scanners. To manage the point cloud data further, this step entails reading and converting it into Python-compatible data structures. Pre-processing operations are conducted to clean and prepare the point cloud data before registration. To maintain data quality and consistency across datasets, this involves down sampling, coordinate normalization, noise removal, and outlier detection. The Python method then uses a transformation matrix that was manually obtained by CloudCompare between the first high-resolution and low-resolution scans at time 0 to perform a registration procedure, such as ICP and feature-based registration, to align multiple point cloud datasets. To reduce the difference between corresponding points in the datasets, the method iteratively optimizes the transformation parameters using translation, rotation, and scale methods.

Following registration, the code calculates the cloud-to-cloud distances between each pair of corresponding points in the registered datasets and stores the distances in an array through comma-separated values (CSV) in Excel files. The algorithm evaluates the accuracy and dependability of the registration process by computing many registration quality measures, such as the maximum, minimum, average, and standard deviations of cloud-to-cloud distances. The worst-case alignment error is indicated by the maximum distance, which shows the highest spatial difference between the point clouds in the registered datasets. The best-case alignment accuracy is indicated by the minimum distance, which is the least spatial disagreement between the point clouds. The average distance serves as an indicator of overall registration precision since it is the average geographical variation over all point cloud datasets. The discrepancy of cloud-to-cloud distances around the mean value is quantified by the standard deviation, which shows the consistency and homogeneity of registration errors throughout the dataset. All the quality measures are calculated for each time slot that the LiDAR records the point cloud datasheets. Lastly, the maximum, minimum, and average cloud-to-cloud distances and standard deviation from each time are averaged and outputted to one file to analyze the complete results.

Users may ensure precise and dependable alignment of several point cloud datasets for different applications, expedite the alignment process, and analyze registration quality metrics methodically by automating point cloud registration and processing through Python.

4.4 Uncertainty and level of detection

The term level of detection (LoD) describes the smallest change or signal that can be consistently identified in a measurement system such as the Blickfeld Cube 1 Outdoor LiDAR scanner from fluctuation or background noise. LoD is critical for evaluating the sensitivity and dependability of monitoring systems, particularly in scenarios like geohazard monitoring with LiDAR scanners where it is imperative to identify even minute changes or anomalies. The LoD assesses how well the monitoring system performs in identifying minute alterations or irregularities in the scanned environment. The minimal detectable change or signal that the system can consistently identify from variability or background noise can be found by computing the LoD.

The LoD aids in calculating the measurement uncertainty related to the monitoring procedure and the LiDAR scanner. It considers many error factors, such as noise, surface roughness, registration errors, uncertainties in positioning, and flaws in sensor calibration. Knowing the LoD makes it possible to evaluate the measuring system's dependability and constraints.

Understanding the LoD makes it possible to enhance the sensitivity and detection capabilities of the system by optimizing data acquisition parameters including measure repetition, scan resolution, and scanning method.

To make decisions and act in response to changes or abnormalities seen in the environment under observation, the LoD assists in defining thresholds or criteria. Researchers can ascertain whether detected changes are significant enough to justify additional research or action by comparing measured signals to the LoD.

Comprehending the LoD offers a framework for analyzing and evaluating the importance of monitoring outcomes concerning the system's capabilities. By using the LoD as a benchmark, the strength and consistency of observed changes can be assessed and significant signals and variability or background noise can be differentiated. Several variables and formulae are used in the LoD calculation.

Uncertainty and error components associated with LiDAR measurements arise from:

- Tool calibration (i.e. ability to repeat a measurement) σ_{tool} (mm)
- Beam footprint error σ_{BF} (mm)
- Registration error Reg (mm)

Error and uncertainty are measured with respect to a confidence interval CI (%) assuming perfectly random error distribution. In some situations, the error distribution is not random, this simplification becomes conservative and therefore appropriate.

The error associated with a given measurement along a reference frame E_{CI} for confidence interval CI can be computed as:

$$E_{CI} = \pm[F(CI) \cdot (\sigma_{tool} + \sigma_{BF}) + reg_{CI}] \tag{4.1}$$

where $F(CI)$ is a confidence interval factor to match the random distribution (i.e. $F(CI) = 1.96$ for $CI = 95\%$). The registration error reg_{CI} is computed through the R-ICP method outlined previously. The equation for reg_{ci} is given as:

$$reg_{CI} = \mu_{C2C} + F(CI) \cdot RMSD_{C2C} \tag{4.2}$$

where μ_{C2C} is the average for the C2C distribution between the two registered scans, and $RMSD_{C2C}$ is the root mean square deviation (i.e. the standard deviation) for the C2C distribution. $RMSD_{C2C}$ is referenced instead of standard deviation despite the computational similarity given that the C2C distribution may not be perfectly symmetrical.

The beam footprint error σ_{BF} is computed using the beam divergence of the scanner, the distance between the scanner and the targeted point cloud, and the target's surface roughness.

The tool error σ_{tool} is typically measured as the standard deviation for the repetitive measurement of a given distance and is provided by the manufacturer as part of the calibration process.

The level of detection LOD_{CI} for a confidence interval CI between two scans A and B can be computed as:

$$LOD_{CI} = \max\left(E_{CI,A}, E_{CI,B}\right) + reg_{CI,AB} \tag{4.3}$$

The above equation for LOD is valid for change detection purposes between two point cloud data sets. The error component is therefore dominated by the registration error reg, in turn dominated by scan density. This notion drives the rationale for generating an initial high resolution reference scan at the start of a high temporal frequency monitoring program. This approach is further discussed in later sections. It is further noted that LOD could be noticeably reduced through the use of mesh to cloud distance measurements, at the cost of computational time and increased influence of scan roughness. These notions are further discussed at length in work published by Lague et al. (2013) and Fey and Wichmann (2017).

Beam footprint error σ_{BF} is computed as follows (Aubertin, 2024). Assuming the X-Y plane is parallel to the flat elliptical beam footprint, the largest axis of the ellipse, a_{el} (m), is computed as:

$$a_{el} = |I_B| \cdot \cos(\theta_I) \cdot \left[\tan\left(\theta_\mathrm{I} + \frac{\beta}{2}\right) - \tan\left(\theta_\mathrm{I} - \frac{\beta}{2}\right)\right] \tag{4.4}$$

where θ_I (degrees) is beam incidence angle with respect to the surface.

The incidence angle θ_I is computed as:

$$\theta_I = \cos^{-1}\left(\vec{n} \cdot \overrightarrow{I_B}\right) \tag{4.5}$$

where $\vec{n}$ is the normal vector of the plane spanning the ellipse.

Beam distortion error is computed as:

$$\sigma_{BF} = \sqrt{(\sigma_{xy}^2 + \sigma_z^2)} \tag{4.6}$$

where σ_{xy} and σ_z are the standard deviation of possible reflective position of the beam along the distorted footprint for the in plane and out of plane component of the ellipse respectively.

Considering perfect random distribution of the positional error for the reflected pulse, the largest span of the ellipse a_{el} covers the full spectrum of the plausible position on the X-Y plane. The corresponding standard deviation would therefore equate to:

$$\sigma_{xy} = a_{el}/6 \tag{4.7}$$

The Z component of the error distribution corresponds to the difference between plausible extents, i.e. Z_1 and Z_2. This one-sided error in the random distribution curve corresponds to:

$$\sigma_z = \frac{1}{3}(Z_1 - Z_2) \tag{4.8}$$

where $Z_1 > Z_2$.

The components Z_1 and Z_2 can be computed as:

$$Z_{1,2} = \frac{|I_B|\cos(\theta_{\mathrm{I}})}{\cos\left(\theta_I \pm \frac{\beta}{2}\right)} \tag{4.9}$$

In this research work, change detection analysis was conducted on topographical data sets surveyed using a Blickfeld Cube 1 LiDAR with a divergence angle $\beta = 0.4°$. The beam divergence error σ_{BF} with respect to measurement distance I_B (m) and incidence angle θ_{I} for the Blickfeld Cube 1 is plotted in Figure 4.1. Most survey measurements typically avoid incidence angle above 60 degrees. The maximum error associated with beam divergence can therefore be estimated from the error curve generated with respect to distance for incidence angle $\theta_I = 60°$ as plotted in Figure 4.2.

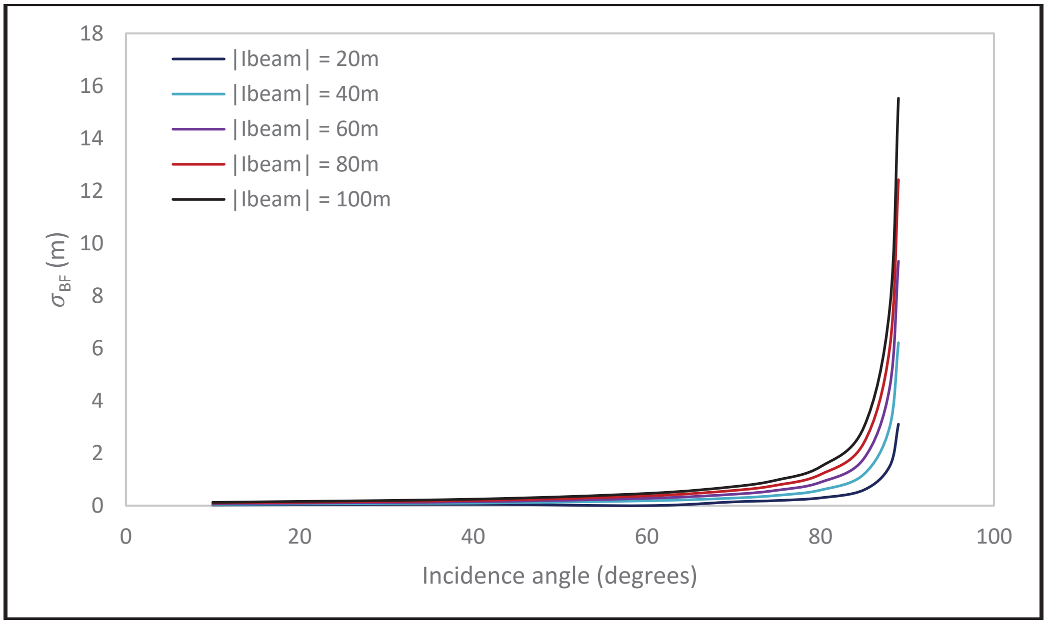

Figure 4.1 Beam footprint error for the Blickfeld Cube 1

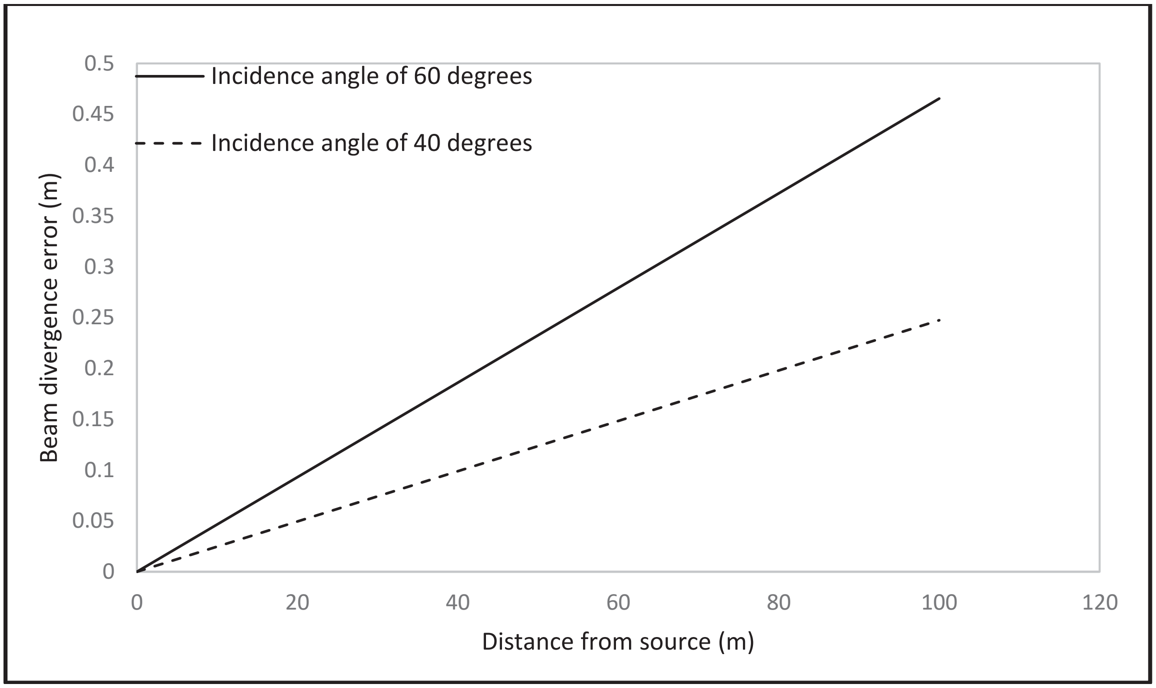

Figure 4.2 Beam footprint error for the Blickfeld Cube 1 for incidence angle of 40 and 60 degrees

CHAPTER 5

CONTROLLED PILE FAILURE HIGH TEMPORAL FREQUENCY MONITORING EXPERIMENT

5.1 Scope and Objectives

The work presented in this chapter aimed to trial the experimental set up of Chapter 3 in a controlled setting. The study involved a controlled experiment that generated the failure of a pile of fine granular material stored near a limestone quarry. In this experiment, failure is mechanically induced to simulate natural geohazard occurrences such as rockfalls and landslides. Designing and conducting the experimental setup for causing controlled pile failure are included in the scope. This includes choosing appropriate pile materials, figuring out the pile's size and shape, and setting up procedures for mechanically causing failure with a front-end loader, amongst other things. Topographical monitoring of the pile during the event aimed at capturing movements associated with the artificially generated landslide.

The scope includes using innovative analytical techniques to interpret the information gathered from the experiment. This entails evaluating the dynamics of failure development, assessing changes in geometry and surface properties, and processing point cloud data to recreate 3D models of the pile. The purpose of this chapter is to assess how well the monitoring system prototype performed in recording and capturing the controlled pile failure experiment. This entails evaluating the system's capacity to quickly identify, track, and evaluate dynamic geohazard events. The goal is to understand the physics and behavior of rock heaps under induced failure conditions by evaluating the experimental results against theoretical models or empirical observations. This entails evaluating the accuracy and dependability of the monitoring system as well as interpreting the data to pinpoint important variables driving failure processes.

5.2 Experimental Settings

To ensure that the results of experiments are valid and relevant, it is essential to choose appropriate locations for geohazard simulations. These locations should include topography features and geological traits typical of geohazard-prone areas found in the actual world. Researchers can precisely mimic the environmental circumstances of natural geohazards by selecting suitable sites, which enables controlled experimentation and observation of failure mechanisms. Additionally, conducting studies in appropriate locations improves the validity and relevance of study findings, facilitating the creation of efficient monitoring and mitigation plans for geohazard-prone regions.

The trial site, the Sintra limestone quarry in St-Alphonse-de-Granby, Quebec, was selected for the controlled pile failure monitoring experiment because it can effectively simulate geohazard events including landslides and rockfalls. The location has favorable geological conditions for the controlled pile failure monitoring experiment. The rock pile can be easily constructed with plentiful reserves of broken rock sorted in different piles found in the quarry. Because of its durability and abundance in geological formations, limestone is an excellent platform for landslide and rockfall simulations.

The test was conducted with a pile of granular material of size 0-5 mm already present onsite. A picture of the pile is presented in Figure 5.1. The material had been exposed to outside elements and weather for several months. The pile was therefore slightly damp. This humidity was advantageous in the course of the experiment, as it exhibits apparent cohesion when the pile was remodelled as part of the experiment.

Figure 5.1 Limestone Pile at Sintra Quarry of Fine and Wet Granular Material

A Front-End-Loader (FEL) was used onsite to remodel the pile. The lower portion of the pile was excavated to achieve a near vertical slope. This condition was made possible by the apparent cohesion of the material. As the material dried up with the sun, the material would progressively slide down and form a new geometry. This artificial landslide was the basis of monitoring for this experiment.

Figure 5.2 shows the section of the pile excavated with the FEL on the right.

Figure 5.2 Excavation Pile (on the left) and FEL (on the right)

High temporal frequency (HTF) monitoring was carried using the Blickfeld cube sensor as outlined in Chapter 3. A high resolution survey using a drone with photogrammetry capabilities was performed at the onset of the experiment. This high resolution scan represented the reference data set for change detection analysis. Considering the equations presented in

Chapter 4 for the computation of LOD thresholds, the use of a high resolution scan as the reference data set diminishes considerably half of the error components, and thus reduces the overall achieved uncertainty.
Figure 5.4 shows the topographical data set with a color scale for the elevation in the z-direction.

Figure 5.3 shows the layout of the experimental set up. The HTF monitoring system was positioned approximately 45 m away from the pile, with an incidence nearly perpendicular from the excavated slope.

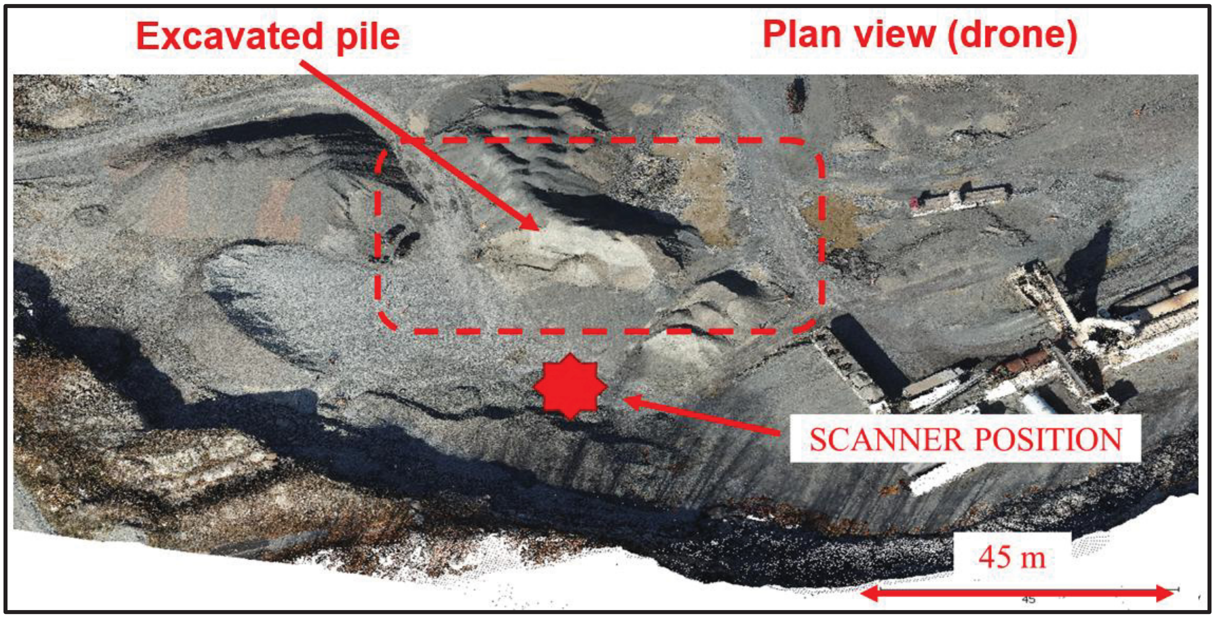

Figure 5.3 Plan View of Sintra Quarry

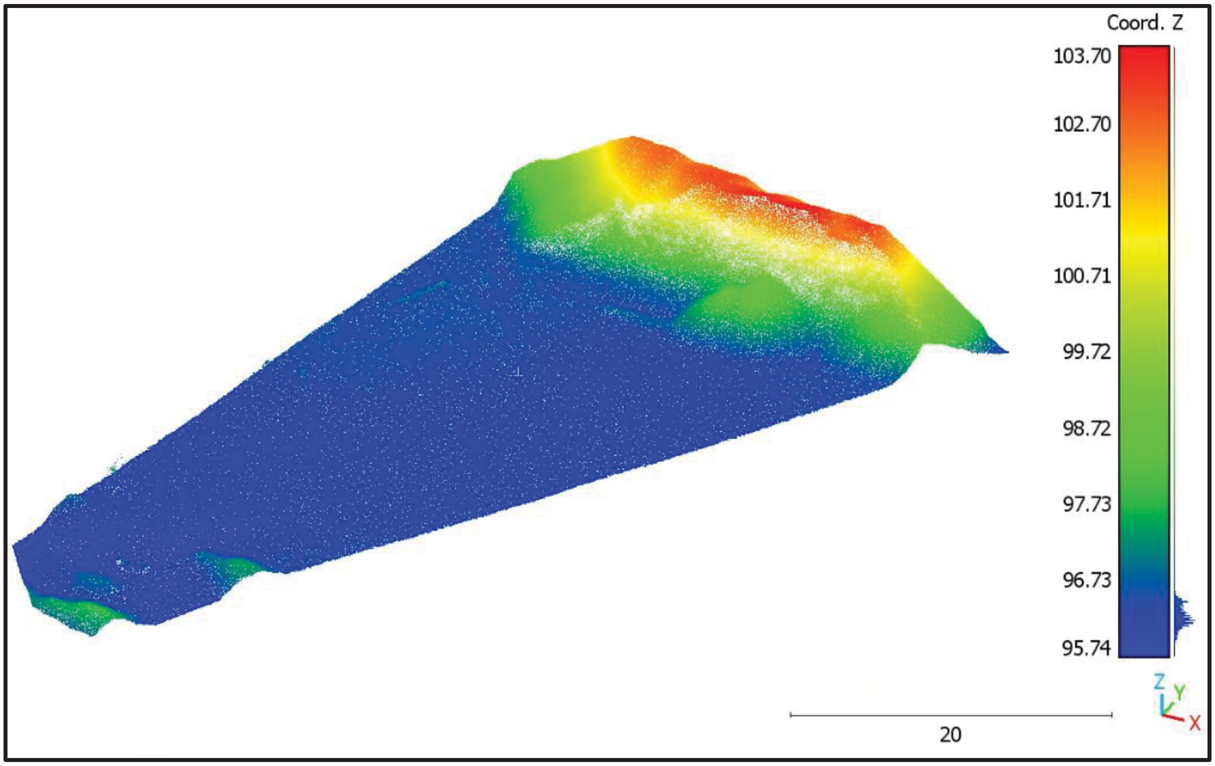

Figure 5.4 Topographical Plan View with Color Elevation of Sintra Quarry

A sub-set of the high resolution scan shown in the previous figure was extracted to use as a reference data set for cloud to cloud distance measurements. This sub-set is shown in Figure 5.5 below.

Figure 5.5 High-Resolution Scan of Limestone Rock Pile

Changes were tracked in the appearance and behavior of the rock pile in real-time as long as the LiDAR scanner was used to continuously gather point cloud data of the pile (2 triggers for every hour of measurements clocked by the Raspberry Pi Clock). The battery was positioned at the bottom of the prototype and maintained by opening and closing the system for each data collection to keep the LiDAR scanner and the Raspberry Pi running for the duration of the experiment, which lasted for one week. This data offers important insights into the rock pile's displacement, deformation, and fragmentation during the collapse process.

Post-experiment analysis is conducted to determine the degree of damage and deformation sustained by the rock pile following the failure event. The LiDAR scanner's high-resolution point cloud data is compared to measure volume, shape, and stability changes. The gathered data is processed and examined using a manual and automated desktop computer approach. The manual technique entails registering and processing point clouds with a specialized software tool like CloudCompare. A thorough 3D model and transformation matrix of the rock pile before and after the failure event is produced by combining the high-resolution scans from the drone with the LiDAR data. To determine structural alterations, displacement patterns, and unstable regions inside the rock pile, the integrated point cloud data are analyzed.

The automated way is inspired by the Python code, which optimizes the workflow for data processing and analysis, allowing to extract significant insights accurately and efficiently from the data they have collected. This technique improves reproducibility and quickens the pace of geohazard monitoring research by automating repetitive operations and standardizing analysis procedures. Registering and processing the point cloud data from the drone-based scans and LiDAR scanner is the initial stage. Several datasets are aligned and integrated into a coherent 3D model of the experimental site using this technique. Algorithms to identify and eliminate noise and outliers from the point cloud data are integrated into the automated Python code. This removes inaccurate or superfluous points from the data, improving its quality and dependability. The method makes it easier to automatically retrieve pertinent metrics and parameters from the processed point cloud data. To quantify variations and trends within the dataset, this involves calculating the standard deviations, maximum, minimum, and average change detection values. Because of its iterative structure, the code can be improved and adjusted in response to user feedback and validation outcomes. The robustness of the analysis is improved, and ongoing progress is ensured by this iterative optimization procedure.

5.3 Initial scan placement

This chapter's change detection analysis procedure is based on the approach outlined in section 4.2.2 and used in Chapter 5. As part of the change detection analysis, a high-resolution scan of reference was chosen from a drone survey conducted in November 2022 using photogrammetry. The entire scan, which was 74.456 MB in size, had approximately 900,000 points. To make the parameters easier to handle for any adjustments, the file was trimmed around the monitoring zone. The cropped data set with surface density is displayed in Figure 5.6. With an approximate equal spacing of 7 cm between points, the average surface density is 618 points per square meter. There were about 340,000 points in that trimmed region.

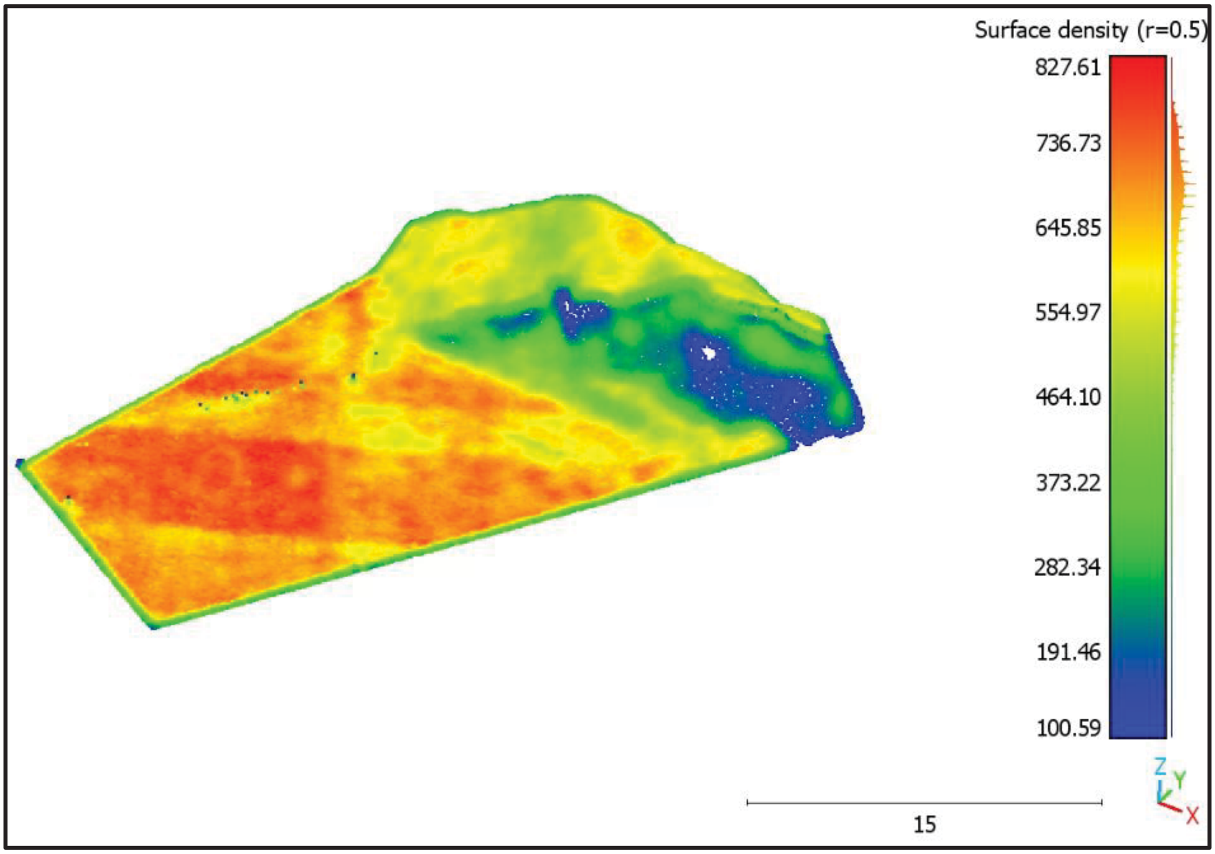

Figure 5.6 Cropped zone from the high resolution topographical data set of reference

The original high resolution data set and each Blickfeld cube scan were compared in order to conduct the change detection analysis used in this work. In order to provide a consistent geographic frame of reference, the first Blickfeld scan was positioned in relation to the high-resolution scan before these calculations were performed. It should be mentioned that moisture in the lens caused problems with some of the early scans' data collection. By switching back to a different, more appropriate lens, this problem was resolved. The earliest date taken into consideration in this work is November 3, 2022. For the purposes of scan placement, this scan was recognized as the first time stamp T0 for high temporal frequency monitoring. The R-ICP method involved 7 iterations to achieve a mean C2C error of 0.049 m, and $reg_{83\%}$of 0.07 m. The computations and experimental work carried next remain valid. Figure 5.7 plots the registration error with respect to R-ICP iterations carried during the scan placement work.

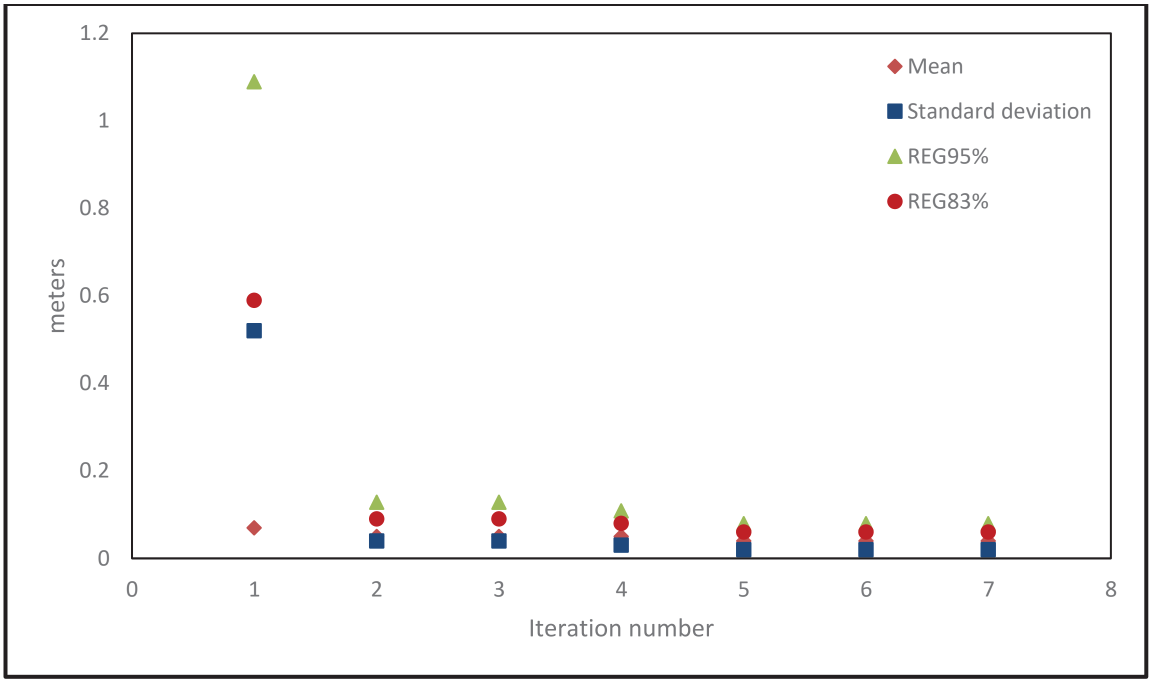

Figure 5.7 Registration error graph for RICP number of iterations

5.4 Results and analysis

The change detection analysis work was carried over a period of 7 days. There is an approximate 5 day gap between the start of reported monitoring data and pile excavation. This gap is due to lens fogging issues after the first night of installation. This situation was also reported during the Yukon case study presented in Chapter 6. This condition was reported to the Blickfeld OEM. Corrections were implemented by using a different lens on the system.

Data collection involved 2 frame per time intervals. Data collection took place every hour. A portion of the data collected on the third day was not recorded properly. The system was promptly rebooted upon noticing the issue which was not further reported afterwards.

Change detection analysis was carried using cloud to cloud distance (C2C) computations from the CloudCompare software. Change detection analysis was carried with respect to the high resolution reference scan described previously.

Figure 5.8 presents C2C average and standard deviation measured at each time interval during the monitoring period. The x-axis represents the time zones of each day starting from 12pm on November 3, 2022, till 1am on November 9, 2022. It is noted from Figure 5.8 that the initial C2C distance is fairly high. At around 6 cm, this value is higher than all subsequent variation. It is ascertained that the extent of pile topographical change took place at the onset of the experiment. Nevertheless, the change for that period is captured, albeit with only the first reported point, given that all C2C measurements are with respect to the high-resolution scan taken at the beginning of the experiment.

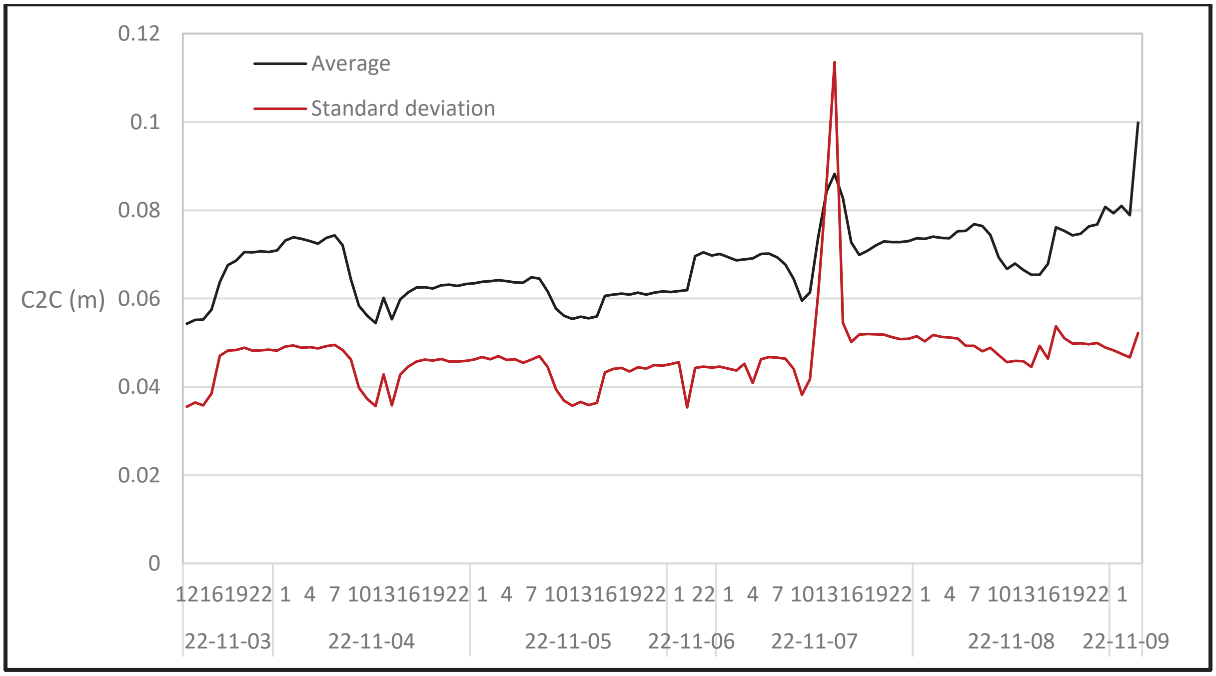

Figure 5.8 Change detection analysis reported in terms of average and standard deviation

Further investigation of the C2C distribution, and implications of statistical figures require additional considerations. Understandably, large sections of the scan present little to no changes while greater changes are observed at the top and bottom of the pile. Moreover, the change in pile geometry may reduce the overall changes as appears to be the case over the period considered.

Considering the relatively good scan placement between the high resolution reference scan, and the first HTF scan, it is ascertained that the bulk of both point clouds are mutually inclusive. This aspect is made particularly important in Chapter 6 where sections of the scans were not mutually inclusive in some of the analysis due to incomplete data acquisition for some time intervals. Consequently, the largest C2C measurements should represent valid deformation values representative of the pile deformation.

Figure 5.11 plots the maximum C2C measurement computed for each time interval. With the exception of the apparent outlier of November 7th, the reported values show near balanced variation over the time considered, which further highlights that geometrical changes considered from an overall statistical framework may misrepresent the situation.

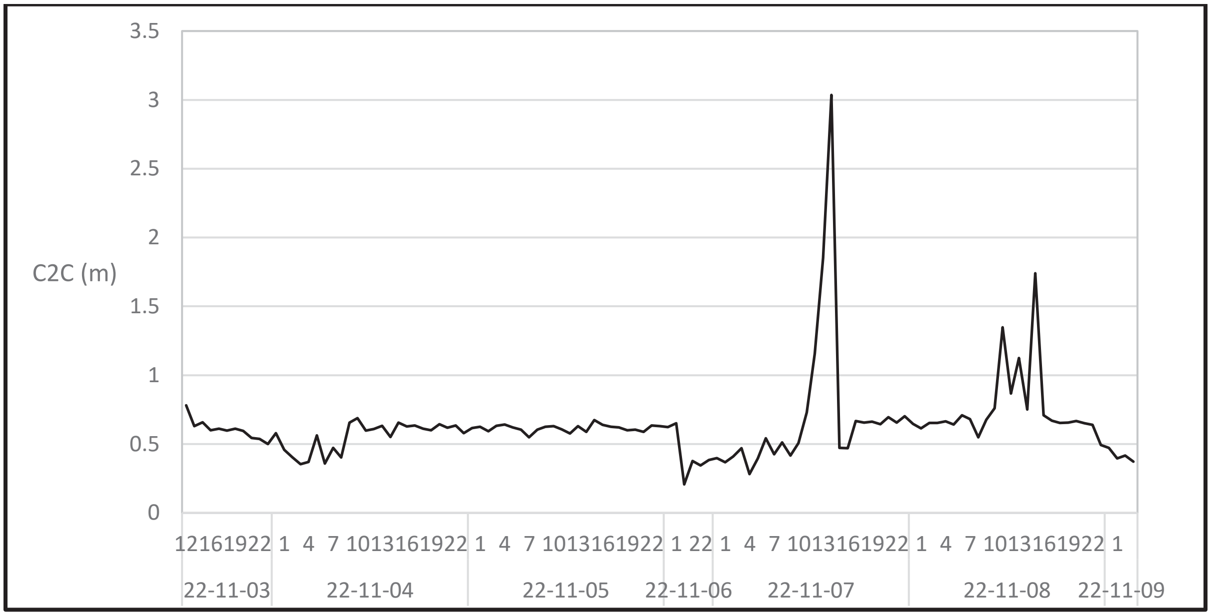

Figure 5.9 Maximum C2C measurement from the cloud distribution

Both previous plots also indicated some apparent variability on a daily basis. This variation within the day was inferred to arise from temperature and/or changes in lighting conditions. Figure 5.10 plots the average C2C measurements while differentiating days and night data sets. With the exception of the incomplete data from November 6th, and the apparent outlier(s) from November 7th, the data appears to exhibit non-negligible daily variability.

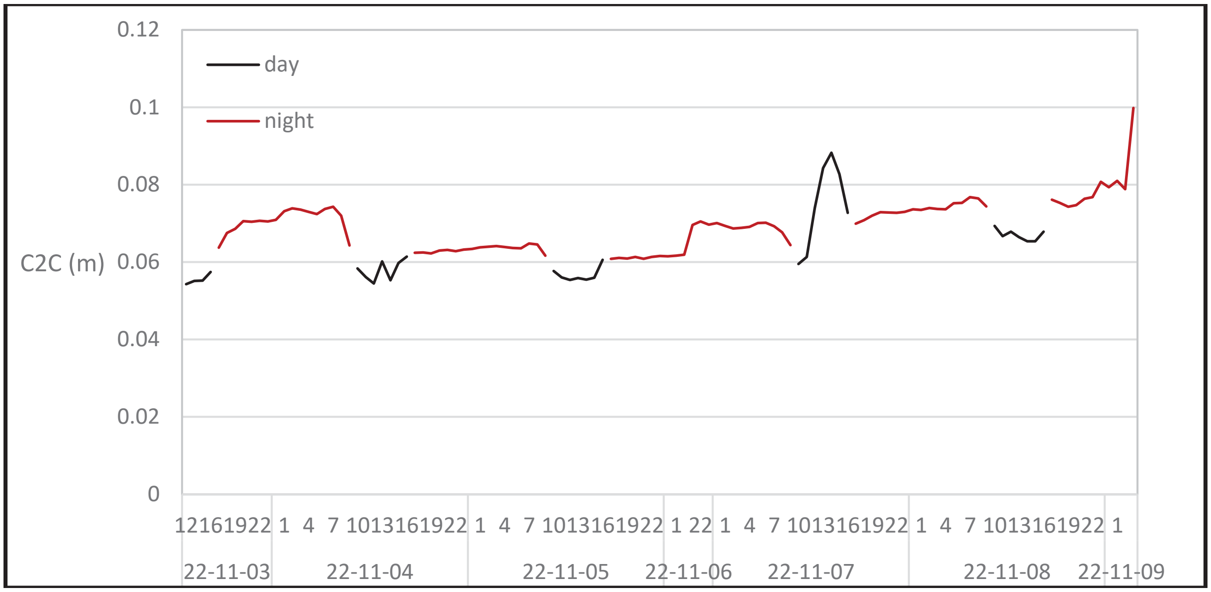

Figure 5.10 Average C2C measurements captured during day and night intervals

Considering the above variations, and the reported statistical spread captured by the standard deviation, a confidence interval can be established with regards to the realistic high-end of the C2C distribution. This value was computed for a confidence interval $\mathrm{CI} \approx 95\%$ with $\mu + 2\sigma$. Figure 5.11 plots the C2C upper Ci and average for the monitoring period. The values, while below the maximum C2C reported in

Figure 5.9 present realistic changes observed in the field and capture a logical and empirical framework for the analysis of meaningful changes. As can be noted from computations in the next section, these reported values are above the level of detection computed for this analysis, and thus represent more reliable results.

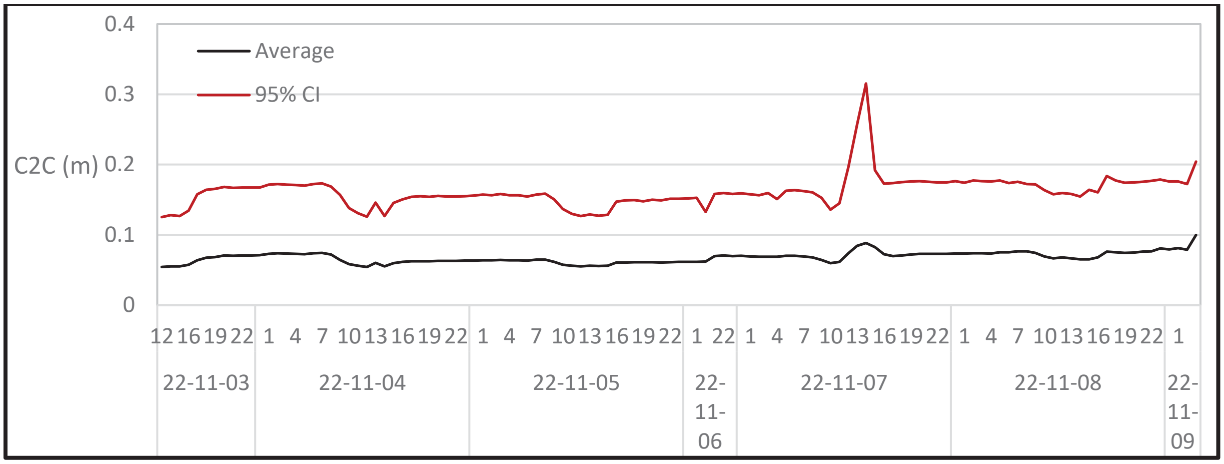

Figure 5.11 Change detection analysis reported in terms of average and 95 % C2C confidence interval computed as $\mu + 2\sigma$

The C2C measurements reported in the plots are statistical representations of the distributions from the HTF clouds generated at each time interval. This variation implies topographical variability over the surface considered. The analysis also presents absolute C2C values since no positive or negative direction is imposed. Thus, different zones with similar C2C values could be twice as changes from one another with one presenting positive change (i.e. bottom of the pile receiving debris) and one presenting negative change (material losses).

Figure 5.12 shows the HTF scan obtained on November 7th at 14:00. The scan shows viable topographical changes at the top and the bottom of the pile which further highlights this overall variability. It re-stated that C2C measurements are absolute distances, and do not fully reveal the directional magnitude of material displacement. Directional C2C could be considered for detailed inspection of the topographical changes in subsequent research.

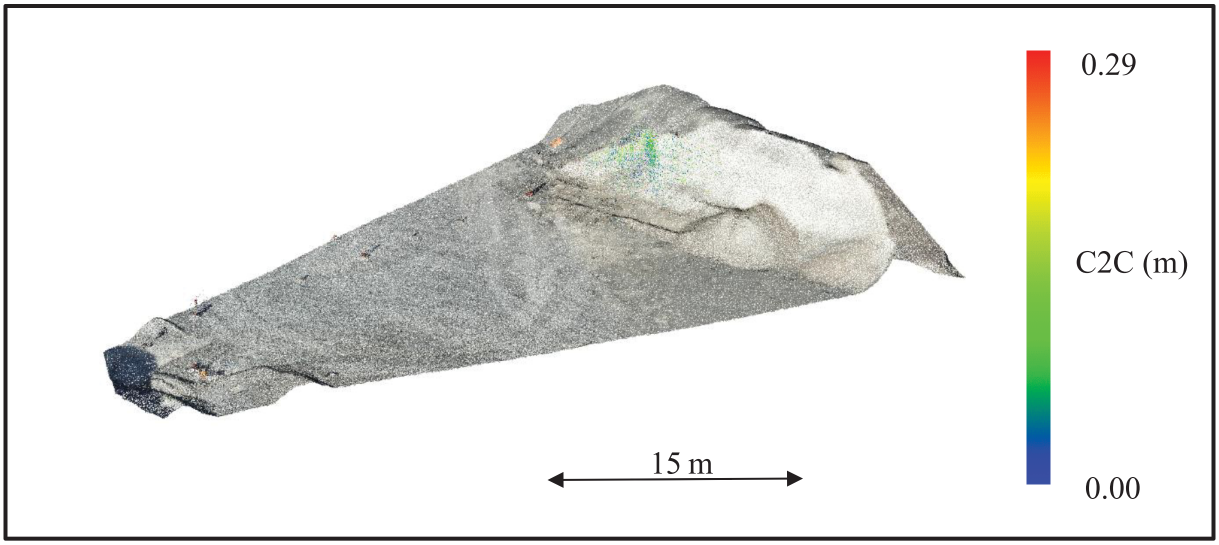

Figure 5.12 HTF scan on November 7th at 14:00 with color scale for C2C measurement and overlaid on top of the high resolution reference scan

A wind gust makes sense because wind can produce abrupt changes in the experimental configuration, particularly if it impacts loose materials or equipment (such as the cone or cables discussed previously). Wind gusts may cause the piles or equipment to move quickly or vibrate, which could lead to abnormalities in the point cloud data or an increase in standard deviation readings. Alternatively, the irregularity could also be explained by other variables such as variations in lighting or mechanical shifts in the equipment. Since these experiments were conducted outside, a variety of environmental conditions could have an impact on sudden changes.

5.5 Error analysis and LOD computations

Table 5.1 presents the different components of the level of detection computations. These parameters were obtained from the OEM of the LIDAR or derived following Equations presented in Chapter 4. The table compile all the error components and provide a LOD for the case study presented in this chapter.

Table 5.1 Uncertainty components and LOD computations for controlled failure pile experiment

Components	**Values**
Calibration error	2 cm
Repetitive measurement error	0.33 cm
Number of scans per time-interval (N)	2
$\sigma_{\mathrm{laser}}/\mathrm{N}$	1.65 cm
Beam divergence β	0.4 degrees
Number of measurements per time interval	2
$\sigma_{\mathrm{beam}}/\mathrm{N}\ \lvert \mathrm{I_B} \rvert \leq 30\mathrm{m};\ \theta_{\mathrm{I}} \leq 40°$	4.5 cm
Registration error reg83%	7 cm
$\mathrm{LOD}_{83\%}$	13.15 cm

The error from the first sensor calibration procedure is represented by the calibration error. Even while calibrating increases accuracy, there is still a small residual error, which raises the total uncertainty by 2 cm. This low repeating measurement error indicates a high degree of consistency in data gathering and emphasises the sensor's dependability in frequently recording the same measurement under comparable circumstances. The standard deviation of the laser takes into consideration the inherent uncertainty of the laser system caused by elements like environmental circumstances and sensor quality. Here, the overall error margin is marginally increased by the laser uncertainty. With distance, the measurement accuracy is impacted by the divergence angle, which reflects the laser's beam dispersion. While a wider angle causes more spread across distance and affects spatial resolution, a lower divergence produces a tighter footprint. Although more frequent scans could further improve data granularity and reliability, two measurements each time interval capture structural changes across intervals. The beam error increases the uncertainty by 7 cm for measurements up to 30 m and with an incidence angle less than 40°. This restriction emphasises how angle and distance affect measurement accuracy, with smaller angles and shorter distances typically yielding more accurate readings. Aligning point clouds from several scans results in the registration mistake. Compared to Chapter 6, it is marginally lower here, indicating less environmental or temporal alterations between scans. This is probably because alignment is made easier by a more regulated environment and a shorter time interval between scans. The smallest discernible displacement shift between scans is denoted as LOD. Smaller shifts might be within the error margin but changes larger than 13.15 cm can be reliably recognised.

The LOD computed here is noted to be fairly conservative, with incidence angles up to 40 degrees, and a registration error based on cloud to cloud distance computations. It is inferred here that the reportable LOD would be lower by considering Mesh-to-Cloud registration, and acknowledging that changes were measured mostly at near perpendicular incidence. The changes reported varied around 6 cm which is less then the LoD computed, but this change is consistent with the variations observed physically in the field. Further discussions are provided in a later chapter pertaining to avenues to improve LoD for this type of work.

5.6 Discussions

The extensive examination of the data gathered during the experiment and the conclusions made from it are the main points of debate in the St-Alphonse controlled pile failure monitoring experiment. This is a detailed description of the information.

The behaviour seen in the pile failure experiment is represented by the maximum and minimum values. These can represent the piles' greatest and lowest displacement, strain, or stress levels. The extreme measurements recorded during the experiment, such as the greatest displacement, and deformation, are represented by the maximum values. These maximum numbers are important because they matched times when the pile was under a lot of stress, which may be a hint that failure or severe damage was about to occur. Self-weight redistribution from the induced failure of the front-end loader, and possible environmental factors like temperature or moisture variation were the main stress sources identified during the experiment. In particular, stress peaks that correlated with discernible changes in displacement trends were noted on the first day of the high pile shape adjustment. These moments point to crucial points in the instability's development and imply a connection between the observed deformation patterns. The location of the pile's maximum strain was determined by monitoring these maximum values over time or under various load scenarios. This helped to pinpoint the breakdown point or the moments just before it. The pile had reached a critical threshold, as evidenced by a dramatic increase in maximum displacement. This causes a sudden change in behaviour that ultimately results in structural failure. The lowest readings frequently denote stable times or times when the pile is under less stress. They were crucial in determining whether the pile had shifted away from a stable or neutral posture, though. The minimum values may be losing stability before the maximum displacement is attained if they show a tendency of progressive reduction. By using these tendencies to anticipate when the pile will fall, this could show early symptoms of failure. While a decline in the min values suggested the loss of basic stability, a dramatic increase in the max values as shown in Figure 5.9 Maximum C2C measurement from the cloud distribution, on November 7th indicated the beginning of fast failure. These movements frequently correspond with visible alterations in the structural integrity of the pile, such as fissures, establishing a direct connection between the data and the pile's physical behavior. It was easy to identify whether the failure was instantaneous (i.e., rapid, with a sudden spike in displacement) or progressive (i.e., slow, with incremental increases in deformation over time) by looking at the max and min values. Understanding the pile's load-bearing capacity and potential failure modes under various circumstances required knowledge of this information. When the pile is getting close to its failure threshold, it can be determined by tracking the evolution of the maximum values. The pile may be getting weaker and closer to failure if max values were continuously rising under the same load. To anticipate failure and make necessary corrections or preventive actions, early detection is crucial. After loads are applied, min values aid in monitoring the stability of the pile. Even though the max values have not yet reached critical levels, a fall in min values over time (i.e. if the pile settled lower after each load) indicated permanent deformation or instability of the foundation.

The average figures provide a general idea of how the pile behaved during the experiment. These provided insight into the pile's behaviour under normal circumstances prior to failure and helped determine the pile's approximate proximity to failure at different points in time. The data's variability was quantified using the standard deviation. A low standard deviation implied more uniform behaviour, but a high standard deviation indicated inconsistencies or outside influences altering the pile's behaviour.

Interference from the cone used to isolate the prototype was one of the problems with the data quality. The prototype may have had partial readings, reflections, or shadows added to the point cloud data by the cone that was used to isolate it during scanning. The accuracy of the detecting system can be decreased by these artefacts, which can mask subtle but significant aspects of the behaviour of the pile. The detection system can more accurately record the behaviour of the pile without any outside noise by eliminating this disturbance. As a result, failure processes may be more clearly identified and data clarity increased. Manual editing and box filters were used to remove the noises from CloudCompare. Floating points in the point cloud may have been introduced by background metal objects throughout the experiment, introducing erroneous data that doesn't match to any portion of the pile or its behaviour. These floating points have the potential to skew the data and produce false conclusions. Throughout the data preprocessing phase, these metal fragments were located and eliminated from the point cloud. This required the application of particular filtering methods that identified and separated floating points according to their properties or positions. The standard deviation plots illustrated how the elimination of these metal artefacts made the dataset more consistent and dependable.

The degree of detection for minute deformations or early indicators of pile failure increased with the removal of both the cone and the floating metal points. These adjustments produced more accurate measurements, which made it possible to monitor the experiment more precisely and identify failure stages more accurately. The removed metal fragments and cone (represented in the small orange zones in Figure 5.5) from the cleaned dataset made it possible to track the deformation of the pile over time with greater accuracy. Because of the clarity, it was easy to determine if the pile underwent a sudden collapse, which is suggestive of a rapid and catastrophic failure, or gradual deformation, which is indicative of a protracted and progressive failure. In this experiment, a mixed failure mode was revealed by a steady increase in deformation followed by a rapid spike in displacement. The pile first showed signs of progressive distortion, but as critical weights were reached, the fall became more abrupt. In the noisy dataset, where interference may have obscured crucial transitions between slow and rapid failure modes, these behavioural changes were more difficult to identify.

A far clearer picture of the distribution of distortion across the pile was given by the cleaned point cloud. Eliminating the noise made it easier to determine if the deformation affected the entire structure or only the top, middle, or bottom of the pile. The dataset demonstrated that the early deformations were confined to the area where the load was concentrated, which was the base of the pile. Deformation traveled up the pile over time as the load grew, leading to more dispersed failure. As more material was added or moved around inside the pile over time, the overall weight rose and the lowest levels of the pile were even more compressed. We call this slow increase in load the "growth of the load." Initially focused at the base, the impacts of this increased tension spread upward through the pile as structural modifications took place. This indicates that the upper layers started to move and adapt as more material settled and applied pressure below, eventually creating a more extensive pattern of deformation. After cleaning, these patterns were much easier to identify because the original dataset's floating metal points produced misleading reflections and occlusions that covered up these vital details.

It was clear that the pile's response was very nonlinear by comparing its behavior under different loading stages. Little, elastic deformations were formed during the initial stages of loading, and these could be reversed when the load was released. Nevertheless, plastic (irreversible) deformations became more pronounced as the load got closer to the pile's failure threshold, ultimately resulting in collapse. In the cleaned dataset, this shift in behavior from elastic to plastic was more evident. Whereas the cleaned dataset made it possible to pinpoint the exact moment at which the pile crossed the elastic-plastic boundary, which was shown in Figure 5.8 on November 4th between 10 am and 1 pm, the noisy data's floating points and interference made it challenging to discern small-scale elastic deformations from random noise.

It was considerably easier to find minor cracks and localized deformations when the cone and floating metal pieces were removed. These finer details had previously been obscured by noise in the original dataset, such as spurious reflections from metal fragments, making it challenging to discern between interference and the real deformations in the pile. Initial failure indicators, such as change in pile geometry close to the base shown in the figures above between Figure

5.8 and Figure 5.11 between 4 pm on November 3rd and 10 am on November 4th, were made visible by the cleaned dataset and were essential for determining when and where the pile would finally collapse. The initial dataset did not allow for the reliable detection of these tiny features.

Significant defects including signal interference, false reflections, and occlusions were introduced by the cone and metal parts, which led to an incomplete acquisition of data. Measurement uncertainties resulted from these artifacts, particularly when attempting to pinpoint the precise location and magnitude of deformations. These issues were resolved, yielding a significantly cleaner dataset, by manually removing the cone and using box filtration to remove floating points. This decreased the uncertainty in crucial measures like displacement and strain and increased the experiment's overall accuracy.

Cleaner, less-interference experimental setups could be beneficial for future research. Noise in the dataset may be decreased, for instance, by hiding shiny surfaces or eliminating extraneous items from the experimental field. Furthermore, the procedure could be streamlined and the chance of human error decreased by utilizing more sophisticated point cloud techniques, such as automated noise detection and removal. Automation would guarantee that the dataset is constantly cleaned, even in real-time, and enable speedier processing. Future trials may be far more dependable and efficient if artifacts like cones and metal fragments were automatically removed. The use of real-time algorithms that can recognize and eliminate interferences as they happen will free up researchers to concentrate on clean data analysis rather than laborious human editing. When human interaction is impracticable, such as in large-scale studies or long-term monitoring initiatives, this could be especially helpful.

The knowledge acquired from this experiment can be immediately applied to geotechnical projects in the real world, especially when it comes to the planning and maintenance of pile foundations in civil engineering. Engineers to create more durable foundations that are less likely to collapse suddenly by having a thorough understanding of the failure patterns of piles. Early detection of deformations would enable the implementation of corrective actions before the occurrence of failure. The long-term structural soundness of piles might be ensured through routine monitoring with clean, high-quality LiDAR information, enhancing the dependability of vital infrastructure. Future geotechnical projects should include automated noise removal techniques, high-resolution LiDAR systems, and cleaner experimental setups as regular procedures. These enhancements would guarantee that data quality stays high and lower the possibility of results being misinterpreted because of interference or noise. The experiment's results also point to the necessity for greater study on the application of multi-sensor systems and real-time monitoring programs to offer even more precise insights into the behavior of piles during failure.

CHAPTER 6

CHANGE DETECTION MONITORING IN YUKON WITH LOD ANALYSIS

6.1 Scope of analysis

This chapter presents a change detection monitoring case study that implemented the Blickfeld Cube sensor following an experimental set up comparable to Chapter 3. This monitoring work is part of a larger research initiative to study glacier retreat and hydrological processes in Yukon. The experimental field work and raw data collection was carried by a team of graduate researchers at ETS from the HC3 lab. Detailed information on the research program, subsequent findings, and hydrological developments derived can be found in various publications by Baraer and collaborators (i.e. Chesnokova et al., 2020; Charonnat et al., 2023). The present chapter revisits high-temporal frequency monitoring data collected as part of the research program. Experimental settings and survey methods are summarily presented for context, followed by the monitoring results. The change detection analysis protocol developed in Chapter 5 is implemented to quantify uncertainty and level of detection of this work. Additional considerations are given to the practicality of this analysis and the long-term implementation of the monitoring system. An alternative approach relying on change detection with respect to a reference low-resolution Blickfeld scan is proposed to address limitations arising from high registration scan errors.

The goal of this investigation is to ascertain the ability of the developed prototype to monitor changes and quantify the level of confidence associated. The intended application of this prototype, as outlined in the introduction of this master’s thesis, is to provide quantifiable perspective towards changes in order to ascertain if and when changes are happening and develop an objective sense of the uncertainty associated with the data collection and change detection results. The data considered spans from Summer of 2022 to Fall of 2023.

6.2 Experimental Settings

The experimental work presented in this study took place at Grizzly Creek, in Yukon, Canada. Grizzly Creek is characterized by cold weather, snow, ice, and rough terrain.
Figure 6.1 presents the geographical location of the experimental site.

Figure 6.1 Grizzly creek location where the experimental field work was carried as part of this chapter
Taken from Google Maps (2022)

As part of the HC3 research program in Yukon, drone surveys are taken few times a year to measure changes in the ice shelf at large scale. The drones are equipped with cameras to capture topographical conditions from photogrammetry analysis. Pix4D is used to process the collected pictures and generate a topographical data set for the landscape surveyed.

Figure 6.2 shows a topographical data set of the monitored zone captured via photogrammetry. The zone of high temporal frequency monitoring is highlighted in the figure. The larger area is monitored a few times a year through UAV-based surveys. The highlighted monitoring zone is the span captured by the Blickfeld Cube during the high temporal frequency monitoring phase. The indicated Y and X axes represent North and South respectively.

Figure 6.3 shows a picture of the monitored zone. The area is characterized by rough terrain with the presence of snow and some negligible vegetation.

Figure 6.4 show the topographical data set of

Figure 6.2 with color scale for vertical elevation. It can be noted that the surveyed location is in a trench which accumulates more severely precipitations (water and snow) and facilitates change detection analysis. For the purpose of this investigation, the topographical scans showed next X, Y, and Z vectors which represents East, North, and Verticality respectively. All units for scale and C2C measurements in the next sections are in meters (m).

Figure 6.5 shows the high resolution topographical data set with color scale for point density. The average point density is approximately 200 points per square meter, or 7 cm point spacing.

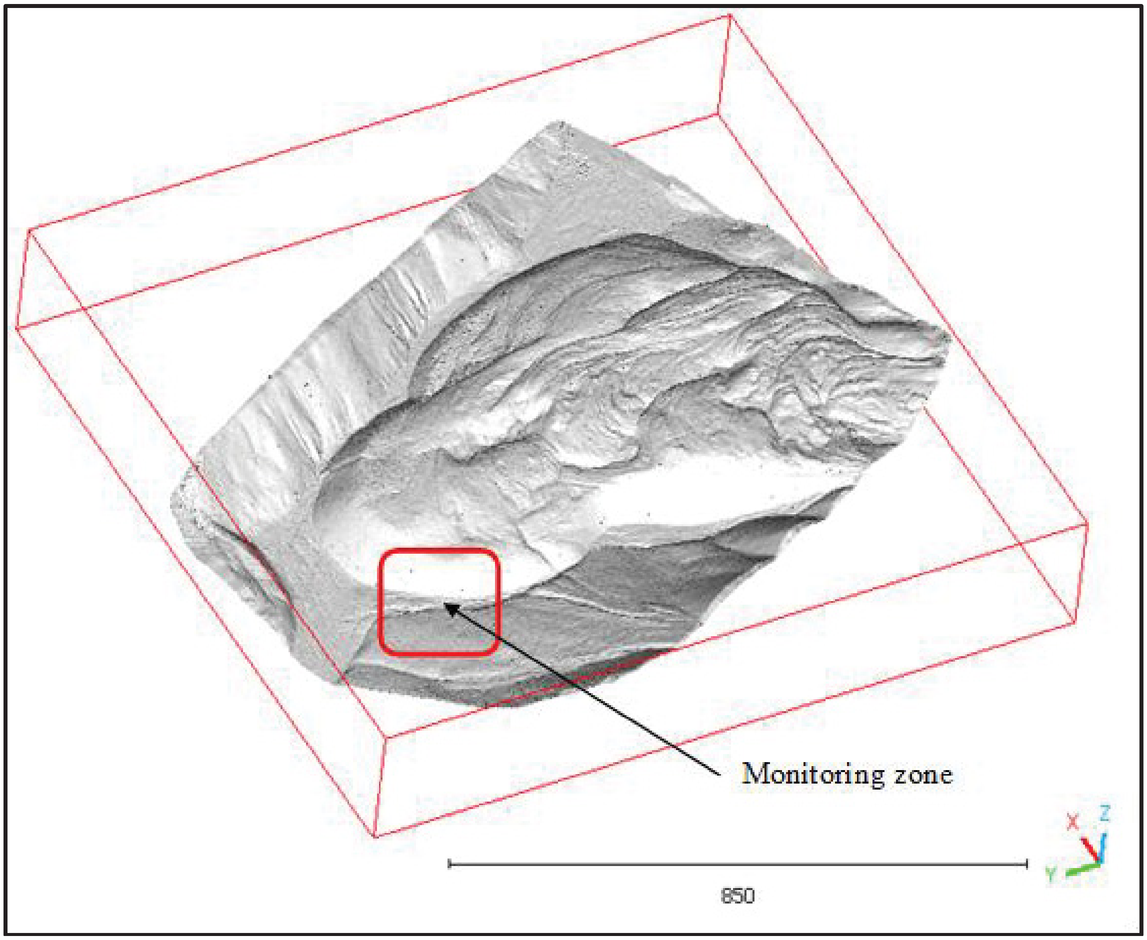

Figure 6.2 Topographical model of the zone monitored at Grizzly creek

Figure 6.3 Picture of the monitored zone for high temporal frequency change detection monitoring

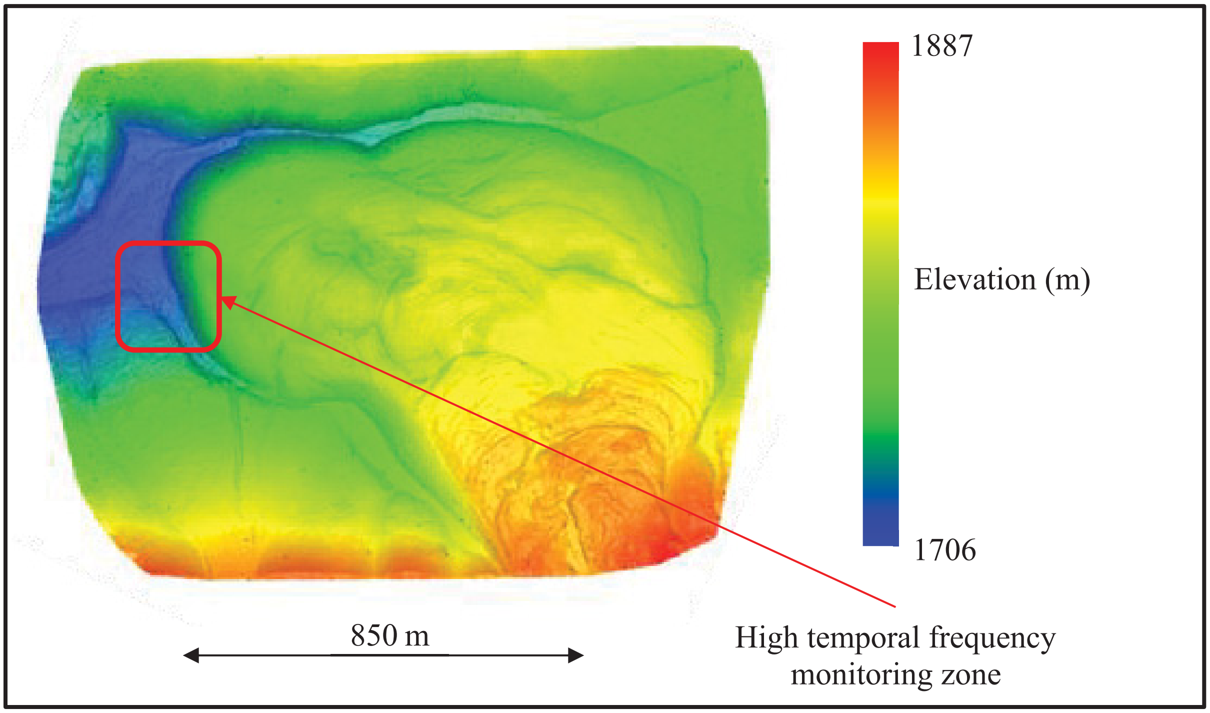

Figure 6.4 Topographical data set with color scale for vertical elevation

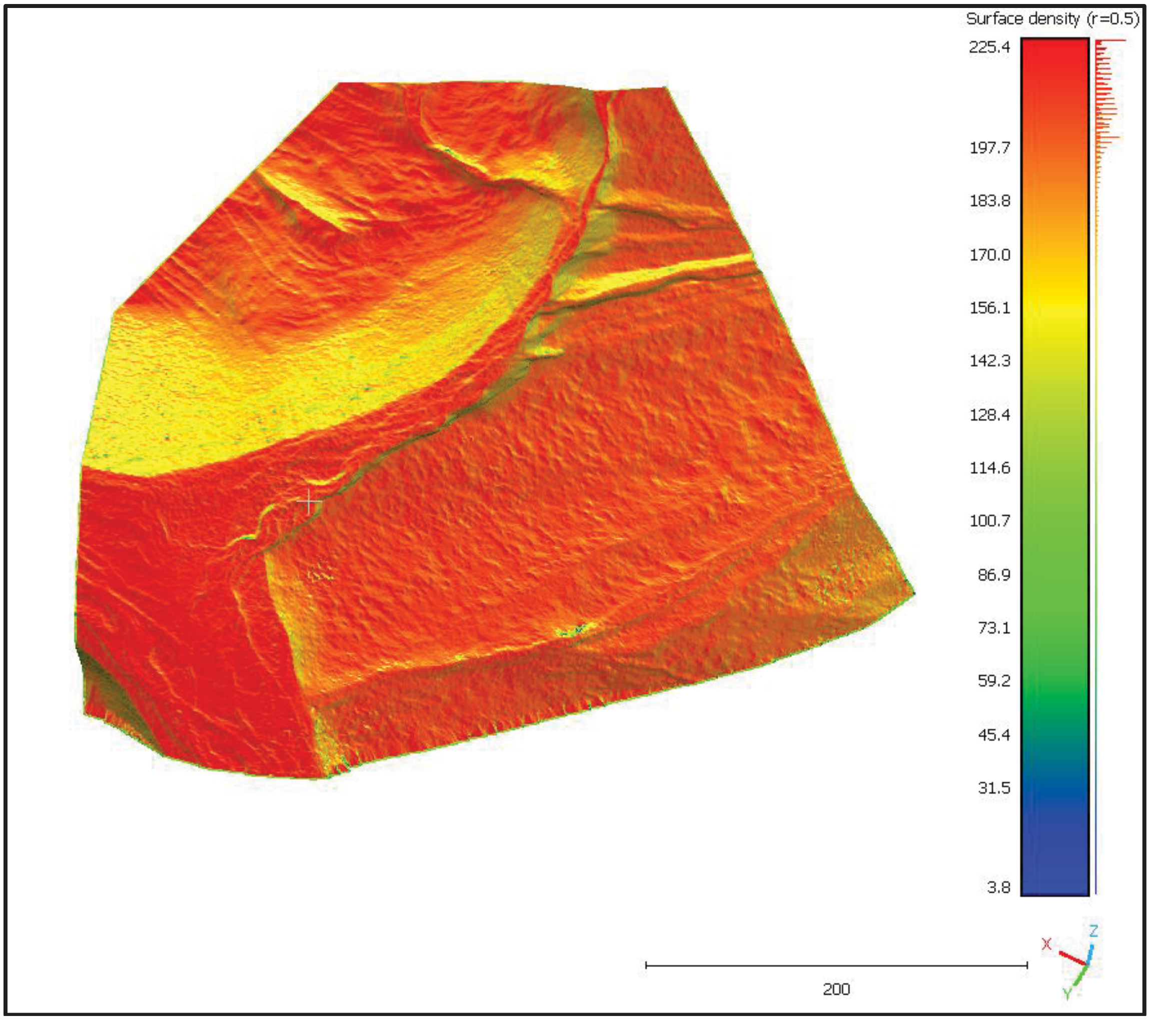

Figure 6.5 High resolution topographical data set with color-scale for point density

The HTF monitoring system was positioned approximately 20 m from the floodplain, and around 60 m from the mainstream channel, oriented in the southwest direction.

Figure 6.6 show a picture of the set up which is essentially similar to the one presented in Chapter 5. Six times a day, every four hours, data were taken to record time-dependent changes in the ice shelf.

Figure 6.6 High temporal frequency monitoring system used at Grizzly Creek
Taken from Bastien Charonnat (2022)

6.3 Initial scan placement

The change detection analysis protocol implemented in this chapter follows the method described in section 4.2.2 and implemented in Chapter 5. A photogrammetry-based drone survey collected in August 2022 was selected as the high-resolution scan of reference as part of the change detection analysis (see Figure 6.2, Figure 6.4, and Figure 6.5. The original scan obtained contained over 170 million points with a size of nearly 7 GB. The file was cropped at the monitoring zone to provide more manageable settings for further manipulations (Figure 6.5). The cropped section contained approximately 29 million points.

The change detection analysis carried in this work was performed between each Blickfeld cube scans, and the original high resolution data set, similar to Chater 5. Change detection analysis was also performed with respect to a reference Blickfeld scan (henceforth referred to as the low-resolution reference scan) dated September 30th, 2022. As will be discussed later, this second change detection protocol was implemented to verify physical bias between the high-resolution scan and the HTF set up. It was also introduced as a potential alternative solution for when high resolution scans are not available or problematic.

Before computations were carried, the low-resolution reference scan was placed with respect to the high-resolution scan to provide a consistent geographical frame of reference. It is noted that some of the early scans (before mid September 2022) exhibited issues with data collected due to condensation in the lens. This issue was addressed by reverting to a different more suitable lens. While the original high-resolution scan is dated from August 2022, the earliest data considered in this work is dated September 23rd, 2023.

The 8am scan of September 23rd was arbitrarily selected as the low-resolution reference scan due to a slightly better point density than before. This change in scan density appears to arise with higher snow accumulation yielding a more direct incidence angle on greater surface span. The span of approximately 30 days between the high-resolution and low-resolution reference scans led to some topographical inconsistencies between the surfaces due to snow accumulation. This was a driving factor for also considering change detection with respect to the low-resolution scan.

The R-ICP method to place the low-resolution scan with respect to the high-resolution scan involved 18 iterations to achieve a mean C2C error of 0.18 m, and $reg_{83\%}$of 0.281 m. While the computations and experimental work carried next remain of interest, it is noted that such registration error is fairly high and would impede robust advanced geoscientific change detection. This error is due, however, to the time interval between the original scan and the monitoring period as underscore by the much lower registration error computed with the same technology in the previous chapter. Some considerations are provided in a later section to limit the impact of such conditions.

Figure 6.7 plots the registration error with respect to R-ICP iterations carried during the scan placement work.

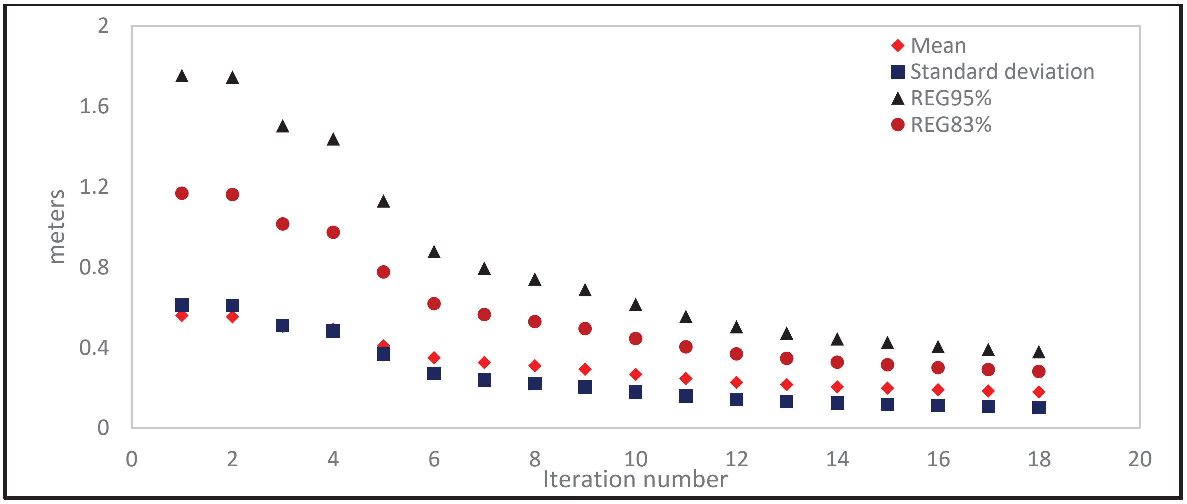

Figure 6.7 Registration error graph for RICP number of iterations

6.4 Change detection results

Change detection analysis was carried for all HTF scans with respect to the high-resolution and low-resolution scans. Distances between the scans were computed using cloud-to-cloud (C2C) distances with CloudCompare. The results are compiled in terms of statistical figures of the resulting C2C distribution for the considered scan interval.

The results present increasing variability with decreasing time-subsampling. Time-subsampling (i.e. considering the average C2C during a week) presents very interesting perspectives towards evaluating meaningful and durable changes during longer periods as opposed to considering rapid superficial variations.

Figure 6.8 plots C2C statistical average and standard deviation averaged on a monthly basis. This coarse sampling of the data sets presents low overall variably and provides rapid insight on overall trends measured during the time interval.

It can be noted that the greatest C2C variation is measured during Q1 and Q2 of 2023. These trends are consistent with seasonal variations and the expected snow accumulation period. Both analyses present similar trends in that regard.

It is noted from the plot that the trends are very similar between the high resolution and low-resolution reference scans. It is inferred that the low-resolution reference analysis tends to exacerbate trends. For most of 2022, average and statistical variably are lower for the low-resolution reference analysis. However, the trends are reversed during Winter 2023. It is ascertained that large variation would be more apparent with the lower-resolution reference scan given the lower point density which compounds the change detection results. This aspect could be significantly reduced by considering a mesh-to-cloud type change detection method. This concept is further discussed in a later chapter.

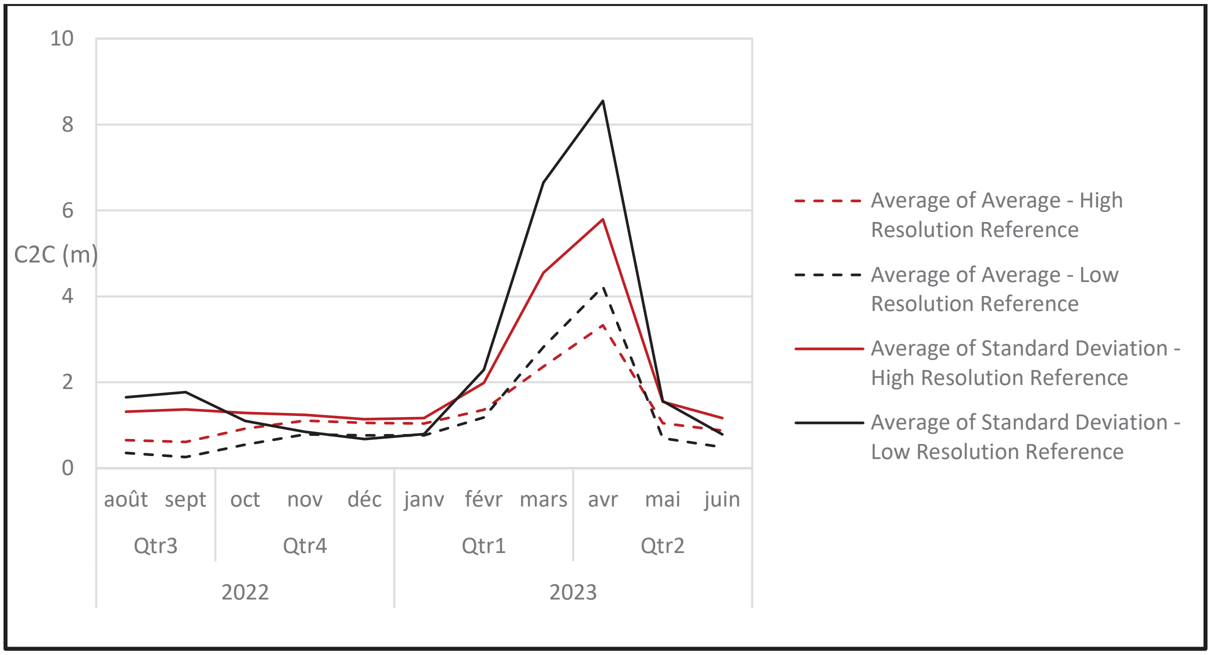

Figure 6.8 Change detection analysis results with respect to high and low resolution reference scans with monthly averaging

Figure 6.9 and

Figure 6.10 present change detection analysis results for weekly averaged data. In the plots, weeks are represented as week number in the year (from 1 to 52). Figure 6.9 show the results between weeks 35 and week 53 (August and December) in 2022. Figure 6.10 show the results between weeks 1 and 22 (January and June) in 2023. The trends appear to be comparable to the previous figure, and feature more apparent variability. This finer resolution provides better insight on time intervals associated with seasonal variation. It is observed for example from Figure 6.10 that an important reduction is accumulated snow converges to week 18.

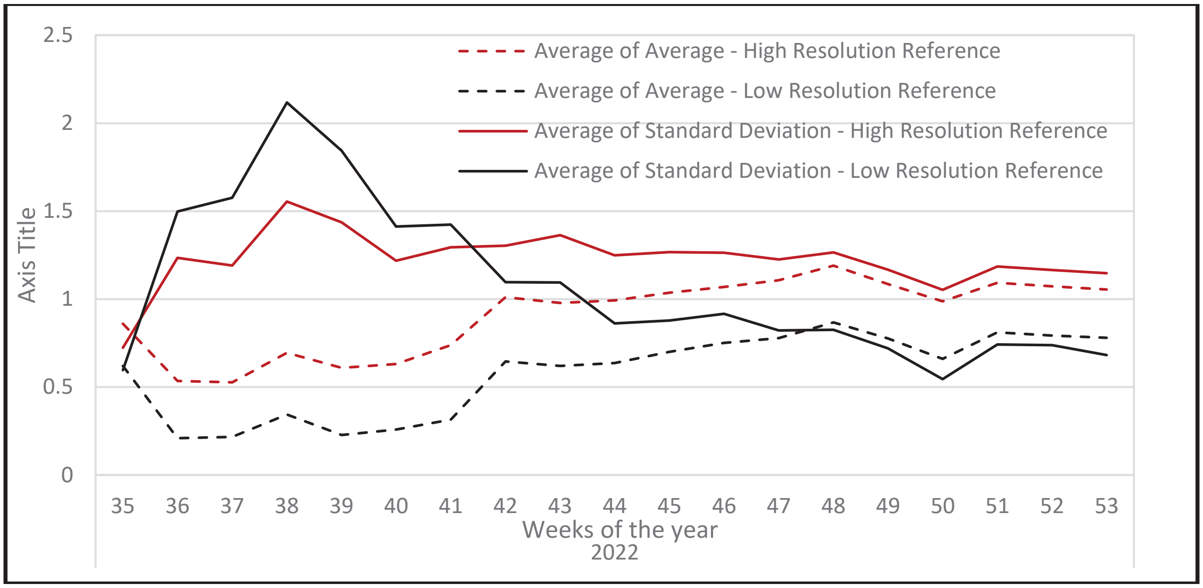

Figure 6.9 Change detection analysis results with respect to high and low resolution reference scans with weekly averaging for 2022 data

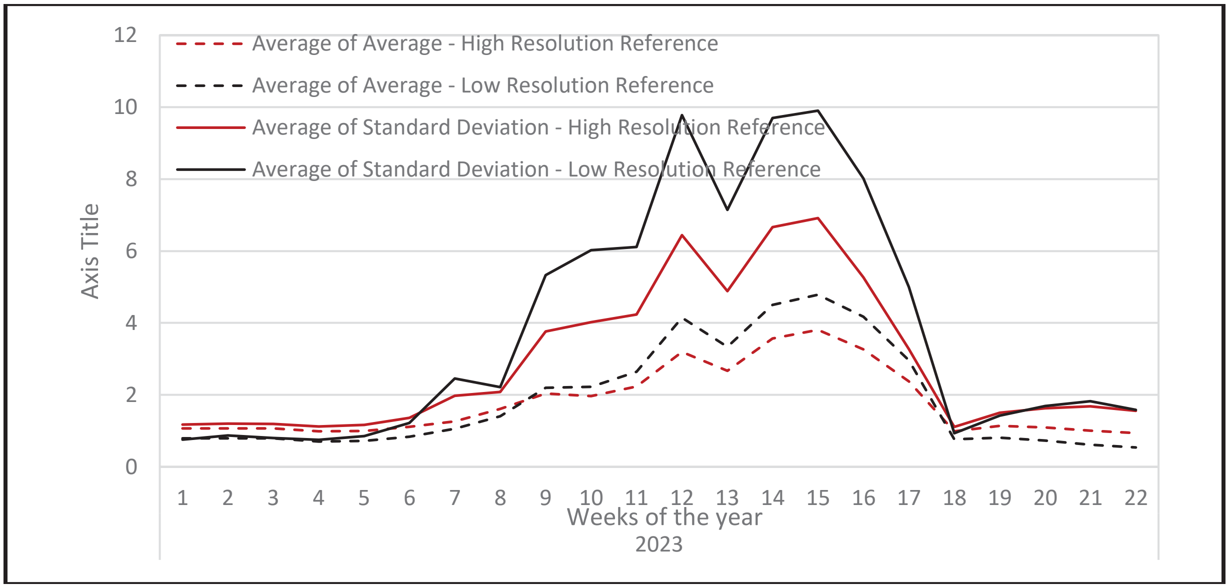

Figure 6.10 Change detection analysis results with respect to high and low resolution reference scans with weekly averaging for 2023 data

It is noted from the above results that the statistical variability of C2C measurements appear fairly high as denoted by the standard deviations computed. This statistical variability is made apparent by considering the maximum values computed during the monitoring period.

Figure 6.11 plots the maximum C2C values computed (averaged on a monthly basis) for the analysis performed. It can be noted that the values measured are very high compared with the computed means. This result explains the larger statistical variability.

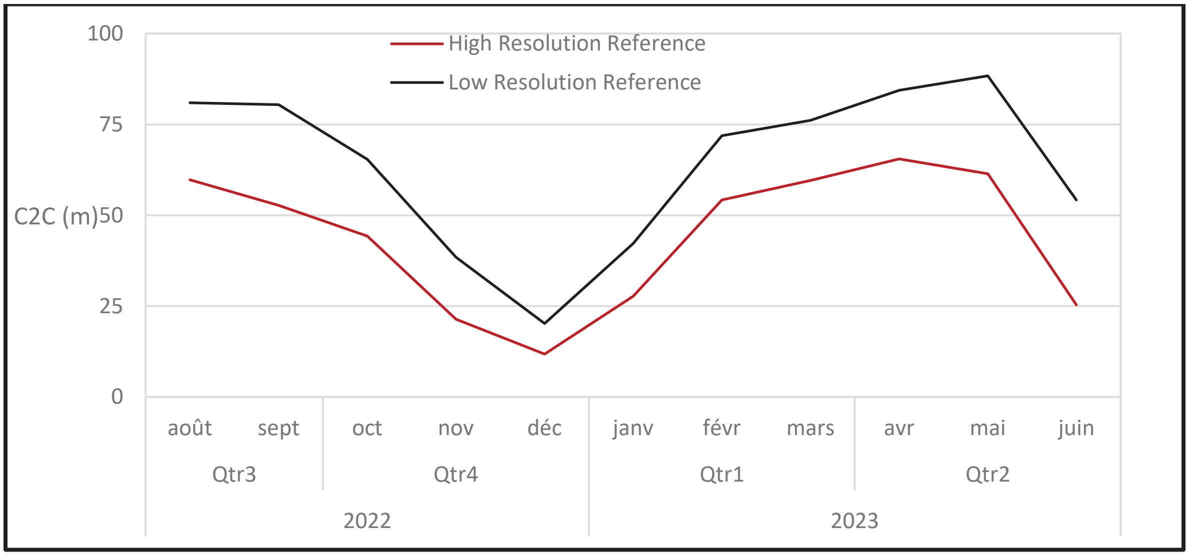

Figure 6.11 Maximum C2C values measured from the change detection analysis developed on a monthly average

This statistical variability was further investigated by inspecting two HTF scans. The first scan is the low-resolution reference scan dated September 23rd, 2022. The second scan was taken from one of the highest C2C measurement as noted in subsequent analysis.

Figure 6.12 and Figure 6.13 show the respective placement of the two scans when visualized simultaneously on CloudCompare. It can be seen from the figures that much more data is compiled on the North side of the surveyed zone for the reference scan then for the test scan. This aspect is again probably due to scan incidence angle on the material, which decreases with increasing snow accumulation on the North bank of the trench. This aspect would arise purely from a geometrical paradigm. It could be addressed by increasing substantially the elevation of the HTF set up.

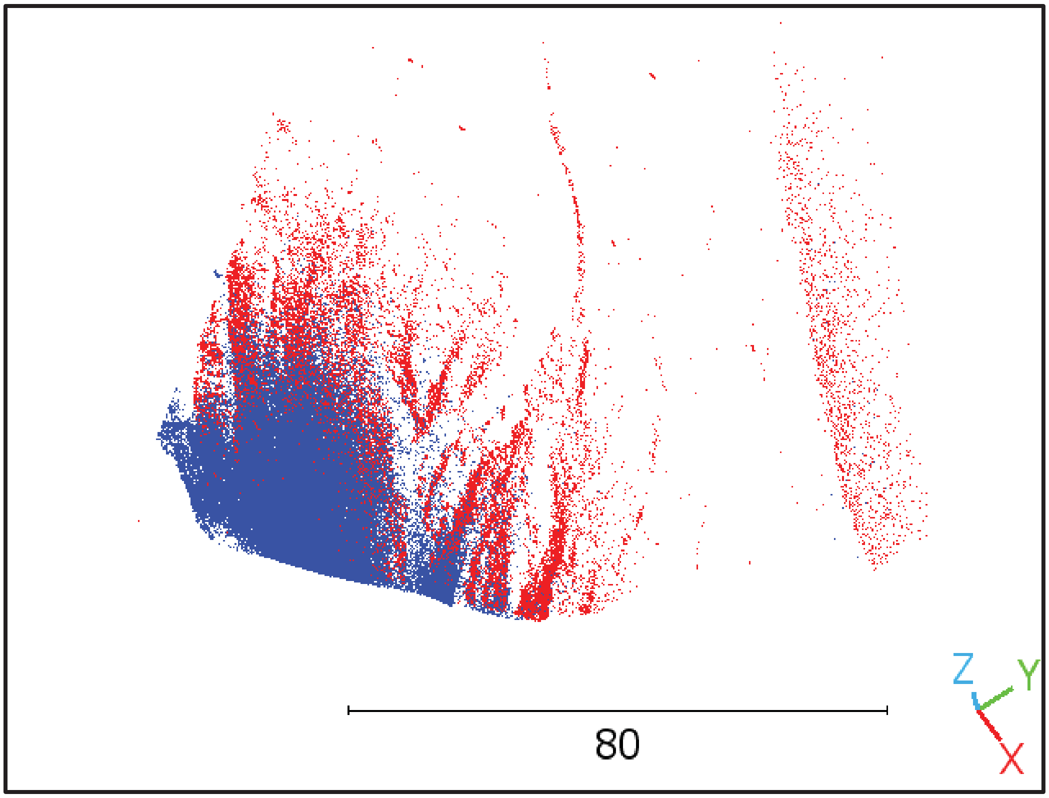

Figure 6.12 High temporal frequency scans respective placement for low-resolution reference scan dated September 23 2022 (red) and scan taken on March 30 2023 (blue)

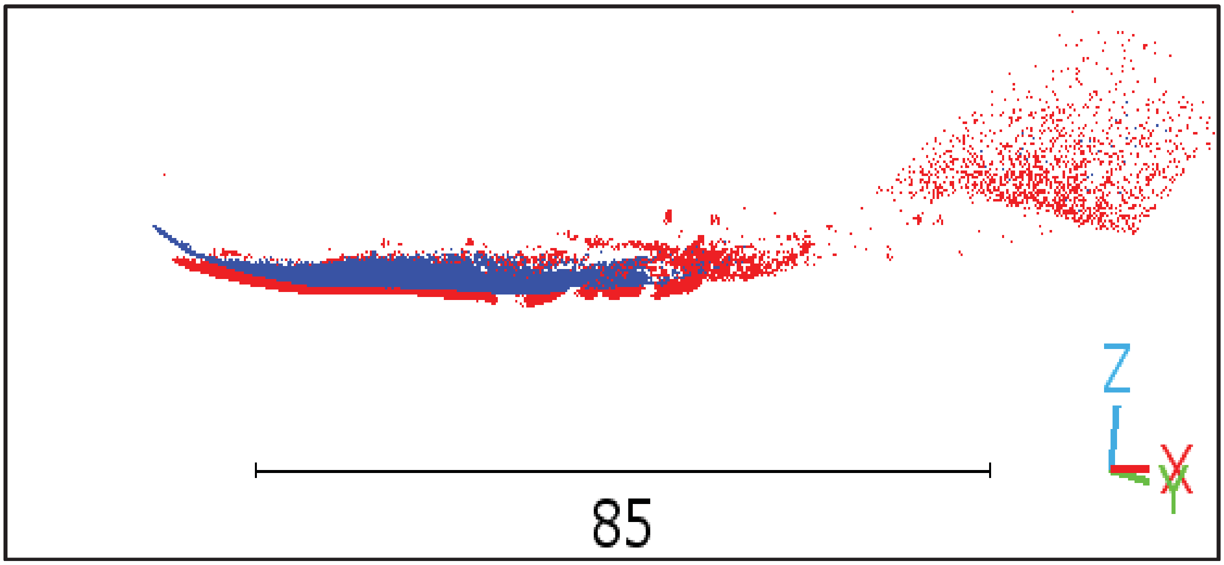

Figure 6.13 High temporal frequency scans respective placement for low-resolution reference scan dated September 23 2022 (red) and scan taken on March 30 2023 (blue)

The importance of scanning mutually exclusive subsets is further investigated by considering C2C color scale distribution for the scan taken on March 30th, 2023.

Figure 6.14 presents the C2C distribution for the scan computed. It can be noted that the high C2C distances are computed on the South part of the scan.

Figure 6.15 shows a different view of the scan and include the low-resolution scan in red. It can be noted that the most important C2C values arise where the low-resolution scan stops on the left of the figure (South). The high values of the C2C computations are thus biased by mutually exclusive subsets of the data. Upon further inspection, the C2C average measured on that day was 4.63 m. The smallest vertical distance measured between the two scans is approximately 1.2 m. Three additional zones of high C2C values impart higher C2C averages. One is located near the top of the South Slope, one further North-west, and one East of the zone where the trench is deeper. These three larger C2C subsets are topographically driven and therefore are relevant to the analysis. These topographical features and their influence on C2C analysis underscore the limitations of detailed geomorphological change detection beyond threshold and sensitivity analysis. Nevertheless, the average value arguably provides the most representative measurement for overall changes in this work, while the standard deviation reflects upon the statistical variability.

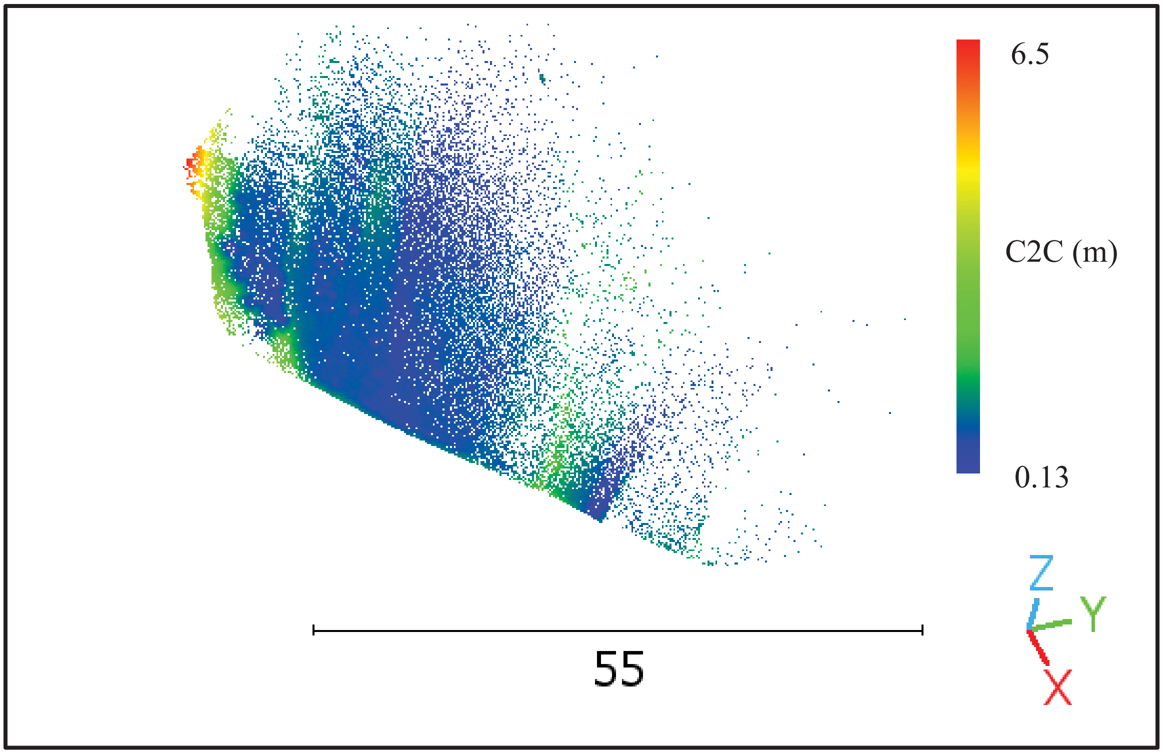

Figure 6.14 C2C distances between scan taken on March 30th 2023 and low-resolution reference scan

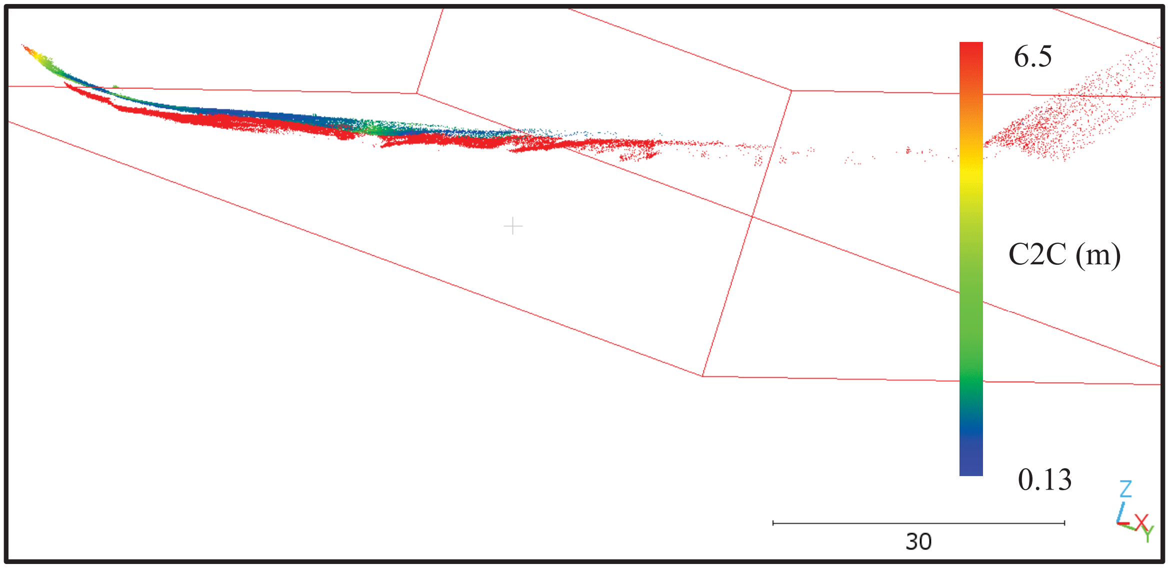

Figure 6.15 C2C distances between scan taken on March 30th 2023 and low-resolution reference scan (The scan in red is for the low-resolution reference scan)

To further expand upon the nature of the results and the inherent variability, the results are presented in

Figure 6.16 considering daily averaging. The plot is for the high variation periods of March and April of 2023. The plot shows average for the C2C distribution.

The plot shows important variations over periods of a few days. The variations are similar for both the high resolution and low-resolution references. It is inferred from the investigation performed with

Figure 6.15 that the average distances are representative of the distribution, influenced by topographical features, and from mutually exclusive monitoring sub-sets. Considering the observed variability, and the influence of topographical features on the result, the value of daily (and hourly) trends is deemed less relevant than coarser temporal trends.

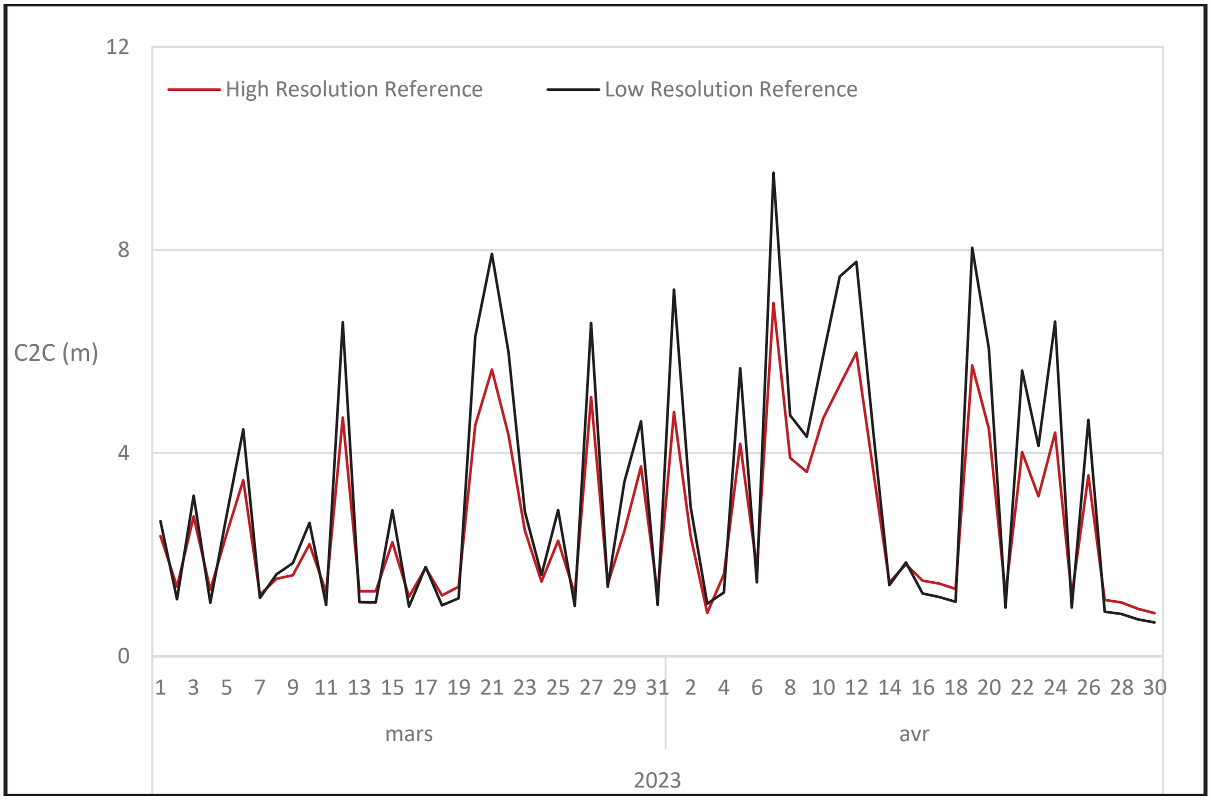

Figure 6.16 Change detection analysis results with respect to high and low resolution reference scans with daily averaging for 2023 data

It is noted that the statistical and temporal variability of the plots are consistent for the low and high resolution reference analyses. Results from the high resolution reference are further investigated with the data set from March 30th. Figure 6.17 shows the HTF scan from March 30th overlaid to the high resolution reference scan. It is observed that the same section of the HTF scan exhibit high C2C measurements as noted in

Figure 6.14, and

Figure 6.15. This subset coincides with a higher snow accumulation captured with respect to both reference systems. The comparisons are limited in that regards as the low-resolution reference scan high C2C measurements were due to some extent to point cloud mutual exclusive subsets, while the high-resolution reference scan appears to be due to a geomorphological change associated with snow accumulation.

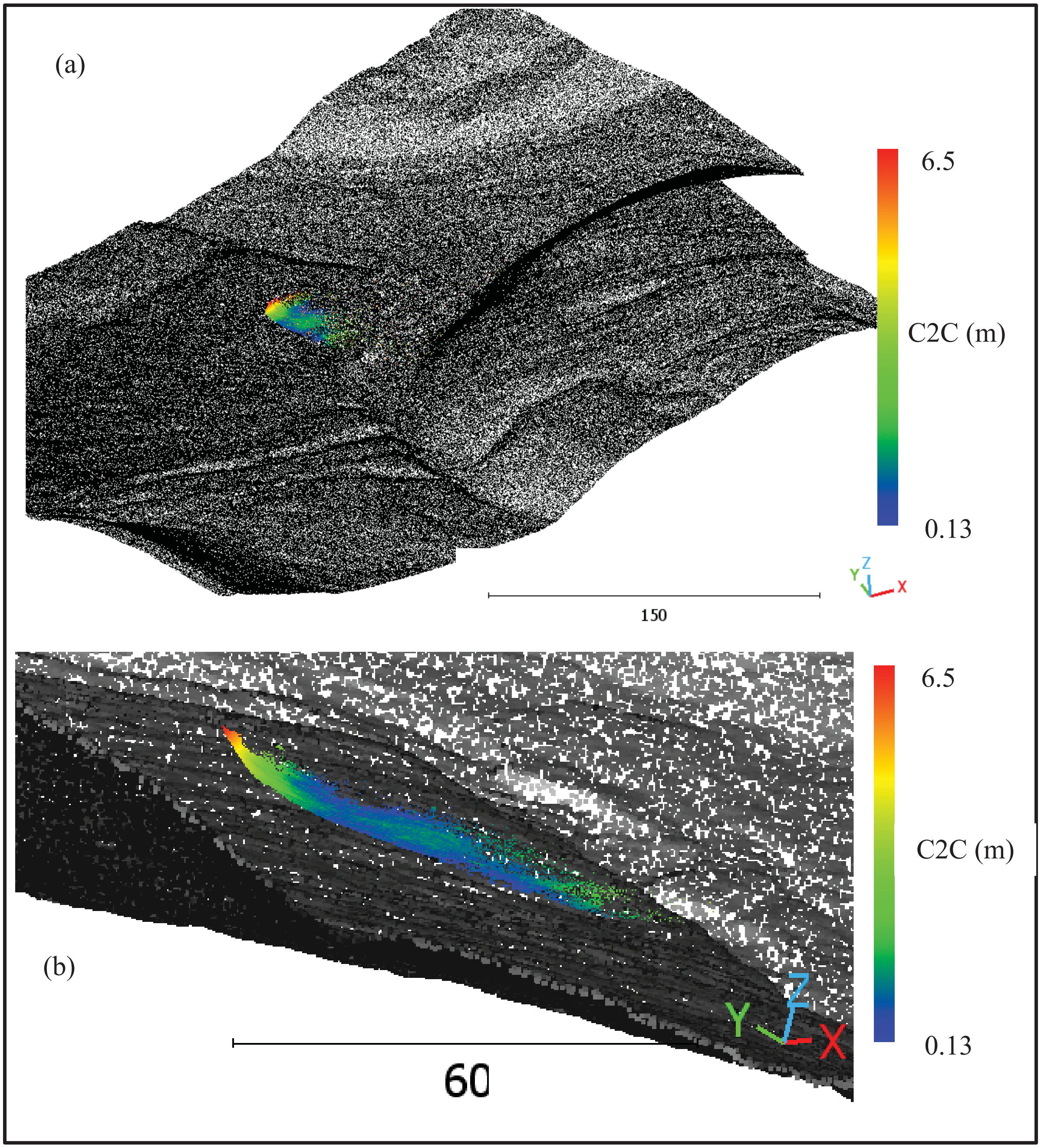

Figure 6.17 March 30th 2023 scan with color scale for C2C with respect to the high resolution reference scan (a) pseudo-isometric view and (b) from an arbitrary angle to emphasize the gap between the two scans

6.5 Level of detection analysis

Table 6.1 presents the different components of the level of detection computations. These parameters were obtained from the OEM of the LIDAR or derived following Equations presented in Chapter 3. The table compile all the error components and provide a LOD for the case study presented in this chapter.

Table 6.1 Uncertainty components and LOD computations for Yukon monitoring case study

Components	Values
Calibration error	2 cm
Repetitive measurement error	0.33 cm
σ_{laser}/N	1.65 cm
Beam divergence β	0.4 degrees
$\sigma_{beam}/N \ \ \lvert I_B \rvert \leq 50\ m;\ \theta_I \leq 60°$	11.5 cm
Registration error $reg_{83\%}$	28.1 cm
$LOD_{83\%}$	41.25 cm

The error resulting from the sensor calibration procedure is reflected in the calibration error. Although frequent calibration guarantees that the LiDAR system's readings stay precise over time, tiny inaccuracies may still arise from inconsistencies. According to the minimal repetitive measurement error, the sensor reliably and accurately measures the same spots in comparable circumstances. This low value suggests that the apparatus can consistently reproduce measurements. A number of variables, including surface reflectivity, air conditions, and sensor quality, affect the laser system's intrinsic 1.65 cm measurement uncertainty. The laser beam's spread angle, or beam divergence, has a value of 0.4 degrees. While greater beam divergence causes more dispersion in the laser footprint, less divergence produces finer measurements and improved spatial accuracy. The beam error is 11.5 cm at a distance of up to 50 meters and an incidence angle of up to 60 degrees. This inaccuracy takes into consideration things like atmospheric dispersion and the laser's footprint spreading over longer distances. This inaccuracy tends to rise with larger distances and incidence angles. The inaccuracy created during the alignment of point clouds from numerous scans is represented by the registration error. The temporal intervals between the high-resolution and later Blickfeld images are probably the cause of its comparatively high value. This latency makes accurate alignment difficult and leads to increased registration mistakes, especially when combined with surface or environmental changes over time. The smallest discernible change between successive scans is indicated by the Level of Detection at the 83% confidence interval. Smaller changes may fall within the margin of error, but any surface displacement or change beyond 41.25 cm can be reliably detected, according to this LOD value. The measured displacements in this study generally ranged from 1 m to 10 m, with most observed shifts being on the order of 2 m. This suggests that while some minor variations may be within the error range, larger displacements indicate actual material movement. In order to minimize registration mistakes, particularly in situations where there are significant temporal intervals between scans, these values emphasise the necessity of regular, high-resolution data capture. Future suggestions to maximise data fidelity in long-term monitoring applications may involve synchronised scanning or modifications to sensor placement and environmental control.

6.6 Discussion and limitations

This chapter presents a case study for change detection analysis using the HTF configuration implemented in Chapter 5. The investigation in this chapter aimed to ascertain the potential of application for this system towards high frequency change detection and derived geomorphological conclusions. The analysis and associated results suggest that the system can readily be used to monitor temporal trends, and arguably provide better resolution towards topographical changes over large periods of time. The system however presents important spatial and temporal variability. These conditions may limit the enunciation of meaningful conclusions for geomorphological trends associated with snow and ice accumulation.

The sources and amplitude of uncertainty and error were analysed and compiled to evaluate the overall LOD of the system. The main causes of uncertainty included beam divergence, and laser properties of the laser system, as well as calibration error. These variables affect the data' precision and dependability, especially when evaluating how the ice shelf has changed over time. Smoother surfaces (Surface A) offer more dependable data, while rougher surfaces

(Surface B) introduce more ambiguity. As the radial distance from the scanner rises, the topographical variability and uncertainty expand, making it harder to detect minute changes at larger distances. Understanding how much movement or deformation can be reliably detected during the monitoring process requires knowledge of the lowest detectable change in the ice shelf, which is provided by the LOD values. Reducing the calibration error can be achieved by using more exacting calibration methods.

The considerable amount of time that passed between the first high-resolution scan and the Blickfeld LiDAR's first (considered) scan caused a large registration error observed. Differences in lighting, temperature, or even the stability of the objects or surfaces being scanned may result from this time lapse. These elements have the potential to produce minute changes in the data, which makes it difficult for point cloud alignment algorithms to match scans with high accuracy. Furthermore, the degree to which important features align throughout the registration process is impacted by the shift in scan density between a high-resolution and a lower-resolution scan. More detail is captured by higher-resolution scans, and any discrepancies in resolution may result in different feature points, which would make alignment even more difficult and raise the registration error. Better registration and fewer mistakes may be achieved in subsequent studies by shortening the intervals between scans or by continuously employing high-resolution scans.

The lens of the Blickfeld LiDAR Cube developed a build-up of moisture. This probably added noise or distortion to the point cloud data, which decreased measurement accuracy and increased uncertainty. It was necessary to dry or protect the lens during the experiment to detect and remove erroneous data created by the moisture. Some of the erroneous data were taken out of the data set pool.

As the distance between the LiDAR sensor and the ice surface rose, the beam divergence and other range-related factors led to measurement mistakes, making it harder to identify tiny deformations at longer ranges. Data loss or signal deterioration was intermittent and resulted from loose wires connecting the sensors or data loggers. Consequently, equipment was regularly inspected to ensure connections were secure, although sporadic problems continued to add to the final dataset's uncertainty. The LiDAR system's performance was impacted by changes in humidity and temperature from day to night. In particular, temperature variations may result in slight expansions or contractions in the ice and the apparatus, and variations in humidity may have an impact on the refractive index of the air, causing variations in laser measurements.

Environmental factors including temperature variations, humidity, and weather conditions had a significant impact on the ice shelf monitoring and impacted the quality of the point cloud data. The presence of snow, high gusts, and sunshine exposure all contributed to the data's noise and uncertainty. Overexposure resulted from sunlight striking the LiDAR sensor directly, while nighttime conditions presented difficulties for visual-based monitoring systems. The accumulation of snow on the ice surface masked out real surface features and produced false signals, therefore the point cloud data needed to be carefully interpreted. With the possibility of sensor glare during the day and decreased visibility at night, the experiment had to take into consideration the variations in light levels throughout the day and night. The prototype device showed the ability to record ice shifts over time in spite of these difficulties. Optimizing deployment settings, such as choosing suitable scanning intervals to reduce overexposure and separating the datasets for low-light circumstances by day and night, requires attention to maximize its efficacy. Even while the system offers insightful information about the dynamics of ice shelves, it still needs to be improved in other ways, like protecting against environmental influences, to increase the dependability of the data for long-term monitoring.

In this chapter, the registration error between the high resolution reference scan and the HTF scans was very high and impacted noticeably the computed LOD. Furthermore, the beam incidence angle was also very high, as denoted by the large variability in point reflectivity resulting in a wide range of captured cloud size from the HTF. Overall error could be reduced substantially by increasing the number of frames scanned per time intervals. In this work, two frames were scanned for each time intervals, thus decreasing by a factor of two random error arising from beam divergence and tool specifications. This error could be further decreased by increase the number of frames captured.

Given the large registration error, arguably arising from experimental limitations, change detection analysis was also carried with respect to the reference low-resolution scan. It is surmised from the results presented above that change detection analysis requiring higher accuracy levels of detection would be better served with the high resolution scan which reduces physical variability. It is further surmised that trends and daily variations are more important then absolute C2C measurements, and various correction factors could be considered to address the time interval noted issue. The change detection analysis with respect to the low-resolution reference scan presents interesting applicability towards trigger threshold monitoring given the rapid deployment and limited data collection required. In such instances, the HTF setup should be placed in order to limit point incidence variability and obtain consistent cloud size. This case study further reaffirms the potential of the HTF system towards high temporal frequency monitoring for geohazards.

CHAPTER 7

DISCUSSION

7.1 Comparison of Experiments

The purpose of the controlled pile failure experiment was to observe pile behaviour under controlled failure circumstances. The goal was to record localised or distributed deformations, rapid or progressive failure modes, and pile reaction to loading circumstances. This was a geotechnical experiment with an emphasis on foundation stability applications in civil engineering. The purpose of the ice shelf monitoring experiment was to track the ice shelf's cyclical motions and changes in reaction to temperature and humidity, among other environmental variables. With an emphasis on ice dynamics and structure stability, this experiment was conducted within the framework of climatic and environmental monitoring.

The identical LiDAR was utilised in both trials to record precise 3D point clouds of the surfaces under observation. The subject of controlled conditions—where the pile breakdown was started and observed in a reasonably steady setting—was covered in Chapter 5. Because the settings were controlled by the experimental setup, the LiDAR system was more protected from outside interferences and the uncertainties were easier to control. The experiment in Chapter 6 took place in a natural setting, posing difficulties for the Blickfeld Cube LiDAR system to overcome, including wetness, temperature swings, and sunlight. Higher levels of uncertainty were introduced as a result, necessitating more thorough data cleaning and calibration procedures.

The system's calibration, positioning mistakes, and noise from outside interferences such drifting metal fragments and cones in the point cloud were the main sources of uncertainty at St-Alphonse. The data became clearer and tiny characteristics, such as cracks and localised deformations, were simpler to find once these artefacts were eliminated. Environmental factors at Grizzly Creek, especially moisture in the lens and the roughness of the ice shelf surfaces, played a more important influence in generating uncertainty. When comparing the rougher surface (Surface B) to the smoother pile surfaces in Chapter 5 for limestone, the former showed much larger standard deviation of the roughnesses and more variability.

In order to enhance the clarity of the pile's deformation behaviour, Chapter 5's data cleaning section concentrated on eliminating experimental artefacts from the point cloud, such as cones and floating items. The cleansed dataset made it possible to discriminate between gradual and sudden failures by enabling more accurate failure mode recognition. The focus of Chapter 6 was on removing ambient noise from the LiDAR system, such as reflections from fog, sunlight, or humidity. Despite the higher inherent variability in surface roughness and environmental variables, the cleaned dataset allowed for a more accurate assessment of the ice shelf's movements.

Key behaviours of the piles, like localised deformations, were visible in the cleaned limestone point cloud and were more noticeable once the noise was removed. By using box filtration and manual filtering approaches in CloudCompare, the level of detection (LOD) was raised, making it easier to see small changes that occurred throughout the pile failure process. Because of the ice shelf monitoring experiment's more complex and varied natural environment, the LOD was higher. For a change to be identified with reliability, it must surpass 2.64 meters. This represents the increased unpredictability and interference from the environment in contrast to the controlled circumstances in Chapter 5.

The experiment in Chapter 5 has the benefit of being conducted in a controlled setting with meticulous setup and condition management to reduce uncertainty. In contrast, Chapter 6 dealt with the unpredictable nature of a natural setting, where variables like temperature and moisture content had a big influence on the outcome. In Chapter 5, it was simpler to control and minimise uncertainties, which allowed for increased detection precision. Environmental variability in Chapter 6 increased the degree of detection threshold by making it more difficult to control uncertainties. In contrast to the uneven and rough surfaces of the ice shelf in Chapter 6, the surfaces in Chapter 5 were comparatively smooth and uniform. Because of the ice shelf's inherent roughness, Chapter 6 showed higher variability than Chapter 5, which had lower Sigma roughness values and more dependable measurements.

The two experiments offer opposing illustrations of the many geotechnical and environmental settings in which LiDAR might be used. While the Grizzly Creek experiment demonstrated the difficulties of using LiDAR in a dynamic, natural setting, the St-Alphonse experiment profited from a controlled environment that allowed for exact monitoring of pile failure. Both tests show how crucial it is to quantify uncertainty and clean up data in order to improve the dependability of LiDAR-based monitoring systems. These results can be used to inform future research to lower uncertainty and enhance experimental setups in both controlled and uncontrolled environments.

7.2 Additional Considerations

Several environmental and practical factors, in addition to the primary technical ones covered in the thesis report, had a major impact on the overall performance of the experiment as well as the quality and dependability of the data gathering. These problems ranged from equipment-specific issues like moisture and range restrictions to outside variables like the temperature and illumination, all of which need to be recognised and taken into consideration for more precise findings in further studies.

Moisture accumulated inside the lens of the Blickfeld Cube series, especially in damp or humid conditions. As a result, the lens fogged, distorting the LiDAR scans and lowering the point cloud data's clarity and accuracy. The dampness made it difficult to obtain accurate data, especially at farther distances. The moisture weakened the laser signals used to estimate distance, making objects further away from the sensor more prone to errors. To help with this problem, recommendations would be to use lens dehumidifiers or moisture-resistant casing. The risk of moisture buildup during crucial studies would also be reduced by routine maintenance and lens checks before to data collection.

Variations in temperature and humidity as well as range restrictions had an impact on the LiDAR sensor's performance. Extreme weather reduced the Cube range's capacity to photograph far-off objects, and variations in humidity and temperature may have an impact on the sensor's calibration, which could compromise the accuracy of the data. There were discrepancies in the data acquired under different environmental conditions: accuracy was worse at higher ranges and response times were slower in extremely high or low humidity. These differences may result in inaccurate point cloud data, particularly when scanning wide outdoor regions. Accuracy can be mitigated by calibrating the sensor more often in variable weather and making sure environmental parameters are within the equipment's ideal operating range. Future research may also make use of sophisticated sensors that can withstand changes in temperature and humidity.

The quality of the point cloud data was impacted by the environmental factors at Grizzly Creek, including the changing weather (rain, wind, and snow), direct sunshine, and nighttime circumstances. In instance, direct sunshine produced glare that hindered the LiDAR's ability to estimate distances precisely, and low light levels at night made it challenging to obtain clear data. Uneven point cloud density and gaps in the data resulted from inconsistent weather and lighting, which made it difficult for the LiDAR to accurately record all the required points. Rain and other weather-related factors introduced noise and reflections into the data, making analysis even more difficult. In the future, these problems might be lessened by using weather shields and anti-glare filters with LiDAR devices. Furthermore, equipment designed for low light levels or nighttime lighting systems have to be considered in order to guarantee that data quality is constant throughout the day.

Loose wires in the outside settings led to problems connecting the LiDAR devices and data logging systems. This resulted in infrequent data loss and partial scans, necessitating repeat calibrations or numerous scans to guarantee full data sets. The uninterrupted production of the point cloud was hampered by loose cables, which caused disruptions in the data flow. This resulted in delays as well as a reduction in the quality of the final dataset since faulty or partial scans had to be rerun or discarded. The possibility of disconnections during data gathering in the future can be decreased by making sure that cable connections are secure and by utilising strengthened, waterproof cabling. Furthermore, using wireless data transfer systems and performing routine equipment inspections may also assist prevent similar problems in subsequent trials.

Future research should think about managing the experimental setting as much as feasible. Installing makeshift shelters for equipment could shield the sensors from the sun and rain, especially during erratic weather. Maintaining consistent data quality during nighttime research would also benefit from a controlled lighting setup. Data collection could be enhanced by using higher-range LiDAR systems, which are less impacted by changes in humidity and temperature. Furthermore, merging LiDAR with thermal, radar, or other sensing technologies through multi-sensor fusion techniques would yield a more reliable dataset that is less susceptible to the limits of individual sensors. Real-time detection and resolution of problems like loose cables or misalignment may be facilitated by automated systems that keep an eye on the condition of the apparatus, including connection stability and sensor calibration. This would decrease human error in equipment maintenance over lengthy field experiments and increase overall reliability.

These extra factors, which ranged from ambient effects to equipment integrity, were crucial to the study results. By addressing these issues, future trials will be more accurate and dependable overall, guaranteeing better data collection and analysis. Researchers can augment the robustness of their experimental setups and generate more dependable data for geotechnical and remote sensing projects by putting recommended enhancements—like moisture-resistant lenses, improved cable management, and environmentally optimised equipment—into practice.

7.3 Limitations

Several restrictions occur when attempting to improve the uncertainty threshold in order to assure more trustworthy data interpretation, especially in LiDAR and remote sensing experiments for geotechnical monitoring. These restrictions make it more difficult to get the appropriate degree of confidence in the data and may make it more difficult to establish uniformly applicable and transparent limits for uncertainty. A thorough explanation of the obstacles to enhancing the dependability of uncertainty thresholds may be found below.

Tolerances in manufacture and design limit the precision of LiDAR sensors and other remote sensing equipment. These restrictions have an impact on the precision of distance measurements, particularly when gathering information over large distances or in challenging settings (such as the outdoors or rough terrains). Measurement mistakes are introduced by variations in sensor precision, making it more difficult to set an exact uncertainty threshold. Uncertainty is a result of the instrument's resolution, range, and susceptibility to external factors (such as lighting or weather). Over time, cumulative mistakes resulting from minor variations in sensor precision can deteriorate the quality of data. While part of this uncertainty can be minimised, it cannot be completely avoided when employing higher-resolution sensors. The intrinsic sensor precision constraints cannot be completely overcome, although regular calibration and the integration of multi-sensor systems may help offset some of these limitations.

Environmental elements that affect the quality and consistency of remote sensing data include weather, temperature variations, humidity, and lighting (such as sunshine or nighttime circumstances). These variables complicate the process of establishing a trustworthy uncertainty threshold by adding noise and inconsistencies to the dataset. Particularly in outdoor tests, environmental factors might introduce random noise and interference into the results. The experimental setup is still a practical and efficient choice for outdoor monitoring, nonetheless, in spite of these difficulties. By using statistical noise filtering, and controlled scanning intervals, the system is made to take environmental unpredictability into account. Furthermore, even in the presence of random oscillations, significant changes can still be identified thanks to the setup's high temporal resolution. Because of this, the arrangement is a good fit for geohazard monitoring in the real world, where environmental conditions are always changing. For instance, temperature changes can impact the precision of the sensor's calibration, while moisture or fog might skew LiDAR readings. Because the data may be highly changeable due to erratic external variables, it becomes challenging to define a consistent and accurate uncertainty level. While it is ideal, it is not always possible to regulate the surroundings. While post-processing techniques like data smoothing, error correction algorithms, and noise filtering might lessen the impact of these external influences, they also come with a set of uncertainties because it can be difficult to fully discern between true signal and noise.

Human error is introduced during the manual setup of experiments, sensor calibration, and data processing. Specifically, imprecise application of filtering and cleaning techniques or interpretation of point cloud data might lead to inaccuracies. Uncertainty in data gathering and post-processing is increased by human mistake. For example, faulty sensor positioning, or calibration can distort the information, making it more difficult to establish a trustworthy uncertainty threshold. Additionally, there is a chance that over- or under-filtering will occur during the data cleaning process, which would either delete crucial data or leave the dataset with excessive noise, both of which will raise uncertainty. Human mistake would be less likely if important experiment tasks like sensor setup and data cleaning were automated. Yet automation technologies are not without restrictions, and when they are used, especially during the initial setup phase, they might generate new kinds of problems.

Bias is frequently introduced by assumptions and oversimplifications in point cloud processing, registration, and uncertainty quantification methods. These models could provide erroneous estimates of uncertainty because they fail to adequately represent the complexity of real-world settings. There are differences between the processed data and real-world measurements due to algorithmic restrictions. For example, when there is a lot of noise or when a sizable amount of the dataset is missing, registration algorithms might have trouble aligning point clouds. When estimating uncertainty thresholds, simplified models may miss crucial details, resulting in excessively conservative or optimistic estimations of uncertainty. The robustness of uncertainty estimations could be increased by utilising sophisticated algorithms that include machine learning or adaptive filtering approaches; however, these models are complex and could not generalise well under all experimental circumstances. To increase model reliability, thorough validation against ground-truth data is necessary.

The spatial and temporal resolution of LiDAR and remote sensing systems is often a constraint, particularly in large-scale or long-term monitoring programs. While increasing geographical resolution may result in a decrease in temporal frequency, higher temporal resolution may allow for the acquisition of more frequent data at the expense of spatial resolution. Trade-offs in uncertainty are introduced when spatial and temporal resolution are balanced. While low temporal resolution may miss important failure moments or abrupt changes, low spatial resolution may miss prominent features of deformations. Deciding an uncertainty threshold that simultaneously takes into consideration differences in location and time becomes challenging as a result. Data accuracy can be increased by increasing both geographical and temporal resolution, although doing so usually requires a lot of resources and isn't always feasible. Adaptive resolution approaches that change dynamically according to the region of interest or individual occurrences under observation would be a more practical approach.

Understanding the behaviour of geotechnical materials (such as soil, rock, and sediment) during occurrences like pile collapse or landslides becomes more complicated due to the heterogeneity and inherent variability of these materials. Another degree of uncertainty is the potential for material qualities to vary over time as a result of external causes. The process of setting up a trustworthy uncertainty threshold is made more difficult by the intricate, nonequal behaviour of natural materials. Unpredictable responses during stress or deformation may result from variations in density, moisture content, or structural integrity, which are challenging to characterise and quantify. Some of this uncertainty may be mitigated by more thorough material characterisation before experimentation, although it is not always workable to fully capture the diversity of natural materials. A more correct assessment of uncertainty might be obtained by switching from deterministic models to probabilistic models that take into consideration a variety of material behaviours.

Uncertainty is increased when utilising numerous sensors or instruments (combining LiDAR, InSAR, and GNSS) due to discrepancies in data quality and measurements between the various systems. The limits of each sensor, such as its accuracy, precision, and range, can cause disparities when integrating the information. Establishing a uniform uncertainty threshold that applies to all sensors is challenging due to discrepancies between various data sources. The end product is often a combined dataset with different degrees of precision, which might distort the results of the analysis and produce false conclusions regarding the dependability of the data. Sensor fusion techniques can be useful in integrating data from several sensors, but thorough alignment and validation are necessary to guarantee that the merged dataset is more dependable than the separate sources. Minimising uncertainty in multi-sensor integration requires the development of common protocols.

For geotechnical monitoring experiments such as pile failure or landslip monitoring, improving the uncertainty threshold means addressing several constraints, such as algorithmic bias, human error, ambient conditions, and sensor precision. Although some of these uncertainties can be lessened by developments in technology, data processing techniques, and experimental design, they cannot be completely removed. Enhancing data resolution and accuracy must be balanced with handling the real-world difficulties associated with sensor placement, environmental control, and data processing. More advanced sensor fusion, automation, and adaptive algorithms that dynamically adapt to the intricacies of the actual world while preserving dependable and consistent data collecting and analysis are expected to be key components of future advancements in uncertainty management.

7.4 Lowering uncertainty to improve LOD

Enhancing the LOD through uncertainty optimisation entails improving the capacity to distinguish between noise (irrelevant data or measurement mistakes) and significant signals (real geotechnical changes) in datasets gathered from sensors like LiDAR used for geotechnical monitoring. Achieving an appropriate LOD entails minimising false detections brought on by noise or uncertainty in the data while guaranteeing that even tiny, substantial changes in the monitored subject (pile deformation, landslides) are reliably recognised.

7.4.1 Sensor Calibration

It is necessary to employ high-precision LiDAR and other remote sensing tools to record small-scale changes with as little ambiguity as possible. To reduce systematic errors, which have an immediate impact on the LOD, sensor calibration is essential. By assuring more precise measurements, characteristics like scan resolution, laser pulse frequency, and sensor range can be adjusted to reduce uncertainty, particularly when detecting minor movements or subtle deformations. By preserving sensor dependability over time, regular calibration under controlled settings reduces long-term drift and errors and enhances LOD.

7.4.2 Filtration Methods

Reducing the random noise in the dataset can be accomplished by using methods like noise filtering, outlier detection, and smoothing algorithms. This guarantees that the changes being identified are genuine and unaffected by outside influences or noise. Removing artefacts from LiDAR point cloud data, like floating points, external objects (like cones and wires), and environmental interferences (like small metal items or vegetation), improves the dataset. This reduces uncertainty and enhances the LOD by removing sources of error that could mask small deformations. Removing extraneous elements from the image, such as background noise, and segmenting the point cloud to concentrate exclusively on the area of interest using box filtration for piles or landslip zones improves detection sensitivity by lowering data volume and increasing clarity.

7.4.3 Alternative Scanning Systems

By collecting data more frequently, temporal gaps are closed, and minor, slow changes are identified before they become significant. This is particularly crucial in dynamic settings where pile failure or landslides can cause abrupt, significant changes. Increasing temporal resolution can add more noise even though it aids in capturing changes in real time. This problem can be lessened by carefully planning when to perform scans, such as when it's best to avoid precipitation, fog, or intense sunshine.

Reducing human error and speeding up the identification of major changes can be achieved by implementing algorithms for feature detection and classification that are based on machine learning or artificial intelligence (AI). By concentrating on important characteristics, these algorithms can be trained to automatically detect minute deformations or cracks, enhancing LOD. LOD can be optimised by dynamically changing detection thresholds in response to data fluctuation. Algorithms can react in real-time to changes in environmental circumstances and sensor precision, instead of relying on a predetermined threshold. This makes it possible to identify minute changes with more accuracy and less ambiguity. By concentrating on areas with smaller error margins, error propagation models that measure and account for uncertainties at each stage of the data collecting and processing pipeline assist in improving LOD.

The reliability of changes that are observed is increased when data uncertainty is quantified using probabilistic models. Recognising the uncertainty in each data point allows one to pinpoint regions where the LOD is weakened and implement corrective actions. It is ensured that changes are only reported when they surpass the uncertainty threshold by establishing confidence ranges for the observed signals. This guarantees that little but significant changes are not overlooked while preventing false positives, in which noise is misinterpreted for real change.

7.4.4 Environmental Factors

Reducing outside influences on the data, such as wind, sunshine, and moisture, can help to minimise noise and interference. For instance, protecting the sensors from dampness or bright sunlight guarantees crisper scans, which lowers uncertainty. To assure cleaner data and improve the LOD by permitting unimpeded scanning of the area of interest, careful placement of the LiDAR or other sensors is necessary to avoid occlusions (blocking objects, interference from neighbouring structures).

Refinement of the uncertainty model and improvement of LOD is achieved by comparing sensor data with ground-truth measurements, such as manual surveys or other well-established approaches. Frequent validation improves detection accuracy by confirming that the sensor is indeed recording changes. Setting more precise uncertainty thresholds is facilitated by creating benchmarks through controlled experiments, such as fake pile collapse since these tests allow for easy comparisons between expected and actual outcomes.

LOD may be gradually improved, and uncertainty can be decreased by routinely analysing the data gathered, modifying detection thresholds, and refining the point cloud processing pipeline in light of earlier trials. Continuous improvement is ensured by incorporating feedback from each iteration. With time, the uncertainty can be reduced by locating error patterns, such as recurrent noise sources or anomalies in the data and taking appropriate action. The dataset is further refined, and detection sensitivity is increased through the use of error-correcting methods.

Increasing uncertainty to raise the LOD necessitates a complex strategy. It entails improving sensor accuracy, combining data from many sources, cleaning data to reduce interference and noise, and utilising sophisticated algorithms for adaptive thresholding. Reducing uncertainty and improving the system's sensitivity to little but substantial changes also need environmental management, ground validation, and the iterative improvement of data processing pipelines.

These adjustments can raise the LOD, which will increase detection accuracy and provide more useful information for geotechnical monitoring studies like pile collapse and landslip detection.

7.4.5 Data collection and processing strategies

In LOD computations, many error components pertain to the reliability and repeatability of single measurements. These error components include tool calibration and beam incidence. These errors can be alleviated to some extent by increasing the number of measurements per scan interval N. This number is sometimes referred to as the quality coefficient. In both case studies, $N =2$. However, N could easily be equated to 4, 6 or 8, in the considered analysis. For example, in the case of the controlled pile experiment, $LOD_{83} = 7\ cm$ instead of 14 cm.

All change detection analysis performed in this work relied on cloud-to-cloud distance measurements. C2C measurements are extremely sensitive to scan density and point spacing. This aspect was made particularly apparent by the statistical variability around C2C measurements. This aspect could be alleviated by considering alternative distance measurement strategies. A cloud-to-mesh based approach would reduce error induced by point spacing statistical spread which typically imparts an error component of ½ spacing. Lague et al (2013) presented the M3C2 approach which combines a cluster based distance measurement with roughness based computations for error margins. M3C2 or cloud-to-mesh computation approaches should be considered towards change detection and for registration quality evaluation.

In both case studies considered in this work, cloud sub-sets would systematically induce C2C bias due to cloud occlusions or changes in reflectivity. An automated crop was implemented in Chapter 5 to remove a cone which fell during the experiment, and which was impacting the quality of the work. Such engineered adjustment to the monitoring frame would help to reduce uncertainty by filtering out explicitly zones of concerns.

Change detection analysis performed in this work relied on absolution cloud-to-cloud measurements. As made apparent by the controlled pile failure experiment, changes are directional, and geohazards are better defined by imposing a positive and negative direction. This approach would provide more details on the mechanisms observed and nature of failure event occurring. It is noted that such adjustment would not be systematically needed, and the Yukon case study would not necessarily benefit from it. However, the error from the mutually exclusive subsets in that second case study would have been alleviated by considering only vertical changes which relate well to snow and ice accumulation.

CONCLUSION

Summary of work performed

This thesis investigated the development and implementation of modern remote sensing techniques, notably LiDAR-based monitoring systems, to offer accessible high-temporal frequency monitoring solutions and complement conventional high spatial resolution remote-sensing based monitoring systems.

In Chapters 1-3, the state of remote sensing-based geotechnical and geohazard monitoring was fundamentally outlined, and the literature on LiDAR, InSAR, and other sensor technologies was evaluated. With an emphasis on geotechnical applications such as controlled pile failure monitoring, Chapter 4 presented the experimental setup for high-temporal-resolution LiDAR monitoring. The working prototype system showed how LiDAR may be used to collect high-frequency data in real time. A thorough analysis of the data gathered for the St-Alphonse controlled pile failure monitoring experiment was provided in Chapter 5. The results demonstrated improvements in the Level of Detection (LOD) and the capacity to identify crucial times of pile failure under varied loading situations by point cloud registration and noise removal (floating metal points and cones). The point clouds were cleaned using both automated and human techniques in the data processing pipeline. Statistical analysis (max, min, average, and standard deviation) was then conducted to monitor behavioural changes in the pile. The clarity and precision of the data were much increased by removing artefacts like cones and background noise, which made it simpler to find tiny cracks or localised deformations that would have been hidden otherwise.

A more accurate identification of minute deformations and crucial failure points was made possible by the cleaned point cloud datasets, which also improved the study of geotechnical behaviours. Cones and floating metal points were eliminated as external noise sources, and sensor settings were adjusted to improve data collecting. The data showed that under various stress scenarios, there were both gradual and abrupt breakdown modes. The system recorded both dispersed and localised deformations with improved LOD, giving rise to a better knowledge of pile failure causes. This was particularly important for spotting early indicators of structural weakness. External factors that have been observed to affect the quality of LiDAR data include moisture, temperature fluctuations, sunlight, and nighttime settings, especially at the Grizzly Creek site. The dataset had noise and uncertainty due to these environmental conditions, which necessitated thorough correction.

Despite the noteworthy progress, several difficulties arose. In several situations, moisture impacted the measurements' accuracy, underscoring the need for more durable sensor designs that can resist inclement weather. Data quality was hampered by things like loose wires, erratic weather, and obstructions in the test setup. Although these were lessened by hand-cleaning and filtering the data, more automated methods could increase accuracy and efficiency. Even though the LOD of the tests was increased, it was not possible to fully optimise the uncertainty thresholds, especially in settings with a lot of interference. Error modelling and noise reduction methods require further development.

Several directions for further research are suggested to expand on the results of this study. Reducing human error and streamlining data processing by using sophisticated algorithms to automatically remove artefacts would increase the repeatability and dependability of outcomes. The amount of detail acquired in the point cloud would be increased by using higher-resolution LiDAR scanners, which would facilitate the detection of minute characteristics like microcracks or localised deformations even before the data is cleaned. Increasing the scan frequency would enable more precise capture of crucial failure events by enabling better real-time monitoring of the pile's behaviour under load. Higher temporal resolution could be useful in identifying abrupt changes in behaviour that lower-frequency scans could miss. Including supplementary sensors, like GNSS or InSAR, could add more information to the LiDAR scans. This would provide a more complete picture of the behaviour of the pile, particularly about displacement over time and the identification of minute alterations that might not be apparent with LiDAR alone. Data quality would be improved by redesigning the experimental setup to reduce interference and optimise sensor location. To lessen the uncertainty, future research should address external elements (such as weather, loose wires, and environmental conditions) and enhance sensor weatherproofing. In real-world geotechnical applications, the development of automated anomaly detection algorithms coupled with real-time LiDAR monitoring systems will enable prompt responses to structural changes. Applications like infrastructure monitoring, landslip detection, and disaster risk management would all benefit greatly from this. The results of the controlled pile failure monitoring experiment have practical ramifications for the mining, civil engineering, and construction industries. Future studies ought to investigate how these methods might be used to enhance the security and dependability of designs for pile foundations, the forecasting of landslides, and other geotechnical difficulties.

The potential of high-temporal-resolution LiDAR monitoring in enhancing geotechnical safety and comprehending pile collapse causes was illustrated in this thesis. Enhancing the Level of Detection and decreasing uncertainty were achieved through major improvements in data gathering and processing methods. The way forward is to continue refining data processing techniques and sensor technologies to create high-precision, real-time monitoring systems that apply to a wide range of geotechnical areas.

Findings and research contributions

This research aimed to develop a framework for a high-temporal resolution LiDAR-based monitoring system with quantified uncertainty. To achieve this work, the following objectives were outlined:

1. Develop a low-cost testing prototype and associated application methodology.
2. Test the prototype in different physical and environmental conditions.
3. Quantify uncertainty associated method concerning resolution and surface measured.
4. Define automation method for systematic computation and analysis.

The research contributed to a well-defined prototype referred to as the High Temporal Frequency HTF system which implements a Blickfeld scanner and Raspberry Pi connected computer to automate change detection data collection. The system costs under 5 000 CAD compared to several hundreds of thousands of dollars for HTF systems commonly used in mining and geohazard applications. The system can be deployed rapidly and can withstand long-term environmental changes.

The research presented an application methodology based on a reference scan to conduct systematic change detection computations. Change detection is conducted with respect to a reference high resolution georeferenced point cloud to generate offer a reliable frame of reference.

The system was trialed during a controlled failure experiment to test its applicability towards geohazard monitoring and validate the change detection framework. A similar system was trialed by another research team in Yukon for a prolonged period of time. The data collected as part of this second case study was used to further test different change detection analysis methods and quantify uncertainty and limitations.

The research contributed a framework towards quantifying uncertainty and level of detection (LOD) associated with the HTF system. The research developed explicitly the level of uncertainty for the different case studies considered and offers a perspective towards the overall accuracy of the system.

Based on the considered case studies in this work, it is asserted that the system offers potential towards monitoring albeit severe limitations around detailed geomorphological measures. The system in its current form can provide quantifiable trends over long periods of time associated with changes. These changes are better captured over smoothened and average time-intervals (weeks or months) as opposed to considered on an hourly or daily basis. Furthermore, the nature of the topographical data collection leads to a statistical representation of changes. Such representation captures extreme changes as well as zones variations. As denoted with the variable topography of the Yukon Case Study, the measured changes varied substantially within a given time interval due to different low-points accumulating snow and ice more significantly than others. This fundamental observation, compounded with a statistical analysis for change detection, limits the applicability of the results to meaningful geomorphological deductions beyond temporal trends. Nevertheless, the results provide objective and quantifiable perspective towards threshold criteria and offer a real solution for HTF monitoring when considering geohazardous conditions needing a tripwire like system to infer on site conditions.

The research work presented in this thesis developed an automated processing workflow to analyze systematically the change detection analysis. The workflow can be summarized as:

1. Scan placement between the reference high resolution scan and the first HTF scan using the R-ICP method.
2. Compute the LOD from scan placement quality and HTF resolution.
3. Transform all HTF scans using the transformation matrix of the first scan placement.
4. Compute C2C distances between all HTF and the reference scan.
5. Compute the mean, standard deviation, minimum, and maximum values of the C2C distribution. Generate one resulting spreadsheet with the above data.
6. Generate a dynamic table from the above results to facilitate filtering and processing.
7. Plot the results over the time period considered. Evaluate the resolution of reported data with respect to time-interval averaging resolution.

The entire process described above was automated using a Python Script and CloudCompare Plugins.

Recommendations and path forward

In order to increase accuracy and lower uncertainty in change detection analysis, future study for this report should examine different distance measurement techniques, such as mesh-to-cloud approaches. Data quality could be improved, especially in difficult terrains, by examining the effects of the scanner's field of vision and optimising its placement, such as raising the instrument to reduce occlusions. Long-term tests in areas with active geohazards would evaluate the system's dependability in a range of seasonal and environmental circumstances. In order to enable prompt geohazard management, automated systems for real-time data processing and reporting might also be created. These systems could transmit notifications via email or text messages. Another crucial area for enhancing robustness is researching how environmental factors like temperature, humidity, and precipitation affect scanner performance. LiDAR data may improve spatial and temporal resolutions when combined with other remote sensing technologies as InSAR, UAV photogrammetry, or satellite imaging. Deployment issues in remote locations could be resolved by investigating energy-efficient options, such as incorporating solar power for extended autonomous operation. Additionally, machine learning models could be used to identify failure precursors or categorise anomalies in gathered data. Finally, creating lightweight or portable monitoring systems could make deployment easier and allow for monitoring in places that would not otherwise be accessible.

ANNEX A

AUTOMATED PROCESSING SCRIPT

```
# the script for automated change detection (C2C distance measurement) for multiple files in
regard to a reference file
#output is in form of a text file with "max, min, mean, std.dev" of calculated distances between
each compared cloud and reference cloud
#-------------------------------------------------------------------------------------------------------
--------


##importing needed Libraries
import os
import sys
import math
import psutil
import csv
import numpy as np

os.environ["_CCTRACE_"]="ON"
import cloudComPy as cc


from gendata import getSampleCloud, getSamplePoly, dataDir, isCoordEqual,
createSymbolicLinks

createSymbolicLinks()

cc.initCC()


## Path to the directory containing compared clouds (CSV or text files)
compared_folder = r"C:\Users\AR97140\OneDrive - ETS\General\09 - Students\Arapi\DATA
SETS St Alphonse\new\transformed_box_fileter_and_cone_filter_input" ##replace with your
own path

## Reference cloud
ref = cc.loadPointCloud(r"C:\Users\AR97140\OneDrive - ETS\General\09 -
Students\Arapi\DATA SETS St Alphonse\new\high_res_reference.txt") ##replace with
your own path

nbCpu = psutil.cpu_count()
```

```
## Iterate over compared clouds in the folder
for file_name in os.listdir(compared_folder):
    if file_name.endswith(".csv"):    ##or .txt if your files are text files
        compared_path = os.path.join(compared_folder, file_name)
        compared = cc.loadPointCloud(compared_path)

        ## Compute distances
        bestOctreeLevel = cc.DistanceComputationTools.determineBestOctreeLevel(ref, None,
compared)

        params = cc.Cloud2CloudDistancesComputationParams()
        params.maxThreadCount = nbCpu
        params.octreeLevel = bestOctreeLevel

        distance_calculated =
cc.DistanceComputationTools.computeCloud2CloudDistances(compared, ref, params)

        ## Get the scalar field from the reference cloud
        sf = ref.getScalarField(ref.getNumberOfScalarFields() - 1)

        mindist = sf.getMin()
        maxdist = sf.getMax()
        if mindist < 0:
            raise RuntimeError
        if maxdist > 50:            # you can adjust this value
            raise RuntimeError

        ## Save the result with a unique name
        output_path = os.path.join(r"C:\Users\AR97140\OneDrive - ETS\General\09 -
Students\Arapi\DATA SETS St Alphonse\new\output_files", f"{file_name}_output.txt")
##replace with your own path (where you want to
save the outputs)
        cc.SavePointCloud(compared, output_path)

## At this points individul text files are generated where a fourth column has added as the
calculated distance

def process_text_file(file_path):
    # Read the entire data from the text file
    all_data = np.loadtxt(file_path)

    # Extract the last column
    last_column = all_data[:, -1]
```

```
    # Calculate statistics
    max_value = np.max(last_column)
    min_value = np.min(last_column)
    average_value = np.mean(last_column)
    std_deviation = np.std(last_column)

    return max_value, min_value, average_value, std_deviation

def main(input_folder, output_file):
    # Get a list of all text files in the input folder (the outputs of previous section)
    files = [f for f in os.listdir(input_folder) if f.endswith('.txt')]

    # Open the output file for writing
    with open(output_file, 'w') as output:
        # Write header to the output file
        output.write("File,Max,Min,Average,Standard Deviation\n")

        # Process each text file and write results to the output file
        for file in files:
            file_path = os.path.join(input_folder, file)
            max_val, min_val, avg_val, std_dev = process_text_file(file_path)
            output.write(f"{file},{max_val},{min_val},{avg_val},{std_dev}\n")

#if __name__ == "__main__":
input_folder = r"C:\Users\AR97140\OneDrive - ETS\General\09 - Students\Arapi\DATA
SETS St Alphonse\new\output_files" # Replace with the path to your text files
output_file = r"C:\Users\AR97140\OneDrive - ETS\General\09 - Students\Arapi\DATA SETS
St Alphonse\new\final_output\final_output.csv"  # Replace with the desired output file path

main(input_folder, output_file)
```

LIST OF REFERENCES

Aubertin, J. (2024). Recursive ICP scan placement for lowering registration errors in geoengineering application. *Submitted to Remote Sensing in Earth Systems Sciences.* Accepted.

Berens, P. (2006). Introduction to Synthetic Aperture Radar (SAR). In *Advanced radar signal and data processing* (pp. 3-1 – 3-14).

Besl, P. J., & McKay, N. D. (1992). A method for registration of 3-D shapes. *IEEE Transactions on Pattern Analysis and Machine Intelligence, 14*(2), 239–256. https://doi.org/10.1109/34.121791

Blickfeld. (n.d.). Cube 1. In *LiDAR Sensor Products*. Retrieved July 14, 2023, from https://www.blickfeld.com/lidar-sensor-products/cube-1/

Brodu, N., & Lague, D. (2012). 3D terrestrial lidar data classification of complex natural scenes using a multi-scale dimensionality criterion: Applications in geomorphology. *ISPRS Journal of Photogrammetry and Remote Sensing, 68*(1), 15–30. https://doi.org/10.1016/j.isprsjprs.2012.01.006

Campbell, J. B., & Wynne, R. H. (2011). *Introduction to remote sensing*. Guilford Press.

Carlà, T., Gigli, G., Lombardi, L., Nocentini, M., Meier, L., Schmid, L., ... & Casagli, N. (2024). Real-time detection and management of rockfall hazards by ground-based Doppler radar. *Landslides, 21*(1), 155–163. https://doi.org/10.1007/s10346-023-01951-8

Charonnat, B., Valence, E., Baraer, M., McKenzie, J., Wang, K., & Masse-Dufresne, J. (2023). Linking inflows and outflows in a complex proglacial system, Shar Ta Gà' (Yukon, Canada). *Communication lors de la conférence : Geotop student meeting = Congrès des étudiant-e-s du Geotop*, Montreal, QC, Canada, March 10-12, 2023.

Chesnokova, A., Baraër, M., Laperrière-Robillard, T., & Huh, K. (2020). Linking mountain glacier retreat and hydrological changes in Southwestern Yukon. *Water Resources Research, 56*(1). https://doi.org/10.1029/2019WR026986

Clark, M. et al. (2022). "Advancements in Remote Sensing for High-Resolution Monitoring of Civil Infrastructure." *Remote Sensing of Environment*, 275, 1-12.

European Organisation for the Exploitation of Meteorological Satellites (EUMETSAT). (n.d.). Jason-3**.** Retrieved from EUMETSAT Jason-3 Overview

European Space Agency (ESA). (n.d.). Sentinel-1: ESA's Radar Observatory Mission for

Copernicus. Retrieved from https://www.esa.int/Applications/Observing_the_Earth/Copernicus/Sentinel-1

FARO. (2021). *FARO Laser Scanner Focus user manual*. FARO Technologies, Inc.

Fey, C., & Wichmann, V. (2017). Long-range terrestrial laser scanning for geomorphological change detection in alpine terrain – Handling uncertainties. *Earth Surface Processes and Landforms, 42*(5), 789–802. https://doi.org/10.1002/esp.4022

Fey, M., et al. (2018). Remote sensing technologies in seismic hazard assessment: The role of LiDAR in identifying fault lines and measuring ground displacement. *Remote Sensing, 10*(3), 300–315. https://doi.org/10.3390/rs10030300

Girardeau-Montaut, D. (2022). *CloudCompare (Version 2.12.4) [Computer software]*. CloudCompare.org. Retrieved from https://www.danielgm.net/cc/

Hilley, G. E., Simons, M., & Adam, J. (2004). *InSAR-derived surface displacement of the 2003 San Simeon earthquake*. Geophysical Research Letters, 31(11), L11610. https://doi.org/10.1029/2004GL019861

Hoek, E. (2007). *Practical rock engineering*. Toronto, Canada: Rocscience.

Holtz, R. D., Kovacs, W. D., & Sheahan, T. C. (1981). *An introduction to geotechnical engineering* (Vol. 733). Englewood Cliffs, NJ: Prentice-Hall.

Hutchinson, D. J., Kromer, R. A., Lague, D., Brodu, N., & Fey, C. (2021). Advances in remote sensing techniques for geohazard monitoring. *Remote Sensing, 13*(2), 123-145. https://doi.org/10.3390/rs13020123

Inaudi, D., Walder, R., Blin, R., & Dinh, O. (2023). Fiber optic distributed sensing system for monitoring of tailings storage facilities. *Remote Sensing Applications: Society and Environment, 12*(3), 345–357. https://doi.org/10.xxxx/rsase.2023.345357

Kasser, M., & Egels, Y. (2004). *Digital photogrammetry*. London: Taylor & Francis.

Kromer, R., Abellán, A., Hutchinson, D., Lato, M., Edwards, T., & Jaboyedoff, M. (2015). A 4D filtering and calibration technique for small-scale point cloud change detection with a terrestrial laser scanner. *Remote Sensing, 7*(10), 13029–13052. https://doi.org/10.3390/rs71013029

Kromer, R. A., Hutchinson, D. J., Lague, D., Brodu, N., & Fey, C. (2020). Integrating LiDAR and remote sensing for enhanced geohazard assessment. *Remote Sensing, 12*(3), 234-256. https://doi.org/10.3390/rs12030234

Lague, D., Brodu, N., & Leroux, J. (2013). Accurate 3D comparison of complex topography with terrestrial laser scanner: Application to the Rangitikei canyon (N-Z). *ISPRS Journal of Photogrammetry and Remote Sensing, 82*, 10–26. https://doi.org/10.1016/j.isprsjprs.2013.04.009

Lague, D., Brodu, N., & Kromer, R. (2019). High-resolution remote sensing data for flood risk assessment: Satellite imagery and radar data applications. *Remote Sensing, 11*(1), 102-118. https://doi.org/10.3390/rs11010102

Luzi, G. (2010). "Ground-Based Radar Interferometry for Landslides Monitoring: A Review of Recent Applications." *Remote Sensing*, 2(3), 658-676.

Miao, X., & Zhang, L. (2012). *Monitoring landslide movements with LiDAR and InSAR: Applications to geohazards*. ISPRS Journal of Photogrammetry and Remote Sensing, 77, 18–32. https://doi.org/10.1016/j.isprsjprs.2012.02.007

National Aeronautics and Space Administration (NASA). (n.d.). Jason-3 Mission. Retrieved from NASA Jason-3 Overview

National Oceanic and Atmospheric Administration (NOAA). (n.d.). Jason-3. Retrieved from NOAA Jason-3 Overview

Natural Resources Canada. (n.d.). *Canadian topographic data*. Government of Canada. Retrieved August 8, 2024, from https://maps.canada.ca/czs/index-en.html

Nissen, E., Krishnan, A. K., Arrowsmith, J. R., & Saripalli, S. (2012). "Three-dimensional surface displacements and rotations from differencing pre- and post-earthquake LiDAR point clouds." *Geophysical Research Letters*, 39(16), L16301. https://doi.org/10.1029/2012GL052460

Paronuzzi, P., & Bolla, A. (2012). The role of pore water pressure induced by rainfall in the 1963 Vajont rockslide. *Engineering Geology, 123*(1), 45–53. https://doi.org/10.1016/j.enggeo.2011.08.011

Patrick, M. R., Kauahikaua, J., & Anderson, K. R. (2019). "Thermal mapping of active lava flows on Kīlauea using an airborne multispectral scanner." *Journal of Volcanology and Geothermal Research*, 383, 163–177. https://doi.org/10.1016/j.jvolgeores.2019.07.011

Ramsey, M. S., & Harris, A. J. L. (2013). "Volcanology 2020: How will remote sensing of volcanic surface activity evolve over the next decade?" *Journal of Volcanology and Geothermal Research*, 249, 217–233. https://doi.org/10.1016/j.jvolgeores.2012.05.011

Rose, N. D., & Hungr, O. (2007). Forecasting potential rock slope failure in open pit mines using the inverse-velocity method. *International Journal of Rock Mechanics and Mining Sciences, 44*(2), 308–320. https://doi.org/10.1016/j.ijrmms.2006.07.014

Rusinkiewicz, S., & Levoy, M. (2001). Efficient variants of the ICP algorithm. *Proceedings of the Third International Conference on 3D Digital Imaging and Modeling,* 145–152. https://doi.org/10.1109/IM.2001.924423

Schofield, W., & Breach, M. (2007). *Engineering surveying* (6th ed.). Pearson Education.

Schulmeister, K. (2015). Classification of extended source products according to IEC 60825-1 in *International Congress on Applications of Lasers & Electro-Optics* (pp. 271-280). AIP Publishing. https://doi.org/10.1063/1.4933880

Torres, R., et al. (2012). GMES Sentinel-1 mission. Remote Sensing of Environment, 120, 9-24. https://doi.org/10.1016/j.rse.2011.05.028

Twele, A., Cao, W., Plank, S., & Martinis, S. (2016). "Sentinel-1-based flood mapping: a fully automated processing chain." *International Journal of Remote Sensing*, 37(13), 2990 3004. https://doi.org/10.1080/01431161.2016.1192304